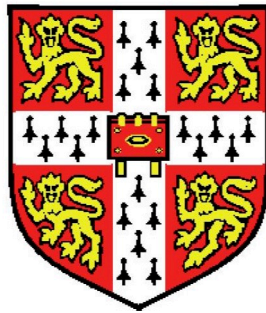


Towards Colloidal Self-Assembly for Functional Materials



University of Cambridge  
Department of Physics, Cavendish Lab  
Darwin College

Zachary M. Ruff

A thesis submitted on 29<sup>th</sup> of September 2017 for  
the Degree of Doctor of Philosophy



## **Abstract**

Nanostructuring has led to materials with novel and improved materials properties driving innovation across fields as varied as transportation, computing, energy and biotechnology. However, the benefits of nanostructured material have not widely been extended into large-scale, three-dimensional applications as deterministic pattern techniques have proven too expensive for devices outside of high value products. This thesis explores how colloidal self-assembly can be used to form macroscopic functional materials with short-range order for electronic, photonic and electrochemical applications at scale.

DNA-functionalized nanoparticles are versatile models for exploring colloidal self-assembly due to the highly specific, tunable and thermally reversible binding between DNA strands. Gold nanoparticles coated with DNA were used to investigate the temperature-dependent interaction potentials and the gel formation in DNA-colloidal systems. The electronic conductivity and the plasmonic response of the DNA-gold gels were studied to explore their applicability as porous electrodes and SERS substrates, respectively. Subsequently, silica nanoparticles were assembled into nanostructures that preferentially scatter blue light using both DNA and polymer-colloid interactions. Finally, rod-sphere structures made from DNA-coated gold nanoparticles and viruses were explored, demonstrating how high-aspect ratio building blocks can create composite structures with increased porosity. The gold-virus gel structures inspired the design and assembly of a silicon-carbon nanotube composite material using covalent bonds that shows promise for high energy density anodes.

## Preface

### Author Contributions:

Section 2.2.: Yang Lang helped prepare Figure 13.

Section 3.4: The *in-situ* SEM was performed with the help of Richard Langford.

Section 5.1: The gold-virus study was performed in conjunction with Simon Nathan and Robert Unwin. Simon prepared the microscopy samples from the functionalized colloids and performed the fluorescent microscopy. Simon performed the structure factor analysis and Rob Unwin performed the chord analysis on the micrographs. Rob produced the virus stocks and the viruses were functionalized together with Rob.

Section 5.2: The silicon-carbon nanotube composite study was performed in conjunction with Rajesh Jethwa as his part III project in the chemistry department. I supervised and designed the project with Prof. Clare Grey and Prof. Dom Wright. Rajesh functionalized and performed the characterization measurements on the silicon nanoparticles, the carbon nanotubes and the composite material. The TEM images were taken with the help of Jonathon Rickard.

### Related Publications:

Journal articles published during thesis:

- Z. Ruff, C. P. Grey, and E. Eiser. Thermally reversible nanoparticle gels with tuneable porosity showing structural colour. *Physical Chemistry Chemical Physics*. 2018
- M. Zupkauskas, Y. Lan, D. Joshi, Z. Ruff, E. Eiser, Optically Transparent Dense Colloidal Gels. *Chemical Science* 2017.
- Z. Ruff, S. H. Nathan; R. R. Unwin, M. Zupkauskas, D. Joshi, G. P. C. Salmond, C. P. Grey, E. Eiser, Designing disordered materials using DNA-coated colloids of bacteriophage fd and gold. *Faraday Discussions* 2015.
- L. Di Michele, B. M. Mognetti, T. Yanagishima, P. Varilly, Z. Ruff, D. Frenkel, E. Eiser, Effect of Inert Tails on the Thermodynamics of DNA Hybridization. *Journal of the American Chemical Society* 2014.

## Declaration

This dissertation is the result of my own work and includes nothing which is the outcome of work done in collaboration except as declared in the Preface and specified in the text.

It is not substantially the same as any that I have submitted, or, is being concurrently submitted for a degree or diploma or other qualification at the University of Cambridge or any other University or similar institution except as declared in the Preface and specified in the text. I further state that no substantial part of my dissertation has already been submitted, or, is being concurrently submitted for any such degree, diploma or other qualification at the University of Cambridge or any other University or similar institution except as declared in the Preface and specified in the text

It does not exceed the prescribed word limit for the relevant Degree Committee. For more information on the word limits for Degree Committee for physics and chemistry.

Zachary Ruff

2017



## Acknowledgements

I would like to thank my supervisors Erika Eiser and Clare Grey for their guidance and mentorship. It has been a pleasure both to learn from Erika and Clare as scientists and to share in their commitment to the pursuit of academic research. Thank you to the current and former members of the Eiser group who I have worked with on DNA-mediated self-assembly, Lorenzo di Michele, Simon Nathan, Robert Unwin, Mykolas Zupkauskas and Thomas O'Neill. In the Grey group, I would like to thank Rajesh Jethwa for spending his part III chemistry project exploring the self-assembling battery concept with me, Nis-Julian Kneules for contributing his expertise in chemical synthesis and Clare and Dominic Wright for guiding and supervising the project. Thank you to all the members of the Eiser and Grey groups for the invaluable scientific discussions and support during this project. I would again thank Clare, Erika, Tom, Myk and Nis for their valuable comments as I prepared this thesis.

Research can be a challenging and solitary path and the support of family and friends near and far have made this thesis possible. I would like to thank my parents, Myra and Roy Ruff, whose love and support I can always count on. I have met an incredible group of friends during my time in Cambridge who seem to be from all over the world and have made my experience here truly rich. Finally, thank you to Magdalena Künkel for being by my side with her unwavering love throughout.

## Abbreviations

AuNP- gold nanoparticle  
DCM: dichloromethane  
DMF: dimethylformamide  
DMSO: dimethyl sulfoxide  
DNA: deoxyribonucleic acid  
DNA-NP: DNA coated nanoparticle  
DNACC: DNA-coated colloid  
dsDNA: double-stranded DNA  
EIS: electro-impedance spectroscopy  
fd- filamentous bacteriophage  
FTIR: Fourier transform interference spectroscopy  
MW-CNT: Multi-walled carbon nanotubes  
PB: phosphate buffer  
PBS: phosphate buffered saline  
PEG: polyethylene glycol  
PEG-NP- polyethylene glycol coated nanoparticle  
PM: polyethylene methacrylate  
SERS: surface enhanced Raman spectroscopy  
SiNP- silicon nanoparticle  
ssDNA: single-stranded DNA  
SW-CNT- single-walled carbon nanotubes  
THF: tetrahydrofuran  
UV-VIS- ultra-violet and visible

## Table of Contents

1	Introduction .....	11
1.1	Colloidal Self-Assembly .....	11
1.2	Colloidal Interactions.....	12
1.3	DNA Hybridization and Melt Curves.....	16
1.4	DNA-Functionalized Colloids .....	18
1.5	Colloidal Gelation and Spinodal Decomposition .....	20
1.6	Structural Color .....	23
1.7	Self-Assembled Batteries.....	25
2	Methods .....	27
2.1	Nanoparticle Synthesis and Characterization.....	27
2.1.1	Colloidal synthesis .....	27
2.1.2	Surface functionalization of colloids .....	28
2.1.3	Dynamic Light Scattering and Electrophoresis .....	32
2.1.4	Fluorescent Assays .....	33
2.1.5	UV-VIS and FTIR spectroscopy.....	35
2.2	Gel Imaging and Characterization .....	36
2.2.1	DNA-nanoparticle melt temperature measurements .....	36
2.2.2	Optical Microscopy.....	37
2.2.3	Image Analysis Techniques.....	40
2.2.4	Electron Microscopy.....	41
2.3	Measuring Bulk Properties of Nanoparticle Gels .....	42
2.3.1	Optical Spectroscopy .....	42
2.3.2	Electro-Impedance Spectroscopy .....	43
2.3.3	Raman Spectroscopy .....	45
2.3.4	Electrochemical measurements .....	48
3	Gold Nanoparticle Gels.....	50
3.1	Functionalization of gold nanoparticles with DNA .....	50
3.2	Thermally reversible aggregation of gold DNACC .....	54
3.3	Formation and fluorescent microscopy of DNA-gold nanoparticle gels.....	58
3.4	Electron microscopy of DNA-gold nanoparticle gels .....	61
3.5	Electro-impedance studies in Gold Nanoparticle Gels .....	64

3.6	SERS on Gold Nanoparticle Gels .....	71
4	Silica Nanoparticle Gels .....	75
4.1	Functionalization of Silica Nanoparticles.....	75
4.2	Microstructure of 100nm silica gels .....	85
4.3	Gels formation mechanism in 30 nm silica gels with DNA and PEG .....	88
4.4	Microstructure of DNA-PEG and PEG 30nm silica gels .....	91
4.5	Optical Spectroscopy and Nanostructure Analysis of Silica Gels.....	94
	Summary and Future work.....	99
5	Colloids, viruses and batteries.....	101
5.1	Structural Studies in Gold Nanoparticle Virus Composite Gels .....	101
5.2	Self-assembly of silicon nanoparticle and carbon nanotubes .....	108
5.2.1	Functionalization of carbon nanotubes.....	110
5.2.2	Functionalization of silicon nanoparticles .....	113
5.2.3	Silicon-carbon nanotube composite formation.....	116
5.2.4	Electrochemical measurements of silicon-carbon nanotube composite .....	118
6	Outlook.....	121
7	Appendix .....	123
7.1	Effect of Inert Tails on DNA Hybridization.....	123
7.2	Hydrosilylation of Silicon Nanoparticles with Polymers .....	125
8	References.....	127

# 1 Introduction

## 1.1 Colloidal Self-Assembly

Nanostructuring has led to materials with novel and improved properties driving innovation across fields as varied as transportation<sup>17</sup>, communications<sup>18</sup>, computing<sup>19</sup> and biotechnology<sup>20</sup>. However, forming three-dimensional macroscopic materials with feature sizes on the order of hundreds of nanometers remains a challenge for current materials processing techniques. Because of this, the benefits of nanostructuring have not been widely extended to large-scale, three-dimensional applications with perhaps the exception of structural materials. Deterministic pattern techniques have proved too expensive for applications outside of high value products for the semiconductor chip and optoelectronic industries. Colloidal self-assembly can potentially fill this important technological gap.<sup>21</sup> In this thesis, the concept of colloidal self-assembly to form functional materials is explored.

Self-assembly is a widely accepted concept for synthesizing low-cost three-dimensional nanostructured materials and is amply studied in the scientific literature.<sup>22</sup> Top-down patterning methods, such as interference lithography<sup>23</sup>, have been successful in creating planar geometries on the macro-scale. By contrast, bottom up techniques, such as those using block copolymers, can be designed to self-assemble in three dimensions<sup>24</sup>, but these systems are limited to feature sizes of tens of nanometers and a finite thickness of microns. In colloidal self-assembly, the attraction potentials between colloids can be tuned to form materials with short-range order and characteristic length-scales spanning tens of nanometers to tens of microns. There are numerous examples in the literature that take advantage of depletion forces<sup>25</sup> and electrostatic interactions<sup>6</sup> to self-assemble colloids into macroscopic structures. Coating colloids with DNA introduces an additional route for controlling the interaction potentials between particles and DNA-coated nanoparticles are used as a model system for studying colloidal self-assembly.<sup>26-28</sup> These studies are later extended to include nanoparticle assemblies formed using polymer interactions and covalent bonding.

DNA-functionalized nanoparticles demonstrate highly specific, tunable and thermally reversible binding. This unusual combination of properties makes DNA-functionalized nanoparticles a useful model system for studying self-assembly. DNA (Deoxyribonucleic acid) is of course best known for coding the genetic information of life and has a double-helix

structure consisting of two anti-parallel intertwining sugar-phosphate backbones covalently bonded to one of four bases: Adenine, Cytosine, Guanine and Thymine (A, C, G, T). The oligomers are held together by hydrogen bonding between complementary base pairs with specific bind rules, where A can only bind to T and C can only bind to G. Synthetic single-stranded DNA (ssDNA) with arbitrary sequences is now routinely and inexpensively produced both in the lab and commercially. The rapid growth of the biotechnology industry has led to the development of simple methods for attaching a variety of linker, spacer and dye-molecules to synthetic DNA.

Although nanoparticles have been used since antiquity, an appreciation of their size dependent properties is more recent. Metallic, oxide, molecular and polymeric nanoparticles have found a wide-variety of applications. However, some of the initial enthusiasm for taking advantage of their unique optical, semiconducting and catalytic properties has been tempered by the difficulty in forming assemblies and higher order structures. Directing the assembly of nanoparticles with various ligands, surfactants and block copolymers remains an important area of scientific research. The specificity and reversibility of DNA binding make the oligomers a particularly useful system for studying both the science underlying the directed self-assembly of nanoparticles and its potential device applications. This thesis focuses on the photonic, plasmonic, electronic and electrochemical applications for DNA self-assembly, since they appear to be especially good candidates for taking advantage of the properties of colloidal self-assembly.

## 1.2 Colloidal Interactions

Colloids can be described as particles made up of a collection of atoms or molecules subject to Brownian motion where the bulk properties rather than a detailed description of its constituent materials determine the particle's behavior. Since colloidal behavior is subject to the laws of statistical mechanics and subject to thermal motion, we can define an upper limit to the size of colloids based on the average height distribution of a colloid in a suspension:

$$\langle height \rangle = \frac{k_b T}{\rho g}, \quad (1)$$

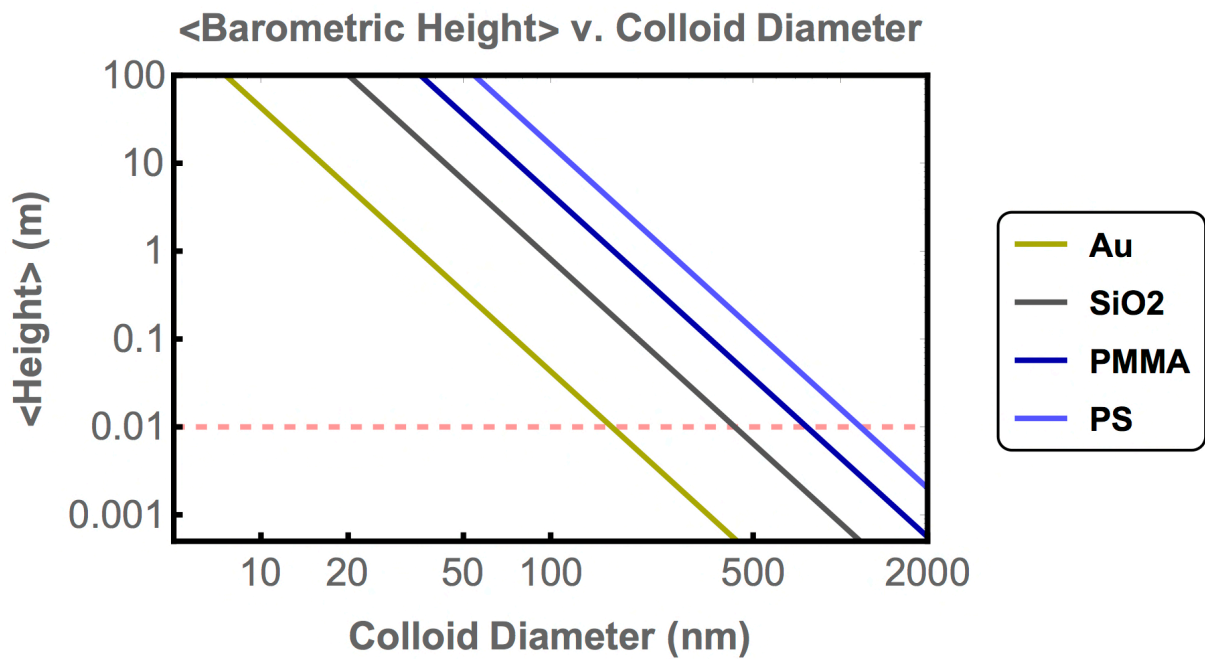


Figure 1: Barometric Height as a function of materials density plotted with log-log axis where  $\rho_{\text{Au}}= 19.3 \text{ g/cm}^3$ ,  $\rho_{\text{SiO}_2}= 2 \text{ g/cm}^3$ ,  $\rho_{\text{PMMA}}= 1.18 \text{ g/cm}^3$ , and  $\rho_{\text{PS}}=1.05 \text{ g/cm}^3$ . Dashed line is at  $\langle\text{height}\rangle= 1 \text{ cm}$ .

where  $\rho$  is the difference in density between the colloid and the surrounding media. It is preferable to work with colloids that are not significantly impacted by gravity, such that they are distributed uniformly in the sample volume in the freely-dispersed phase and only interact when subject to attractive colloidal forces. Figure 1 shows the average height distribution or barometric height for colloids consisting of materials with different densities as a function of colloid diameter. The dashed line at 1 cm defines an approximate value where the colloids have a gravitation height that is less than the height of the sample chambers holding the colloidal dispersions.

Colloidal suspensions are subject to an interplay of forces that can be summed to an effective interaction called the potential of mean force. The different contributions to the potential of mean force are discussed below. The contributions of DNA hybridization can simply be added to the potential of mean force as an additional term.

Dispersion forces or Van der Waals forces are quantum mechanical in origin and arise through fluctuations of the dipole moments in atoms or molecules. They are relatively long-range forces that can span from the length-scale of interatomic spacing to distances greater than 10 nm.<sup>29</sup> A full description of interactions between colloids requires Lifshitz theory and will not be discussed. To calculate the interaction between two colloids, a useful approximation is usually made; molecular dipoles do not interact, the total interactions can

be treated as additive and the interactions are not subject to retardation effects. Retardation effects occur when two atoms are at a sufficient distance apart that the time it takes for the electric field of the first atom to reach the second and return becomes comparable with the period of the fluctuating dipole itself leading to a fast decay of the dispersion energy with distance ( $\sim 1/r^7$  v.  $\sim 1/r^6$ ).<sup>29</sup> Under these assumptions, the interactions between two like spherical colloids can be calculated by integrating the dispersion interaction between two atoms or molecules:

$$u_{disp}(r) = -\frac{C_{disp}}{r^6}, \quad (2)$$

where  $C_{disp}$  depends on the polarizability of the individual atoms or molecules, over the volume of the two colloids to obtain the expression,

$$U_{disp}(r) = -\frac{A}{6} \left( \frac{2R^2}{r^2-4R^2} - \frac{2R^2}{r^2} + \ln \left( \frac{r^2-4R^2}{r^2} \right) \right), \quad (3)$$

where  $R$  is the radius of the colloid and  $A$  is the Hamaker constant, accounting for the dielectric properties of the colloids and the solvent.

Colloids in solution will almost always have an electrostatic charge on their surface. The surface charge can originate through interactions with the surrounding liquid in two main ways. First, surface groups on the colloid can ionize or dissociate leaving behind a charge. Alternatively, ions from solution can absorb or bind the colloid surface introducing a charge onto a previously neutral surface. In either case, counter ions of the opposite charge will be electrostatically attracted to the colloid surface to balance out the surface charge. Some counter ions will form a tightly bound layer, the Stern or Helmholtz layer, and others will be distributed in a diffuse electric double-layer radially outward from the colloid. The electric potential due to the surface charge decays from the surface exponentially under a Boltzmann distribution.

The first expression describing the electronic and dispersive contributions to the potential of mean force between two like spherical colloids was proposed independently by Derjaguin and Landau<sup>30</sup> and by Verweij and Overbeek<sup>31</sup>. The model is therefore commonly referred to as DLVO theory. The DLVO expression for the electric potential includes several approximations including low surface charge and no interaction between ions. For two like

spherical colloids the electrical potential in the DLVO model at a distance  $r$  from the surface of a colloid is given by:

$$U(r) = \left( \frac{Qe^{\kappa R}}{1+\kappa R} \right)^2 \left( \frac{e^{-\kappa r}}{2\pi\kappa r} \right), \quad (4)$$

where  $Q$  is the charge on the colloid,  $R$  is the radius of the colloid and  $\kappa$  is the decay constant. In the limit of low potentials (below  $\sim 25$  mV), the Debye-Huckel approximation, a simplified expression for  $\kappa$  can be expressed as a function of physical constants:

$$\kappa = \sqrt{\frac{2 e^2 n_0 z^2}{\varepsilon \varepsilon_0 k_B T}}, \quad (5)$$

where  $n_0$  is the salt concentration in solution,  $z$  is the charge of the ions in solution,  $\varepsilon$  is the dielectric constant of the solvent, and  $T$  is the absolute temperature. The inverse of the decay constant ( $1/\kappa$ ) is a common measure of the thickness of the electric double layer and is known as the Debye-screening length.

The full expression for the DLVO potential for two like spheres is obtained by adding the dispersive and electrostatic contributions to give the expression:

$$U_{DLVO}(r) = \left( \frac{Qe^{\kappa R}}{1+\kappa R} \right)^2 \left( \frac{e^{-\kappa r}}{2\pi\kappa r} \right) - \frac{A}{6} \left( \frac{2R^2}{r^2-4R^2} - \frac{2R^2}{r^2} + \ln \left( \frac{r^2-4R^2}{r^2} \right) \right). \quad (6)$$

The behavior of colloids in solution is well described by the DLVO model. At short distances ( $r \rightarrow 0$ ), dispersive term dominates due to the power law term and there is a minimum in the DLVO potential. However, at distances  $r$  away from the colloid, the net potential can be repulsive depending on the relative strength of the electrostatic term creating an energy barrier against aggregation. For colloids with highly charged surfaces in dilute electrolytes (a long Debye length), the electrostatic term will dominate leading to a strong repulsive potential and colloids that are stable against aggregation. For colloids with a low surface charge density in concentrated electrolytes, the dispersion term again dominates, the energy barrier disappears, and the colloids attract and aggregate. At intermediate electrolyte concentrations and surface charge densities, a weaker, secondary minimum can appear in the potential at separation distances greater than that of the primary minimum. Here, the energy

barrier to reach the primary minimum is too high to overcome and the colloids will either remain in the secondary minimum or remain dispersed.

Three other colloidal interactions need to be considered in colloidal solutions, hard-core repulsion, steric repulsion and depletion. Colloids are solid materials that do not interpenetrate due to hard-core repulsion forces. At short distances, interactions between non-reactive atoms are highly repulsive due to the Pauli exclusion principle. Hard-core repulsion is the repulsive force responsible for the primary minimum that occurs in DLVO theory.

Steric repulsion occurs when ligands such as polymers are bound to the surface of a colloid in good solvent conditions. When two colloids approach each other in solution, the local concentration of polymer in solution increases, causing the osmotic pressure to repel the two colloids due to decreased entropy. At sufficient grafting densities, steric repulsion can be used to overcome attractive forces and stabilize colloidal suspensions.

Depletion interactions arise when well-solvated and non-absorbing polymers or well-dispersed particles are present in colloidal solutions. Depletion interactions are attractive forces driven by the solvent and not a force originating from colloids themselves. These non-interacting depletants are excluded geometrically from a volume near the surface of the colloids. When the depletion volumes of two colloids overlap, the colloids will undergo an attractive force due to the osmotic pressure difference between the depletion volume and the bulk solution.

### 1.3 DNA Hybridization and Melt Curves

Grafting DNA to the surface of nanoparticles contributes to the potential of mean forces in colloidal suspensions primarily in three ways. First, the negatively charged sugar-phosphate backbone modifies the electrostatic potential of colloid. Second, since DNA is an oligomer ( $\approx 0.34$  nm long per base pair),<sup>32</sup> DNA grafted to the colloids can provide a steric barrier to aggregation at sufficient coating densities. At low grafting densities, single-stranded DNA (ssDNA) in good solvent conditions forms a coil near the colloid surface, since it has a persistence length of  $\approx 1$  nm (**Error! Reference source not found.**)<sup>33</sup> However, as more ssDNA is grafted onto the colloid, the DNA chains straighten to form a rigid brush due to the repulsive interactions between the DNA oligomers due to both electrostatic repulsion and solvation forces. Double-stranded DNA (dsDNA) is more rigid due to its double helix structure having a

persistence length of  $\sim 35\text{nm}$ .<sup>34</sup> As a result, dsDNA generally provides a greater amount of steric repulsion than ssDNA, especially at low grafting densities.

The third contribution is the Watson-Crick base pairing that creates an attraction between complementary strands of DNA due to hydrogen bonding between bases.<sup>32</sup> The free energy of DNA hybridization is a function of the number of base pairs in the binding sequence and the specific base pair sequence, since A and T binding is mediated through two hydrogen bonds, while C-G binding is mediated through three hydrogen bonds. SantaLucia developed a nearest neighbor model which is widely used for predicting the free-energy of hybridization between ssDNA strands.<sup>35, 36</sup> Each base-pair contributes  $1-3 k_B T$  to the free-energy of hybridization giving the ssDNA strands used in this thesis (7-10 base-pairs) hybridization energies on the order of tens of  $k_B T$  at room temperature. Therefore, when hybridized, these DNA strands are unlikely to become unbound at room temperature. However, at higher temperatures the entropic energy exceeds the energy of the hydrogen bonding and the ssDNA dissociate.

The hybridization of DNA bound to colloids is a collective phenomenon that involves all bases in the interaction volume between colloids' surfaces. For colloids with high DNA grafting densities involving tens of DNA strands, the free-energy of hybridization will be hundreds of  $k_B T$  and be on the order of magnitude as covalent bonds.<sup>29</sup> Despite the high attractive energy at room temperature, the potential of mean force between DNA-coated colloids eventually becomes repulsive at higher temperatures as the free-energy of hybridization no longer exceeds the repulsive electrostatic and entropic energies.

The degree of hybridization between two complementary strands of DNA can be measured using UV absorption spectroscopy. At 260nm, single-stranded DNA has a 37% greater extinction coefficient than double-stranded DNA.<sup>37</sup> By heating and cooling solutions of complementary DNA strands, association/disassociation curves can be generated as a function of temperature. They are referred to as "melt" curves, where the melting temperature is defined as the point where 50% of the DNA is hybridized. The melt curves for free DNA oligomers is much more gradual relative to DNA grafted to colloids (**Error! Reference source not found.**).<sup>28</sup> Both increasing the grafting density and the number of base pairs in the ssDNA will steepen the melt transition and shift the melt curve to higher temperatures. This effect follows from the collective binding of DNA grafted to colloids. In

section 2.2.1, the utility of melt curves for extracting the free energy of DNA hybridization will be discussed.

#### 1.4 DNA-Functionalized Colloids

DNA-functionalized colloids or DNA-coated colloids (DNACCs) first appeared in the literature in a 1996 issue of *Nature* where both Alivisatos<sup>27</sup> and Mirkin<sup>26</sup> described a process for attaching DNA to the surface of gold nanoparticles. The novelty of the approach was built on a well-known process for attaching molecules to gold surfaces using alkane-thiols. Previously, thiol chemistry had been used to aggregate gold nanoparticles through irreversible bridges.<sup>38, 39</sup> By replacing the alkane-thiols with short ssDNA oligomers, they were able to demonstrate thermally reversible aggregation. In subsequent works, Mirkin et. al.<sup>40-42</sup> and Gang et. al.<sup>15, 43, 44</sup> studied both the variables contributing to the surface coating and the phase behavior of DNA-functionalized gold nanoparticles.

Depending on the properties of the DNACCs and the kinetics of the colloidal assembly, DNACCs will form amorphous aggregates, phases with short-range order or colloidal crystals with both short and long-range order (Figure 2). The degree of order in the aggregated phase is determined by both the strength of the colloidal interaction and the cooling rate from the gas phase. Most structural studies of DNA mediated nanoparticle aggregates have focused on the formation of colloidal crystals.<sup>15, 42, 44-46</sup> By changing the inter-particle distance and colloid diameter, a wide variety of crystal structures have been demonstrated in nanoparticle superlattices.<sup>46, 47</sup> While colloidal crystals made from DNACCs are interesting as model systems for understanding atomic structures and for forming micro-assemblies, they may be

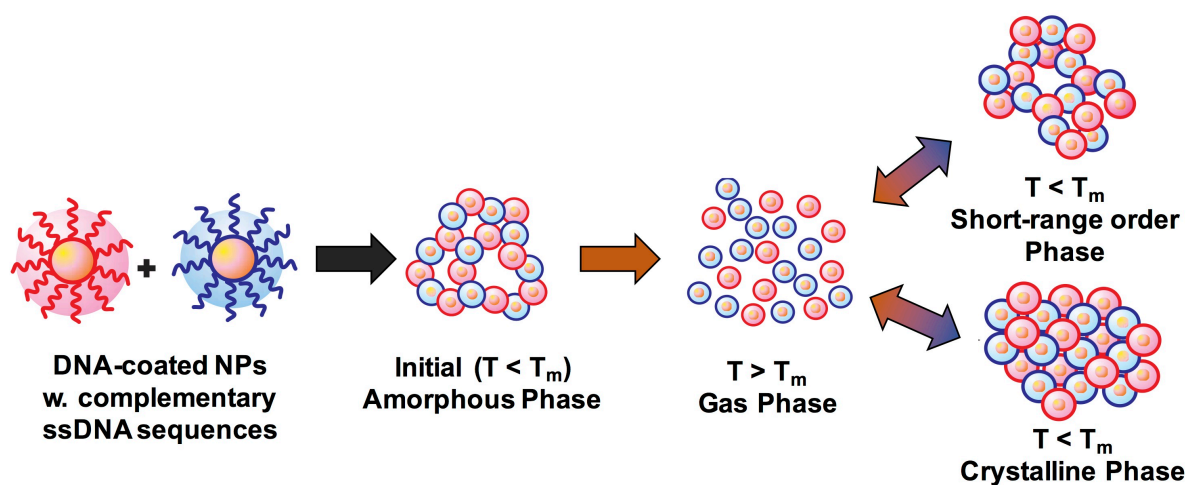


Figure 2: Phase behavior of DNA-functionalized nanoparticles. The degree of order in the aggregated phase is determined by both the strength of the colloidal interaction and the cooling rate from the gas phase. Figure adapted with permission,<sup>15</sup> Copyright 2008, Macmillan Publishers limited.

unsuitable for forming larger crystals. The long timescales necessary for achieving the crystalline phase in systems with strong attraction appear to be impractical due to both the sharp phase transitions inherent to densely coated colloids and long timescales associated with colloidal diffusion. Although originally there was little interest in DNACCs with short-range order, more recent studies have begun to study their properties and possible applications for three-dimensional self-assembly.<sup>13, 21, 48</sup> Unlike systems under thermodynamic equilibrium, phases with short-range order can form macroscopic three-dimensional constructs with well-defined porosity within seconds.<sup>8, 13</sup>

After the initial demonstration of attaching DNA to metallic nanoparticles, DNA was grafted to micron-sized polymer spheres using avidin and biotin, a protein couple with a high binding constant. Such DNA-functionalized micron-sized polymer spheres have been used to form clusters<sup>48-50</sup> and even small colloidal crystals<sup>51</sup> under specific conditions, despite the sharp melt behavior of the aggregate due to the large number of DNA strands involved in the binding of microspheres. Our group later demonstrated the utility of using the DNACCs to form macroscopic percolating colloidal gels using polystyrene microspheres.<sup>48</sup>

The sequence specific, selective interactions of DNACC opens the possibility of forming colloidal gels with more complex morphologies than is accessible in colloidal systems with only short-range attraction potentials. Our group demonstrated the novelty of the selective binding accessible in DNACC systems with two sets, A and B, of 0.5 micron polystyrene colloids.<sup>13, 21, 52</sup> In this system, the A-colloids are coated with complementary DNA (A and A') and the B-colloids are coated with complementary DNA (B and B') such that only A-colloids can bind to A-colloids and only B-colloids can bind to B-colloids, but that the two sets cannot bind to each other. At high temperatures, both the A and B colloids are in the gas phase, since all colloidal interactions are repulsive. As the temperature is decreased to below the melt temperature ( $T_m$ ), A-colloids begin to bind to A-colloids and B-colloids begin to bind to B-colloids and the system begins to phase segregate. At low temperatures, the system forms two independent interpenetrating of gels (bigels), where all colloids of a given type (A or B) are in contact with a colloid-poor gap between the two networks. Figure 3 shows a simulation of the phase segregation in this two-component system.

The de-mixing in the two-component system occurs through a kinetic-arrested spinodal decomposition mechanism.<sup>13, 21, 52</sup> Similar to spinodal decomposition in atomic systems, as the colloids are quenched from the gas-phase, density fluctuations grow rapidly

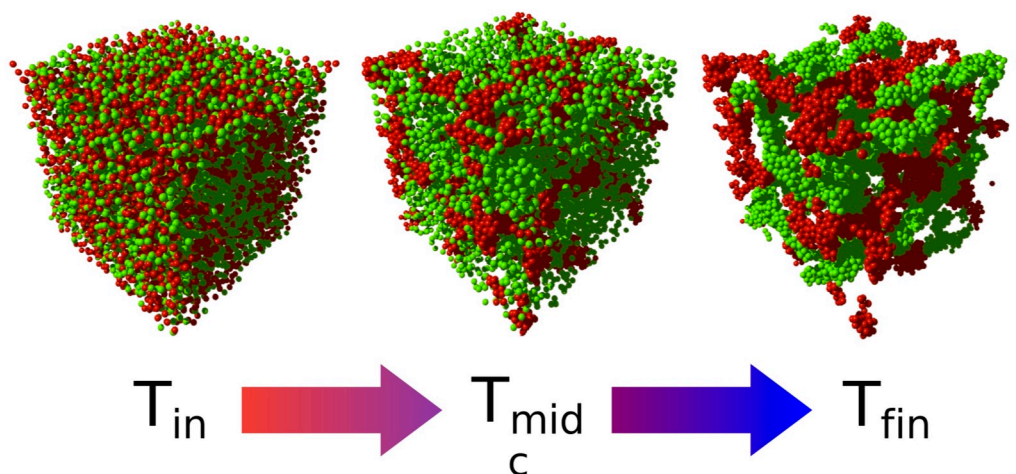


Figure 3: Bigel formation through spinodal decomposition in a two-component system with A-colloids (green) and B-colloids (red). Figure adapted with permission,<sup>13</sup> Copyright 2013, Macmillian Publishers limited.

due to the favorable colloidal interactions. The growth of the phase separation will then be arrested due to the high energy of collective DNA binding, which prevents coarsening of the gel networks. In the absence of non-specific interactions, two phases will be compositionally pure since non-complementary colloids will repel.

Alternative strategies such as multistep aggregation also can be used to form gels with a core-shell structure. In this case, two complementary DNA sequences A and B were designed with  $T_{m,A} > T_{m,B}$  ( $T_{m,A} - T_{m,B} \approx 10^\circ\text{C}$ ), such that when  $T_{m,A} > T > T_{m,B}$ , the A-red colloids will gel and the B-green colloids will remain in a gas phase. When the temperature is reduced such that  $T < T_{m,B}$ , the B-green colloids will then form an independent gel in the free volume. Conversely, a similar system can be designed with binding rules such that A and B colloids can bind, but the B colloids are coated with DNA with a shorter binding motif. In this case, the A colloids will form a gel when the sample is quenched below  $T_{m,A}$ , while the B colloids will remain in the gas phase. When sample is subsequently cooled to below  $T_{m,B}$ , the B colloids will coat the A network of colloids, forming a gel with a core-shell structure.

### 1.5 Colloidal Gelation and Spinodal Decomposition

Colloidal gelation can be driven by either attractive or repulsive potentials of both weak and strong energies over a range of interaction distances. This thesis focuses on the gelation of colloids with relatively short-range, attractive potentials with energies covering those that are relatively weak (few  $k_B T$ ) to very strong ( $100 k_B T$ ). When the interaction energies between colloids are weak, colloids can rearrange due to thermal motion. However, once the

interaction becomes greater than approximately  $10 k_B T$ , colloids can no longer dissociate due to thermal motion and can be considered trapped or “arrested” in the aggregated state.

Figure 4 is a sketch of a phase diagram for a one-component colloidal solution with an attractive potential and reversible aggregation. Above the two-phase region, it is possible to form three distinct phases. At low volume fractions, colloids can form short-lived clusters due to the finite probability that the colloids will aggregate, which then quickly dissociate due to thermal energy. As the volume fraction increases, there can be a transition to where there are sufficient transient clusters to percolate the full sample volume. At sufficiently high volume fractions, the clusters become longer lived such that they remain in place for a sufficient time,  $\tau$ , that the phase can be considered glassy. The transition between the gel and the glassy state is often defined by  $\tau$ , the time it takes for a colloid to diffuse one colloid diameter away from its original position, with the time  $\tau = 100$  seconds demarcating the transition between the two states.<sup>6</sup>

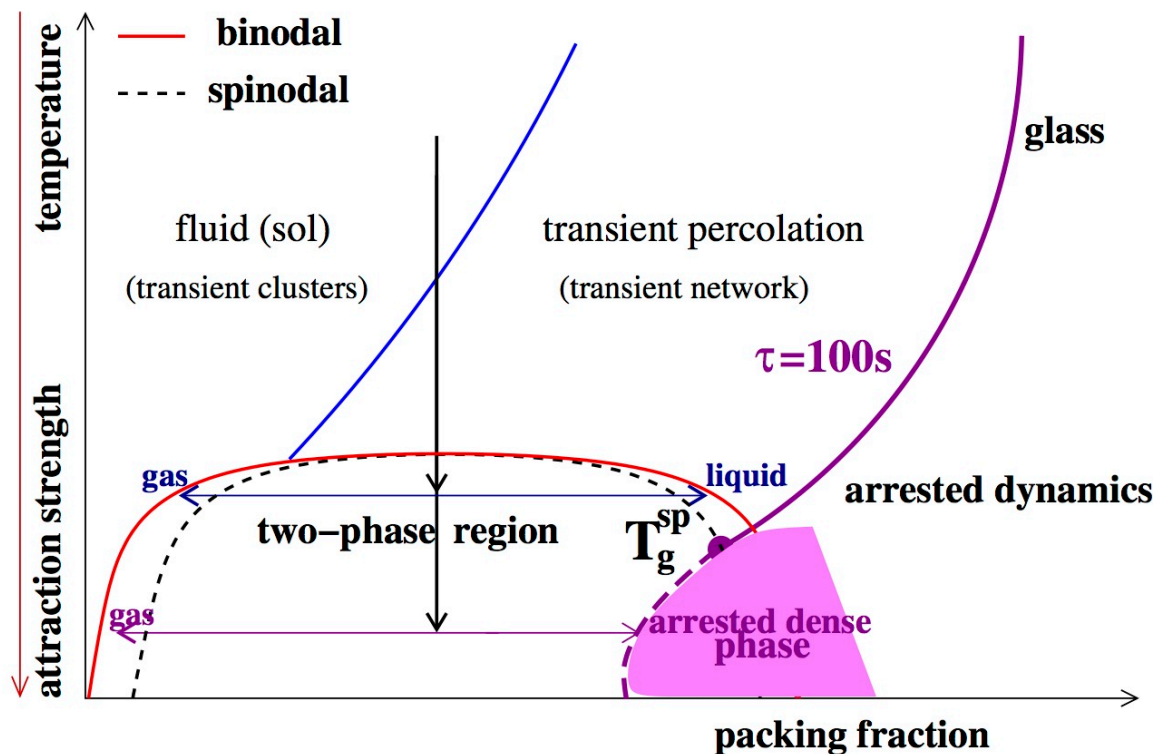


Figure 4: A sketch of a phase diagram of colloids with attractive potentials. When quenched into the spinodal, the colloids separate in a colloid-rich arrested phase and a colloid poor gas phase. Figure adapted with permission,<sup>6</sup> Copyright 2007, IOP Publishing LTD.

By cooling a colloidal dispersion into the two-phase region, the colloids will phase separate into a colloid-poor, gas phase and a colloid-rich, dense (aggregated) phase. If cooling into the two-phase region is sufficiently slow and the attractions are sufficiently weak that the colloids can rearrange, the colloids will crystallize. However, if the cooling is fast, the colloids will instead form a gel without long-range order. In Figure 4, the distance between the spinodal and binodal line defines where crystallization can occur if kinetic traps are avoided and colloids can reconfigure in experimentally relevant time-scales. This regime is achieved in DNACCs by using either small nanoparticles<sup>15</sup> or larger colloids with very short DNA binding sequences<sup>53</sup> over the timescale of days. Conversely, in systems consisting of larger colloids with strong interaction energies, the spinodal and binodal lines overlap and the crystalline phase is experimentally inaccessible.

Figure 5 shows a simplified phase diagram for thermally-reversible colloids with strong, short-range attractive potentials below the two-phase region and strongly repulsive potentials above it, which is the case for the DNACCs in this work. Above the two-phase region, there is a colloidal gas, since the strong, repulsive potential keeps the colloids from associating. By cooling the dispersion into the two-phase region, the potential transitions from repulsive to attractive, driving the phase separate into a kinetically-arrested, colloid-rich gel and a colloid-poor gas. The strong attraction between colloids suppresses colloidal rearrangement, preventing crystallization.

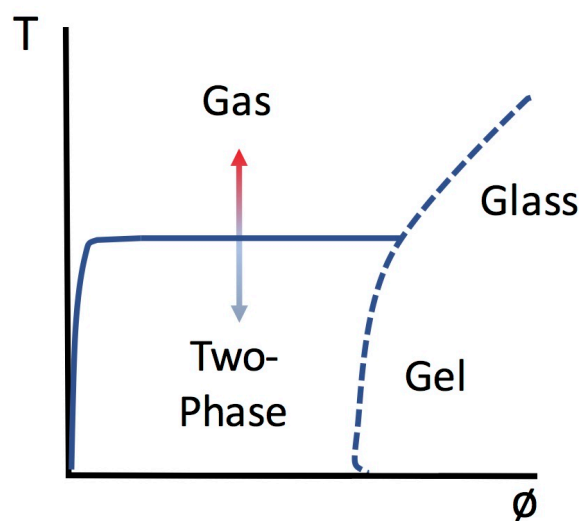


Figure 5: A sketch of a simplified phase diagram of strongly attractive colloids in solution undergoing a thermally reversible phase transition from a colloidal dispersion to colloidal gel. The strong attraction between colloids in the two-phase region suppresses colloidal rearrangement and prevents crystallization.

To form colloidal gels with short-range order, it is the transition from the homogeneous gaseous phase to the two-phase region that we are interested in. The transition typically is driven by reducing the temperature of a colloidal dispersion, although we will see later in section 5.2 that it can also be induced by external stimuli, such as covalent bonding under UV irradiation. We will also see that in systems with weaker attraction potentials, such as the PEG-coated silica colloids in section 4.3, the colloids can rearrange over time.

## 1.6 Structural Color

Materials can preferentially reflect or transmit color due to their underlying nanostructure rather than from the selective absorption of certain wavelengths of light. This phenomenon occurs in systems with short range order and feature sizes on the order of hundreds of nanometers. At this length-scale, light is scattered due to the spatial variation in the optical polarizability of the nanostructure. Structural colored materials can be separated into two classes of systems, those with and without long-range order.<sup>5</sup> Color derived from materials with long-range order have been studied extensively and are well understood. The strong

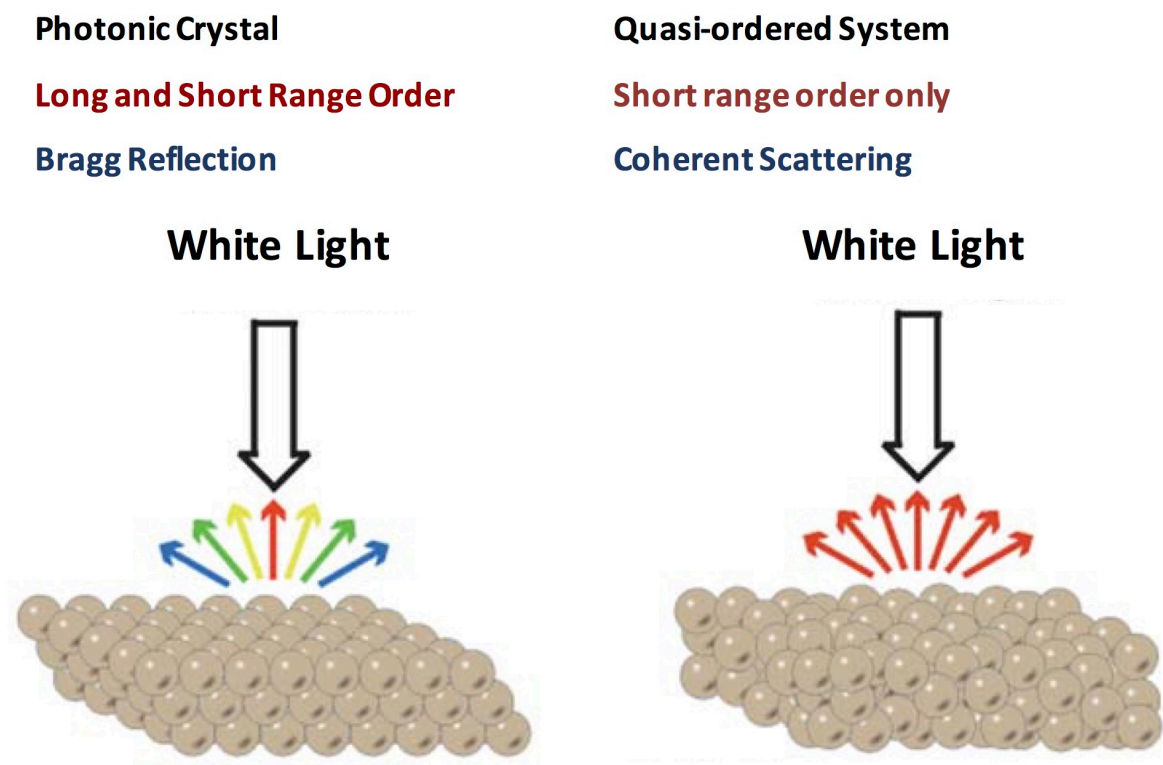


Figure 6: Structural color from photonic crystals and weakly ordered systems. Figure adapted with permission from reference,<sup>5</sup> Copyright 2012, Royal Society of Chemistry.

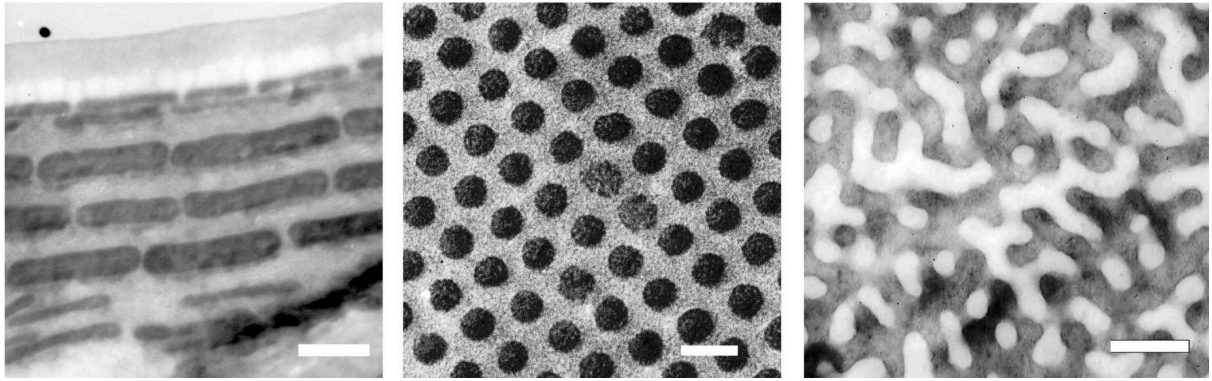


Figure 7: Examples of the three main nanostructures of bird feather that display structural color from coherent scattering. Laminar array of plates (left), Hexagonal arrays (middle) and quasi-ordered arrays (right). The scale bar in all figures is 200nm. Figure adapted with permission from reference,<sup>7</sup> Copyright 2003, Oxford Academic.

periodicity (photonic crystals) leads to photonic bandgaps displaying vivid, angle dependent coloration. The periodicity of photonic crystals can be in one, two or three dimensions and there are many realized and potential applications for these devices such as Bragg mirrors, photonic crystal fibers and negative refractive index materials.

Materials with only short-range order are beginning to gain interest, particularly as pigments.<sup>54, 55</sup> The lack of long-range order makes these materials isotropic, leading to angle-independent coloration. Although only recently has there been a push to develop artificial examples of these systems, coherent scattering has been appreciated by biologists for some time.<sup>7, 56-58</sup> In bird feathers, structural color can derive from structure with and without long range order (Figure 7). In chapter 4, self-assembling nanostructures that resemble the quasi-ordered arrays in bird-feathers are discussed.

Much of the recent work on creating angle-independent structural color in synthetic systems has been performed in colloidal systems. The Takeoka group have demonstrated angle-independent structural color in gels of soft<sup>59</sup> and hard<sup>60</sup> colloidal suspensions. The Manoharan group have formed materials with isotropic color by condensing suspensions of core-shell particles using depletion forces<sup>61</sup> and osmotic pressure in microfluidic droplets.<sup>54</sup> In these systems, the colloid diameter or form factor defines the length-scales in the system or structure factor. Therefore, the optical response of these systems cannot be decoupled from the scattering cross-section of the individual colloid and the scattering of the system is proportional to the product of the two:

$$\text{Form Factor} \times \text{Structure Factor} \propto \text{Total Scattering}. \quad (7)$$

It will be shown how the form factor of the colloidal gel can be decoupled from the form factor of the colloidal building blocks and the structure factor of the colloidal gel by using colloids sufficiently small that they have a negligible optical scattering cross-section when they are freely dispersed (gas phase). Only when the particles are aggregated (gel phase) do they scatter light.

## **1.7 Self-Assembled Batteries**

The nanostructuring of electrodes is a recognized opportunity for improving battery performance.<sup>62, 63</sup> Three-dimensional nanostructures are particularly promising, as they can enable idealized battery geometries for optimizing both the power and energy density of batteries.<sup>63</sup> Battery cycling rates are typically limited by the kinetics at the electrode interfaces, mass and ionic transport through the bulk materials or by thermal and mechanical damage to the cell. Nanostructuring can potentially address each of these performance limitations by increasing both the interfacial surface area in a battery and increasing the mass of electrode material in contact with the electrolyte. Bringing the cathode, anode and electrolyte within tens to hundreds of nanometers, makes ionic and mass transport less critical. The shorter transport distances decrease the amount of resistive heating and associated damage. Furthermore, nanostructured devices can also better accommodate the stress associated with an electrode's volume expansion as ions are incorporated into the high capacity materials.

Three-dimensional battery geometries address a common design trade-off between power density (charge/discharge rate) and energy density (total capacity). As an example, to enable high power densities, portions of the electrode material are often replaced with a conductive component, usually carbon, compromising energy density. Decoupling this trade-off will be critical as demand for higher performance batteries requires improvements to both figures of merit.

A variety of methods for forming three-dimensional batteries from colloids have been proposed and extensively reviewed.<sup>62-64</sup> Colloidal templating of polymer spheres has been used to form scaffolds upon which to electrodeposit battery materials.<sup>14, 65, 66</sup> Block copolymer templating also can be used to form mesoporous structures of electrode materials for batteries<sup>67</sup> and capacitors<sup>68</sup>. Although both approaches have been used to form devices

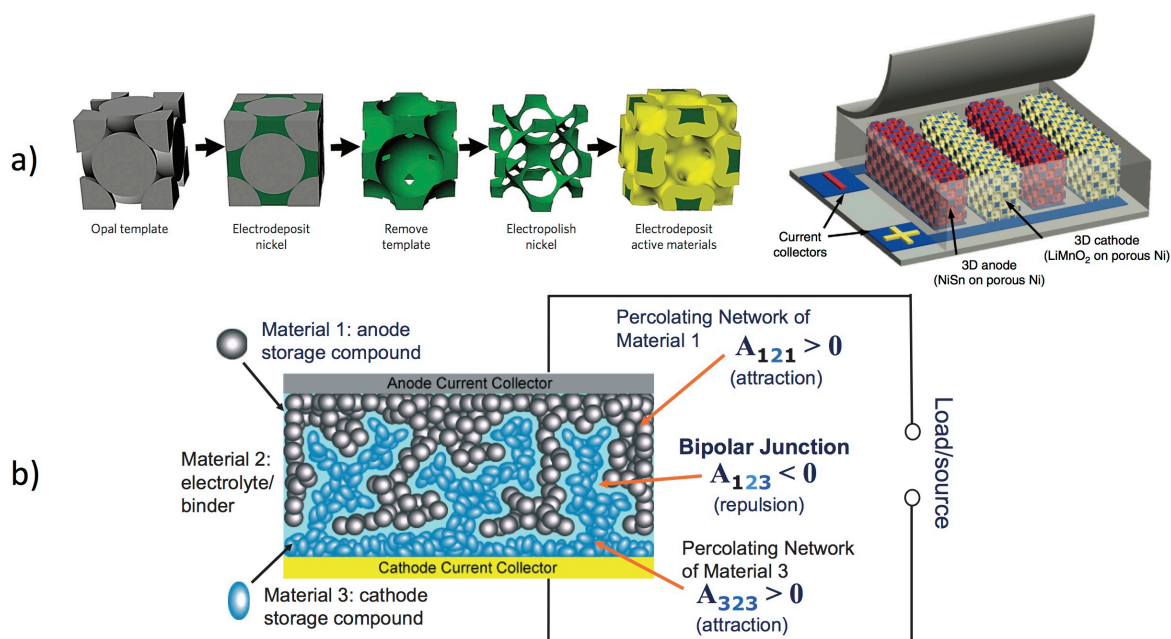


Figure 8: a) 3D batteries formed by Electrodeposition on a opal structure fabricated by colloidal templating. Figure adapted with permission from reference,<sup>14</sup> Copyright 2011, Macmillian Publishers limited. b) 3D batteries formed by dispersion forces. Figure adapted from reference,<sup>16</sup> Copyright 2007, Wiley-VH.

with impressive performance, the electrodes synthesized by colloidal and block copolymer templating are limited to microns in thickness and do not appear to be scalable for practical devices. Since electrodes made through colloidal self-assembly are fundamentally three-dimensional, they in principle do not suffer from these limitations. Self-assembly of colloidal batteries has also been demonstrated through dispersion forces<sup>16</sup> and graphical depiction of the battery is shown in Figure 8.

Extending the concept of using the specific interactions of DNACCs to form functional materials was originally a motivation for this thesis. The interpenetrating network bigel structure is an interesting concept for creating electrochemical devices optimized for having high surface areas and short distances between electrodes. The core-shell bigel structure resembles a bulk hetero-junction structure concept that has previously been explored for solar cell applications.<sup>69</sup> However, using DNA-mediated assembly was not explored in these systems, since the distance between DNACCs is too large to allow for significant electrical conduction between them, as will be shown in section 3.5. In chapter 5, covalent bonds are substituted for DNA-mediated interactions to overcome this challenge.

## 2 Methods

### 2.1 Nanoparticle Synthesis and Characterization

#### 2.1.1 Colloidal synthesis

The nanoparticles in this work were synthesized through the precipitation of molecular precursors in solution. The precursors precipitate forming small seeds with diameters on the order of a nanometer and then grow either by absorbing more material from the additional precursors or aggregating with other seed particles. A range of parameters can be tuned to achieve monodisperse spherical particles including the solvent, precursor concentrations and surfactants. Due to the commercial availability of nanoparticles with a range of diameters and surface functionalities, nanoparticles were often purchased, rather than synthesized. Nonetheless, both gold and silica nanoparticles were synthesized to gain greater familiarity with the formation process.

##### **Gold nanoparticle synthesis**

Gold nanoparticles can be synthesized easily by reducing gold perchlorate ( $\text{HAuCl}_4$ ) in sodium citrate ( $\text{C}_6\text{H}_9\text{Na}_3\text{O}_9$ ) in an aqueous one-pot reaction. 500ml of 1.0 mM gold perchlorate in Millipore water was heated in a glass flask to 95 °C. After 30 minutes, a warm solution of 50 ml of 38.8 mM sodium citrate was added to the gold solution. After the solution turned red, the flask was heated for an additional 30 minutes and then the solution was allowed to cool overnight. The nanoparticles were then stored in the dark in a refrigerator at 4 °C for later use. The resultant nanoparticles were approximately 13 nm in diameter.

##### **Silica nanoparticle synthesis**

Silica nanoparticles can be synthesized from solution to form relative monodisperse colloids using the Stöber sol-gel process.<sup>70</sup> Although the silica colloids used in this thesis were purchased from commercial sources, silica colloids were prepared using the Stöber process to gain familiarity with the synthesis technique and the potential for silica colloids can be produced at scale. In a typical synthesis, 44.5 ml of Millipore water was mixed with 5 ml of absolute ethanol and 0.5 ml of 25% aqueous ammonia and stirred for 30 minutes in a round bottom flask. Next, 1 ml of TEOS (tetraethyl orthosilicate) was added to the solution and allowed to react for 24 hours with stirring. The resultant silica nanoparticles were approximately 100 nm in diameter.

### 2.1.2 Surface functionalization of colloids

Developing reliable and reproducible protocols for functionalizing nanoparticle surfaces was critical to this work. In addition to identifying reactions with high yields, colloidal interactions need to be considered carefully to maintain stable dispersions during surface modification. Since DNA is a charged oligomer, additional ions need to be added to the reaction solution to electrostatically screen the DNA from the colloids during the coating process. However, the addition of salt also reduces the Debye length of the colloids, potentially leading to aggregation. To circumvent this challenge, two approaches were used; the nanoparticle dispersions were either salted gradually during the functionalization process or the particles were sterically stabilized during the chemical reactions between functional groups on the surface of the colloids and ends of DNA.

At the start of this thesis, there were limited protocols for coating nanoparticles with DNA other than noble metal nanoparticles using thiols. Therefore, it was necessary to develop new strategies to functionalize the silica used in Chapter 4. During this thesis, new approaches were published that paralleled the approach taken in this thesis verifying the strategy. The detailed protocols for functionalizing the gold, silica and biological (viruses) colloids with DNA are described in this section as well as the chemical modification routes for introducing functional handles to silicon nanoparticles and carbon nanotubes.

#### **Gold nanoparticle functionalization:**

DNA was attached to gold nanoparticles using thiol-metal interactions as shown in Figure 22. Citrate capped gold nanoparticles were purchased (Nanocomposix) at a concentration of 0.05 mg/ml. Concentrated sodium dodecyl sulfate (SDS) was added to 10 ml of gold nanoparticle solution to bring the concentration of SDS in solution to 0.01% and the suspension was concentrated to 1.0 mg/ml before adding 25 nM of activated thiol-functionalized DNA (A = 5'- CCA ATC CAA TTT TTT TTT TTT TTT T/3ThioMC3-D/ -3'; A' = ATT GGA TTG GTT TTT TTT TTT TTT T/3ThioMC3-D/ -3'; purchased from IDT) in 10 mM phosphate buffer (Sigma-Aldrich). The thiol-functionalized DNA had been previously activated by incubating the DNA in 100  $\mu$ M dithiothreitol (DTT) and purified using size elution chromatography (Illustra NAP-25, GE Lifesciences), equilibrated with phosphate buffer and eluted. After 15 minutes, a certain amount of concentrated solution NaCl (2.0 M) was added in steps to increase the NaCl concentration in the dispersion (0.05 M for the first two steps,

then 0.1 M steps subsequently) at 20 minute intervals to bring the final salt concentration of the solution to 0.5-1.0 M.<sup>41</sup> After incubating overnight, the DNA functionalized gold nanoparticle suspension was then washed three times with phosphate buffer. All chemicals were from Sigma Aldrich unless otherwise noted.

#### **fd-Virus functionalization:**

DNA was covalently linked to the gp8 major-coat proteins of the fd-virus capsoid using a slightly modified protocol developed by Unwin et al.<sup>28</sup> A concentrated fd-virus stock solution was diluted into 10mM 4-(2-hydroxyethyl)-1-piperazineethanesulfonic acid buffer (HEPES, Sigma- Aldrich) at pH 7.0 to make 0.5 ml of fd-virus solution at a concentration of 0.25 mg/ml. To this solution, 0.5 mg of sulfosuccinimidyl-4-(N-maleimidomethyl) cyclohexane-1-carboxylate (sulfo-SMCC, Pierce) was added and mixed thoroughly. The mixture was then left to sit at room temperature for 1 hour to functionalize the fd-virus with thiol-reactive maleimide groups. Then, the fd-virus/SMCC solution was twice washed using desalting columns (40 kDa MWCO Zebra, Thermo Scientific) to remove residual reactants.

Meanwhile, 20 nM of thiolated DNA was suspended in 100  $\mu$ l of phosphate buffer and activated in 100  $\mu$ l of 100 mM DTT and left to react for one hour. The activated thiolated DNA was purified using size elution chromatography (Illustra NAP-25, GE Lifesciences), equilibrated with phosphate buffer and eluted.

To the DNA solution, 0.25 ml of the activated fd-virus solution was added and the salt concentration was increased to 200 mM using 2.0 M NaCl phosphate buffer (Sigma-Aldrich). The mixture was left to sit at room temperature for 2 hours and then dialyzed (100 kDa MWCO Spectrum Labs Float-A-Lyzer) against 10 mM Tris-EDTA buffer solution (TE, Sigma-Aldrich) in a refrigerator overnight. The resulting dialyzed sample was then collected and stored at 4°C for later use. Due to changes in volume incurred by the desalting process the volume of DNA-functionalized fd-virus solution was 1.02 ml with an fd-virus molarity of 3.74 nM.

#### **Silica nanoparticle functionalization:**

*Sulfo-SMCC chemistry:* 100nm silica nanoparticles were purchased with an aminated surface (Nanocompsix). Unlike the gold nanoparticles, the silica nanoparticles came in an acidic, acetate solution (pH= 5.5) to charge stabilize the nanoparticles below their isoelectric point (pH= 7-8). The zeta-potential values as a function of pH were provided by the vendor using a

titration measurement. Throughout the coating process it was critical to have good colloidal stability while maintaining a pH range suitable (pH= 7-9) for the two-step conjugation chemistry. The acidic buffer was replaced with an 80:20 ethanol to phosphate buffer (pH= 7.4) mixture, which provided sufficient colloidal stability for the reaction and in which of sulfo-SMCC is soluble. 2 mg of silica colloids dispersed in 1 ml were then reacted with 2 mg sulfo-SMCC. After the reaction, the colloids had sufficient stability in 10 mM phosphate buffer for the subsequent reaction with thiolated-DNA (50 nM, same sequence used for gold nanoparticles) activated using 100 mM DTT and purified using size elution chromatography. The solution was then salted step-wise 0.5 M NaCl to following the gold nanoparticle functionalization protocol.

*Carbodiimide chemistry:* Nominally 100 nm carboxyl functionalized silica nanoparticles (Micromod) were suspended in an aqueous buffer solutions of either 10 mM PB (pH= 7.4) or 100mM 2-(N-morpholino)ethanesulfonic acid (MES, pH= 5.0 or pH= 6.0, Sigma Aldrich). The nanoparticle suspension (2.5 mg/500  $\mu$ l) was then sonicated for 15 minutes. After sonication, 50 nM DNA (A = 5'-/5AmMC6/TTT TTT TTT TTT TTT GGT GCT GCG/ -3'; A' = 5'-/5AmMC6/TTT TTT TTT TTT TTT CGC AGC ACC/ -3'; purchased from IDT), 12.5 mg Sulfo-NHS (N- hydroxysulfosuccinimide, ThermoFisher Scientific) in 250  $\mu$ l of buffer and 12.5 mg EDC (1-Ethyl-3-(3-dimethylaminopropyl)carbodiimide, Pierce) in 250  $\mu$ l of buffer were added to the nanoparticle suspension and vortexed. The nanoparticle suspensions were then placed on rollers overnight. The PEG functionalized nanoparticles were then washed by centrifugation three times in PB to remove excess reagent.

*Two-step PEG/click-chemistry:* Nominally 30 nm diameter silica colloids with a partially aminated surface (Micromod) were suspended in 10 mM phosphate buffer (PB, pH=7.4) at a concentration of 2.5 mg/ml and sonicated for 15 minutes. 1 mg of the heterobifunctional PEG reagent with a Tetrafluorophenyl (TFP) ester on one end of the PEG chain with 24 repeat units and an azide group at the other (TFP-PEG<sub>24</sub>-Azide, Quanta Biodesign, Figure 41) in 10  $\mu$ l of anhydrous DMSO (dimethyl sulfoxide) was then added per ml of the colloidal suspension and allowed to react overnight. The PEG functionalized nanoparticles were then washed by centrifugation three times in PB to remove excess reagent. The PEG reaction also was performed in 10 mM aqueous buffers of 2-(N-morpholino)ethanesulfonic acid (MES, pH=6.0)

and carbonate (pH= 9.0 and pH= 10.0) buffers as well as anhydrous DMSO with and without adding 5% triethylamine (TEA).

The PEG-NP dispersions were then reacted with 50 nM of ssDNA sequences, either A or A', per 2.5 mg of NP. Both sequences consist of an alkyne group at the 5' end followed by a 15T spacer and a 7 base-pair long binding motif (A = /5Hexynyl/ TTT TTT TTT TTT TTT TTT GGT GCT G - 3'; A' = /5Hexynyl/ TTT TTT TTT TTT TTT TTT CAG CAC C - 3'; purchased from IDT). The melt temperature of the binding motif is  $T_m = 28^\circ\text{C}$  (10mM PB and 100mM NaCl). Copper sulfate (0.1mM) and sodium acetate (5mM) were used to catalyse the reaction. After 30 minutes, a concentrated buffer solution with 2.0 M sodium chloride was added to increase the salt concentration of the suspension to 150 mM and the reaction was left to proceed overnight. The DNA-NPs were then washed three times in PB to remove any unbound DNA from the solution. All chemicals were from Sigma Aldrich unless otherwise noted.

### **Silicon nanoparticles**

Silicon nanoparticles (SiNP) were functionalized using a hydrosilylation reaction. Nominally 30 nm, hydrogen-terminated silicon nanoparticles were purchased (Meliorum technologies) dispersed hexadecane (10 mg/ml) in an argon environment. In a typical experiment, silicon nanoparticle solutions were mixed in a 1:9 volume ratio with tetrahydrofuran (THF) in a glass vial and sonicated for 30 minutes before subsequently reacting with substrates containing either alkene or alkyne functionalities in quartz glassware under UV irradiation (high-pressure mercury lamp, 125 W).

#### *Hydrosilylation reaction between the silicon nanoparticles and 4-aminophenylpropargylether:*

2 ml of the silicon nanoparticle solution was mixed with 10 ml of THF and sonicated for 30 minutes. 2.2 ml of the SiNP/THF solution was added to 11.1 mg of 4-aminophenylpropargylether (aniline, Figure 64) in 38 ml of THF and UV irradiated (35 min). A control solution was also prepared by mixing 10.7 mg of the aniline in 38 ml of THF. Both solutions were washed by centrifugation with THF and pentane to removed residual aniline and hexadecane and dried under nitrogen.

#### *Hydrosilylation reaction between the silicon nanoparticles and modified carbon nanotubes:*

2 ml of the silicon nanoparticle solution was mixed with 18 ml of THF and sonicated for 30 minutes. In another glass vial, 2 mg of the aniline modified carbon nanotubes in 10 ml of DCM

was sonicated for 30 minutes. 4.5 ml of the SiNP/THF and 4.5 ml modified-MWCNT were mixed and UV irradiated (4 hours). A control solution was also prepared without UV irradiation. Both solutions were washed by centrifugation with pentane to removed residual hexadecane and dried under nitrogen.

*Hydrosilylation reaction between the silicon nanoparticles and polyethylene methacrylate:* 2 ml of the silicon nanoparticle solution was mixed with 18 ml of THF and sonicated. 9.5 ml of the SiNP/THF solution was mixed with 0.5 ml of polyethylene methacrylate (2 kDa, PM, dried under vacuum for 2.5 hours, Sigma Aldrich) and irradiated with UV light (18 hours). 8.5 ml of the nanoparticle/THF solution was used as a control. Both solutions were washed by centrifugation with THF and pentane to removed residual PM and hexadecane and dried under nitrogen.

### **Diazonium modification of carbon nanotubes**

106.2 mg of multi-walled carbon nanotubes (MW-CNT) were mixed with 206.8 mg of 4-aminophenylpropargylether in 60 ml of dry dimethylformamide (DMF) and sonicated for 60 minutes in a nitrogen atmosphere. Isopentyl nitrite (0.1 ml) was then added to initiated the reaction and the mixture was heated at 80 °C for 25.5 hours. After the reaction, the solution was dialyzed against a 7:1 ethanol to water solution to remove excess reagents. The dialyzed dispersion was then dried under nitrogen.

### **2.1.3 Dynamic Light Scattering and Electrophoresis**

Modern dynamic light scattering (DLS) instruments provide a simple, powerful tool for measuring both the size and zeta-potential of dispersed colloids by measuring their diffusivity and electrophoretic mobility. A DLS instrument consists of a laser light source and a detector that measures the scattering pattern of a sample at a given angle. The diffusivity of the colloids can be related to the autocorrelation function which compares the scattering intensity ( $I$ ) as a function of time,  $t$ , after a time ( $\tau$ ):

$$g^2(\tau) = \frac{\langle I(t) I(t+\tau) \rangle}{\langle I(t) \rangle^2}. \quad (8)$$

At short  $\tau$ , the scattering pattern will be strongly correlated, since the colloids will not have sufficient time to diffuse from their original position. In stable, dilute dispersion of

monodisperse colloids, as  $\tau$  increases, the scattering pattern will decorrelate exponentially. The rate of the decay of the autocorrelation function can be used to calculate the diffusivity of the colloids, which can then be related to the average apparent hydrodynamic radius of a colloidal dispersion through the Stokes-Einstein relation:

$$D = \frac{k_B T}{\gamma} = \frac{k_B T}{6\pi\eta r_h}, \quad (9)$$

where  $k_B$  is the Boltzmann constant,  $\gamma$  is the friction coefficient,  $\eta$  is the viscosity of the fluid and  $r_h$  is the hydrodynamic radius of the medium.

The zeta-potential ( $\zeta$ ) of a colloidal suspension is obtained through a relation to the electrophoretic mobility of the colloids by measuring their velocity ( $v$ ) in an AC electric field ( $E$ ). For colloids with a small Debye length compared to their colloidal diameter ( $\kappa a \gg 1$ ), Smoluchowski<sup>71</sup> derived an expression for the electrophoretic mobility:

$$\mu_e = \frac{v}{E} = \frac{\epsilon_r \epsilon_0 \zeta}{\eta}, \quad (10)$$

where  $\epsilon_r$  is the dielectric constant of the colloid and  $\epsilon_0$  is the permittivity of free space. The velocity of the colloids is obtained by extracting both the frequency and phase information from the Doppler shift between two interfering laser beams due to the colloidal motion in the applied electric field. The DLS and zeta-potential instruments used here were either a Malvern Zetasizer model Z or ZS.

#### 2.1.4 Fluorescent Assays

Fluorescent assays are an effective and widely used approach to quantifying the density of ligands grafted to nanoparticle surfaces<sup>41, 72</sup> and were used to measure the effectiveness of surface functionalization procedures. In a typical assay, a fluorescently tagged species first is reacted with the nanoparticle ligand. In the case of DNA assays, the fluorescent tag contains a ssDNA sequence that is complementary to the target. The nanoparticles are then sedimented under centrifugation and the fluorescence of the supernatant is then measured (Varian, Cary Eclipse) and compared to the fluorescence of a series of standard solutions with known concentrations (Figure 9).

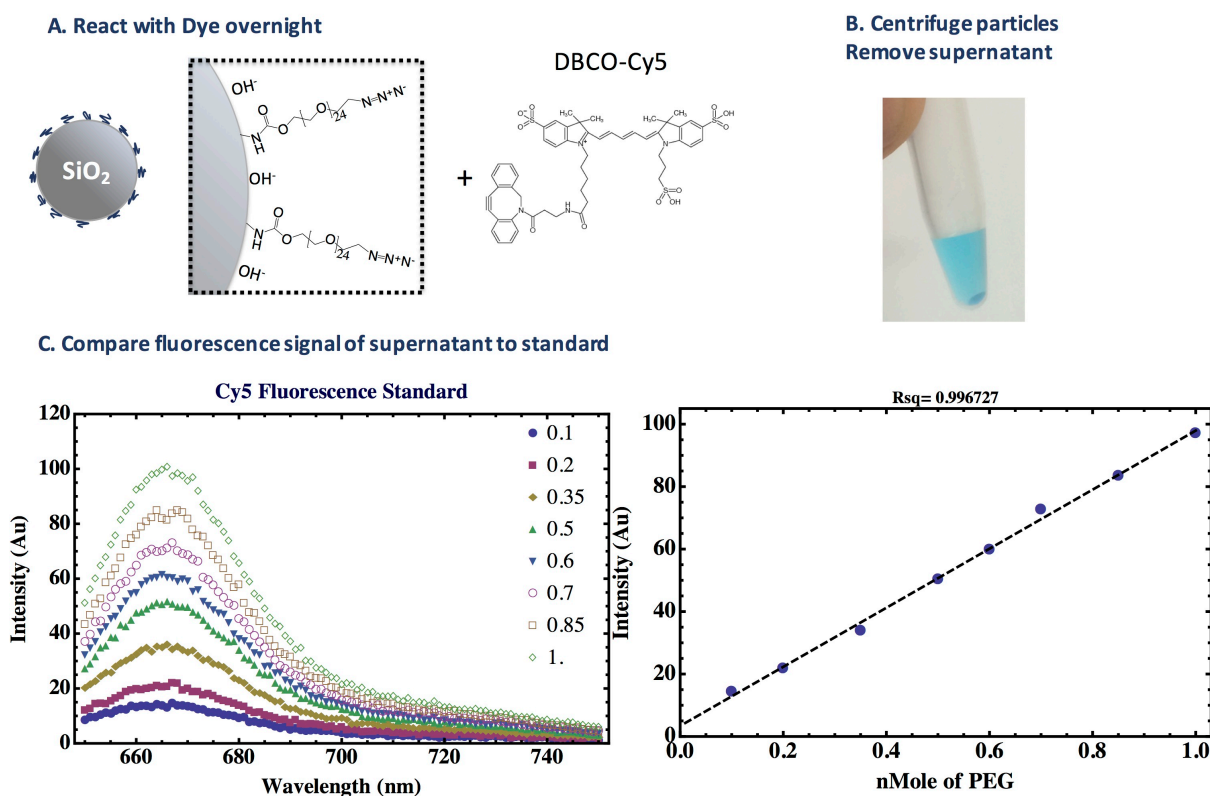


Figure 9: Diagram describing the fluorescence assay used to measuring the density of ligands grafted to nanoparticle surfaces. First, the fluorescent dye is reacted with the nanoparticle ligand (a). Next the suspension is centrifuged to sediment the nanoparticles (b). Finally, the fluorescence of the supernatant, containing the non-reacted reagent, is measured and compared to a concentration standard (c).

As described in sections 2.1.2 and 4.1, a two-step functionalization strategy was developed where nanoparticles first were functionalized with a hetero-functional PEG oligomer with a free azide group. To quantify the surface density of PEG on the nanoparticle, a dye with a dibenzocyclooctyne group (DBCO, Jena Biosciences, Dibenzylcyclooctyne-Sulfo-Cy5) was reacted with the azide functionality of PEG-NPs for 24 hours. The PEG-NPs were then sedimented from solution using centrifugation and the supernatant was compared to a standard to determine the dye concentration in solution subtracted from the total dye concentration used and divided by the number of particles in solution to give the number of PEG ligands per particle.

A similar strategy was used to quantify the amount of DNA on each nanoparticle. Fluorescently tagged DNA complementary to DNA bound to the nanoparticles was added the DNA-functionalized nanoparticles in a 0.5 M NaCl and allow to sit overnight to allow for DNA hybridization. The nanoparticles were then sedimented under centrifugation and the

concentration of the DNA in the supernatant was subtracted from the total amount added to the nanoparticle solution by comparing to a standard.

### 2.1.5 UV-VIS and FTIR spectroscopy

Ultraviolet-visible (UV-VIS) spectroscopy can be used to measure both the absorbed and scattered light of nanoparticle dispersions. The UV-VIS absorption spectrum of a sample is due to its electronic band structure making it a very useful method of characterization. The absorption of nanoparticle dispersion was measured in a quartz cuvettes with a Teflon caps in a transmission configuration (Varian, Cary 300 Bio). A cartoon of the measurement set-up for UV-VIS measurements is shown in Figure 10. UV-VIS spectroscopy was used to measure the absorption properties of both DNA free in solution and grafted to nanoparticles. When measuring nanoparticle dispersions in transmission, scattering also can contribute

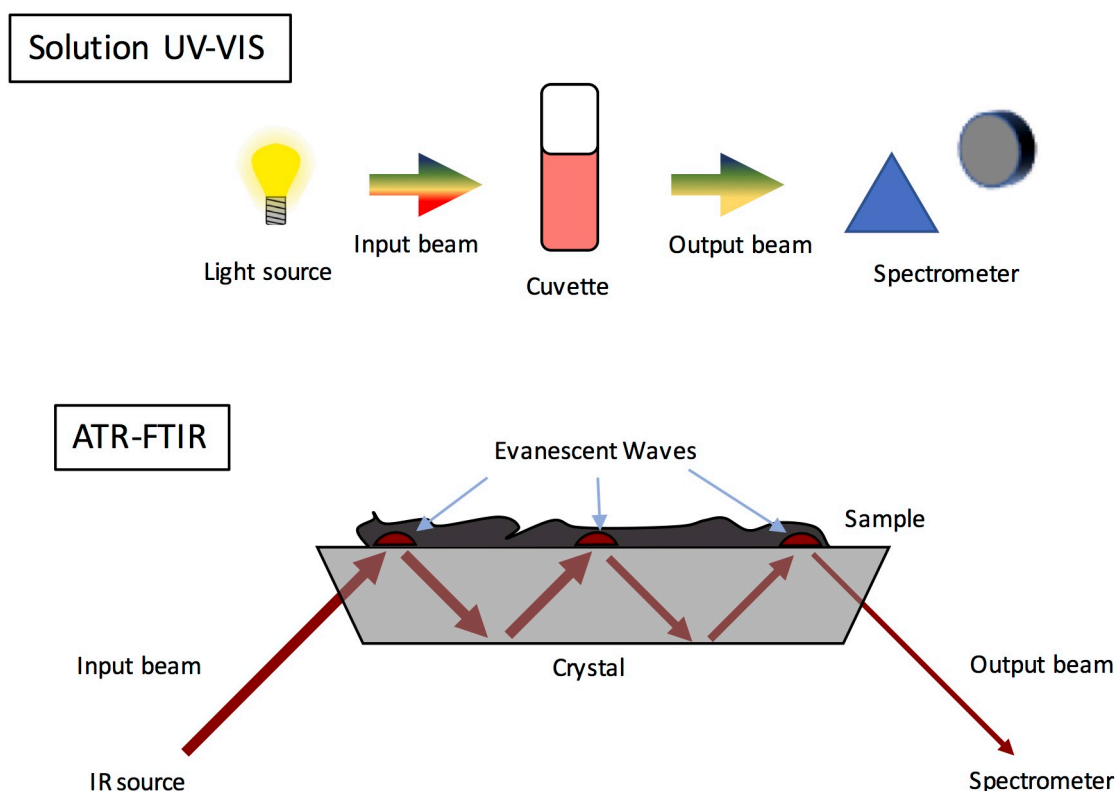


Figure 10: Cartoon of solution UV-VIS spectroscopy (top) and ATR-FTIR (bottom). In solution UV-VIS spectroscopy, light passes through a liquid cuvette and the spectrum of the absorbed and scattered light is measured by a spectrometer. In ATR-FTIR, a crystal is used to couple the IR source to the sample. The spatial overlap of the evanescent wave and the sample leads to attenuation of the input IR beam.

significantly and must also be considered. A temperature controlled UV-VIS spectrometer was used to measure the hybridization of DNA both in solution and attached to nanoparticles.

Attenuated total reflectance Fourier transform infrared spectroscopy (ATR-FTIR) is a convenient method for characterizing the infrared absorption properties of material. Solid materials such as powders are placed on a crystal with a high index of refraction that acts as a waveguide. A portion of the IR beam extends outside of the crystal. The evanescent beam spatially overlaps with the sample material allowing the vibrational spectrum of the sample material to be measured. Both Bruker and Agilent ATR-FTIR instruments were used.

## 2.2 Gel Imaging and Characterization

### 2.2.1 DNA-nanoparticle melt temperature measurements

Melt curve measurements are a powerful tool for understanding DNA hybridization and can be generated by plotting a samples absorption as a function of temperature. The relative amount of ssDNA to dsDNA can be measured through the 37% higher extinction coefficient of ssDNA than that of dsDNA at 260 nm.<sup>37</sup> A melt temperature can be defined at the absorption versus temperature point half-way in between the asymptotic values for the minimum (at low temperatures) and maximum (at high temperatures) absorption of the sample. In binary systems, such as those with two sets of DNA with complementary binding

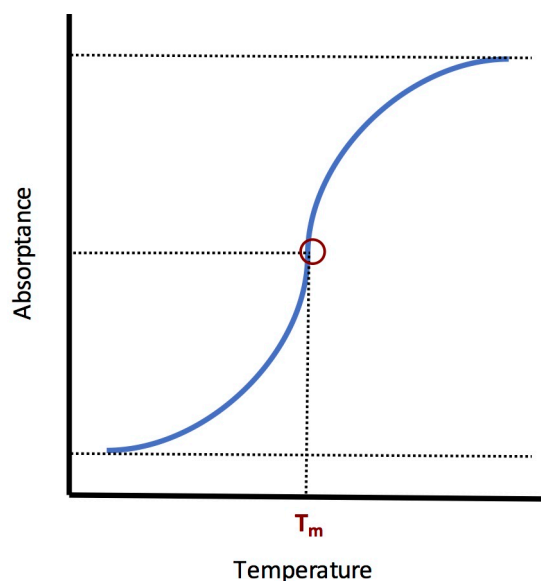


Figure 11: Diagram of a melt curve. The melt temperature ( $T_m$ ) is taken as the point half-way symmetrically between the maximum and minimum of the asymptotic absorption values.

sequences, the free-energy of hybridization can be extracted from the melt temperature measurements directly if the concentration of the DNA sequences is known and it is given by:

$$\Delta G = RT_m \ln \frac{[AA']}{[A][A']} \quad (11)$$

where  $[A]$  and  $[A']$  are the concentration of the two sequences in solution and  $T_m$  is the melt temperature. This approach is used in appendix 7.1 to measure the contribution of non-binding or “inert tails” (repeat sequences T) to the binding energy of ssDNA sequences.

In DNACC systems, melt curves do not have such a simple interpretation, since each nanoparticle can interact with adjacent nanoparticles in many configurations.<sup>40, 50, 73</sup> Therefore, the free energy of an aggregated nanoparticle will depend on numerous factors including to how many nanoparticles it is bound, the number of DNA hybridized to adjacent nanoparticles and the position of the nanoparticle:

$$\Delta G = RT_m \ln \frac{[A_1A'_1][A_2A'_2][A_3A'_3] \dots}{[A][A']} \quad (12)$$

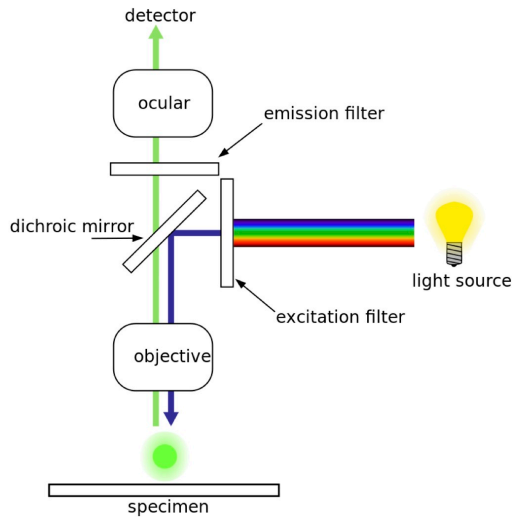
Nonetheless, melt curves can be used qualitatively to measure the effect of factors such as nanoparticle coating density, nanoparticle diameter and salt concentration on the free-energy of melting. This approach was used in section 3.2 to understand the effect of salt concentration on the aggregation of DNA coated gold nanoparticles.

## 2.2.2 Optical Microscopy

Optical microscopy is a versatile and familiar tool that has found uses across scientific disciplines. Light microscopes can be configured with a range of optical elements including light sources, lens, apertures, and filters depending on the application. Optical microscopy has been a particularly useful technique for imaging colloidal gels consisting of micron sized colloids, due to the approach’s ability to image both the constituent colloids and the gel. In this thesis, fluorescence and laser scanning confocal microscopy were used to image only nanoparticles gels, since the diameter of the colloids studied were 100 nm or less, which is below the optical diffraction limit. The resolution of optical microscopy is described by the Abbe limit of diffraction:

$$d[x, y] = \frac{\lambda}{2NA} \quad (13)$$

## Epifluorescence Microscopy



## Laser Scanning Confocal Microscopy

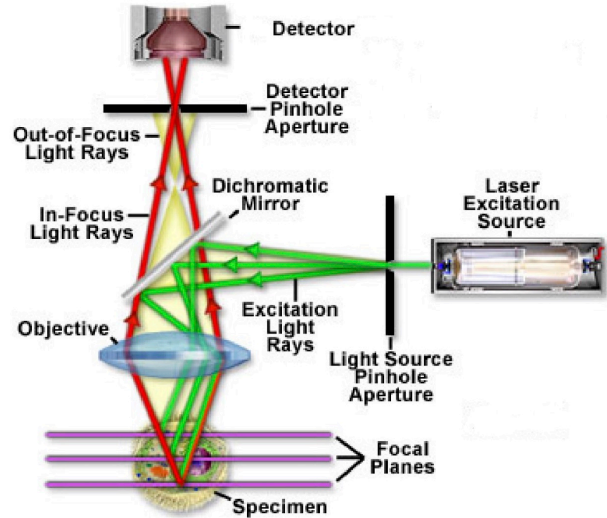


Figure 12: Diagrams depicting epifluorescence and laser scanning confocal microscopy. Diagrams taken from Nikon MicroscopyU website, <https://www.microscopyu.com>.

$$d[z] = \frac{2\lambda}{NA^2} \quad (14)$$

Even when using a high numerical aperture oil-immersion objective ( $NA = 1.4$ ), the resolution of a light microscope is limited to approximately 200 nm in the  $x$ - $y$  plane and approximately 500 nm in the  $z$ -direction. More recently, a variety of “super-resolution” techniques have been pioneered to exceed this limit,<sup>74</sup> but involve significantly more complicated experimental approaches and were not available for this work.

In fluorescence microscopy, a narrow band light source is used to excite a fluorophore which then emits photons at a lower energy. A filter block consisting of a dichromatic mirror and spectral filters then separates the incident photons from the emitted photons, such that fluorescently labeled elements appear bright at the detector or camera and the unlabeled elements appear dark. Colloidal gels samples were labelled in two ways. For transparent samples, such as silica, the colloids themselves were fluorescently labeled during synthesis. Conversely, for absorbing samples, such as gold, the background was fluorescently labeled, such that the gold colloids appear dark against a bright fluorescent background.

Laser scanning confocal microscopy is a powerful technique that is useful for 3D optical imaging of transparent materials. By introducing a pinhole aperture in the beam path of emitted light, out of focus light can be filtered out, which can greatly decrease noise in the  $z$ -direction. The  $x$ - $y$  image is formed by scanning a laser beam across the sample to build up

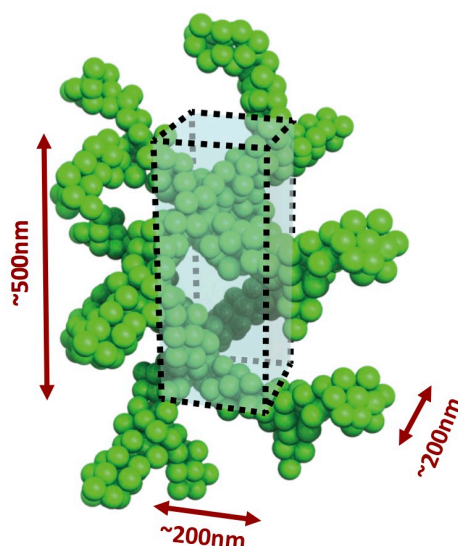


Figure 13: Cartoon representation of an imaging volume for a confocal pixel of a nanoparticle gel consisting of 30 nm diameter colloids. Yang Lan generated the three-dimensional image using Maya.

an image. By moving the sample in z-direction, images can be collected sequentially at individual focal planes. Three-dimensional images then are produced by stacking two-dimensional images together to form “z-stacks” of images, where each image represents one plane with a thickness controlled by the diameter of the pinhole and the diffraction limit of light.

Although confocal microscopy is a power tool, its usefulness is limited to characterizing the gels on the microscale, since the individual colloids often had diameters an order of magnitude less than the linear dimensions of the diffraction limited imaging volume. In the case of 30 nm diameter colloids, approximately 897 colloids can fit inside of a 200 nm X 200 nm X 500 nm confocal pixel volume, assuming random close packing of 63.4% (Figure 13).<sup>75</sup> The intensity of a confocal pixel will be proportional to the number of colloids inside of the pixel. Therefore, the confocal microscopy images are a representation of the microstructure of the gel and alternative techniques were used to examine the nanostructure of the gel.

To study the dynamics of gelation, temperature dependent “in-situ” microscopy was performed. In this configuration, the sample was mounted on a home-built Peltier stage, which allowed for precise control of the sample temperature within fractions of a degree. However, only air objectives with lower numerical apertures (NA= 0.7) could be used with the Peltier stage. Immersion objectives were not suitable for heated samples, since they would act as a heat sink, leading to uncertainty the sample temperature. In addition, heating

immersion objectives can potentially damage the adhesives that hold together the expensive lens assemblies.

### 2.2.3 Image Analysis Techniques

To characterize the length-scales in the gel micrographs, two complementary image analysis techniques were used: structure factor and chord analysis. Custom Mathematica scripts were written to implement both analysis techniques on sets of gel images. The structure factor was calculated by taking the radial average of the two-dimensional Fourier transform of the image intensity ( $I$ ) to obtain the structure factor of the both the gel and the constituent colloids. This quantity is then divided by the structure factor of only the colloids (form factor), which is calculated from the image intensity of a low volume, fraction sample ( $\phi = 2\%$ ) in the melted phase:

$$S(q) = \frac{\langle |\tilde{I}_{gel}(q_x, q_x)|^2 \rangle}{\langle |\tilde{I}_{colloid}(q_x, q_x)|^2 \rangle}. \quad (15)$$

The position of the maximum of the structure factor,  $S(q_{max})$ , indicates which wave vectors ( $q$ ) are most prevalent in the system. The relative intensity of  $S(q_{max})$  will indicate how prevalent the wave-vector,  $q_{max}$ , is compared to other wave-vectors. These wave vectors can be converted to real-space values using the relation:

$$a_r = \frac{2\pi}{q_{max}}. \quad (16)$$

This relation was useful for comparing the structure factor analysis to the real-space technique of chord analysis approach developed by Levitz, summarized in Figure 14.<sup>76-78</sup> First, the raw confocal images are processed using a common technique called a Gaussian blur to remove noise from the image. In a Gaussian blur, each pixel undergoes an averaging with adjacent pixels. Since the pixel size of the confocal images is usually less than diffraction limit, the Gaussian blur was chosen such that the pixels are blurred to the diffraction limit. Next, the image pixels are thresholded and binarized using a built-in Mathematica function based on Otsu cluster variance method.<sup>79</sup> Once the image is binarized, the chords are measured in the biphase image by counting the number adjacent pixels in both the  $x$  and  $y$  directions. The length of these chords is then plotted in a histogram. Finally, the chord histogram is fitted

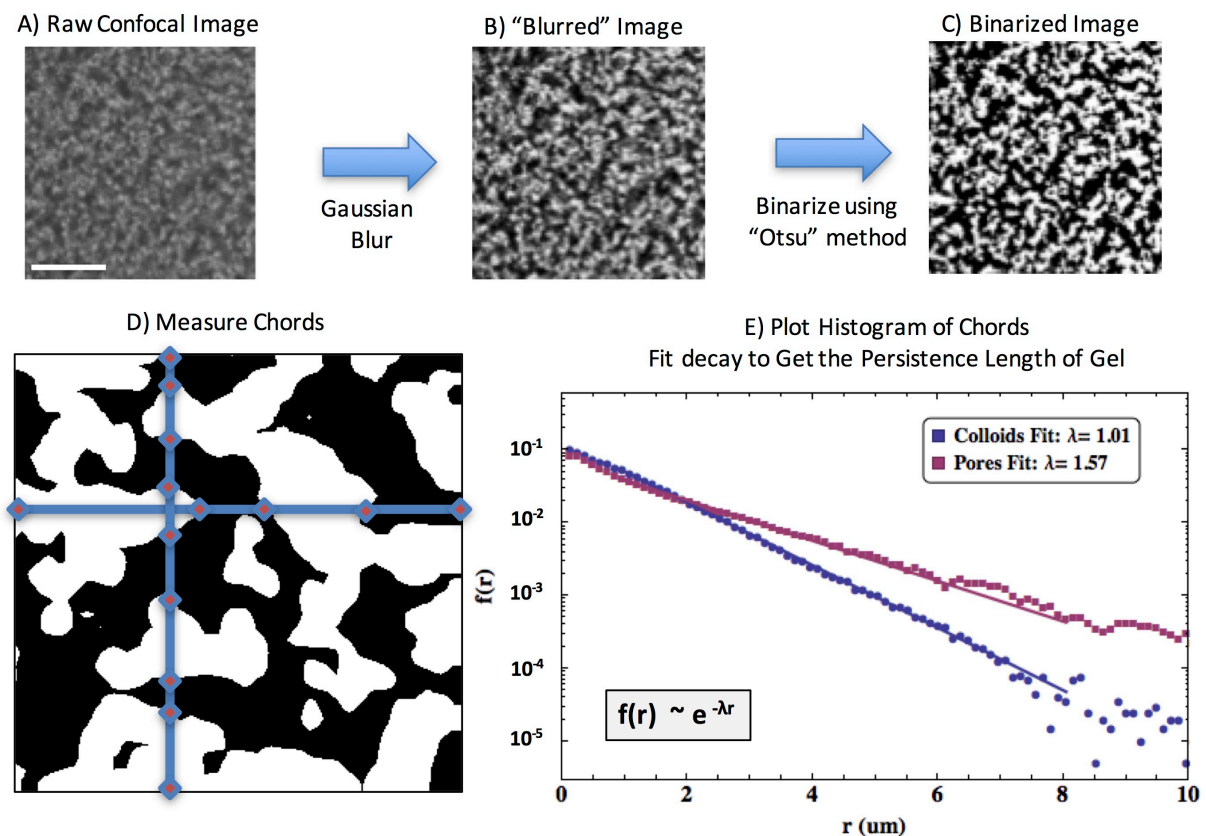


Figure 14: Chord distribution analysis methodology. (A) A “raw” microscopy image is taken using confocal microscopy. (B) The image is blurred using a Gaussian filter, such that the image pixel size is averaged to the optical diffraction limit in the  $x$ - $y$  plane. (C) The image is binarized using a built-in Mathematica function based on the “Otsu” method. (D) The lengths of the chords are measured in both the  $x$  and  $y$  dimensions for both the pores (black) and the colloid-rich (white) phases individually. (E) The histogram of the measured chord lengths in both the  $x$  and  $y$  dimensions is normalized and fitted with a  $\exp(-\lambda r)$  dependence.

with an exponential decay to find the persistence length ( $\lambda$ ) or most prevalent length-scale in the gel:

$$f(r) = e^{-\lambda r} \quad (17)$$

$\lambda$  has been shown to be a useful metric for quantifying the length-scales in many different porous systems.<sup>76-78</sup> Our group has more recently used the approach to characterize systems of polystyrene<sup>13, 52</sup> and fluorinated colloids.<sup>80</sup>

## 2.2.4 Electron Microscopy

Electron microscopy uses beams of accelerated electrons to image materials. The higher energies of electrons enable resolutions up to four orders of magnitude greater than those available using optical photons. Like in light microscopy, the electron beam can either illuminate an entire sample, as is common in transmission electron microscopy (TEM), or

raster across a sample as is common in scanning electron microscopy (SEM). Detectors can be positioned at various heights below and above a sample to collect secondary electrons emitted from a sample, electrons scattered by a sample or electrons that are transmitted through a sample.

In this thesis, three electron microscopes were used. A Hitachi S-5500 in SEM mode was used to characterizing both the size and morphology of the nanoparticles synthesized in this work. In section 3.4, DNA-gold nanoparticle gels were imaged through a nitride membrane allowing for in-situ SEM images using a FEI FEG XL30. Finally, in section 5.2, TEM and TEM tomography were used to image silicon, carbon nanotube composite material using a FEI Technai F-20.

## **2.3 Measuring Bulk Properties of Nanoparticle Gels**

### **2.3.1 Optical Spectroscopy**

In section 4.5, optical spectroscopy was used to measure quantitatively the light scattered from silica nanoparticle gels and the scattering spectrum was used to understand the underlying nanostructure structure of the gel. The reflection and transmission spectra of the samples were measured perpendicular to the capillary using a light microscope (Zeiss AX10, Figure 15). A water immersion objective (Zeiss, 40x, NA= 0.75) was used to couple light into and out of the samples. A beam-splitter allowed for light to be collected simultaneously with a color CMOS camera (IDS, UI-3580LE-C-HQ) and a spectrometer (Avantes, SensLine) through a 600  $\mu\text{m}$  optical fiber (Avantes, FC-UV600-2-SR). The input of the fiber was aligned to ensure that light was collected from the center of the sample and in the same focal plane as the camera image. The reflected spectrum was taken from several different focal planes ( $z$ ) and locations ( $x$ - $y$ ) inside of the sample and were found to be invariant with position, suggesting that the samples were isotropic on the scale of our resolution. The spectral responses of the gels were referenced to a PBS filled capillary to minimize the effect of reflections from the glass capillary and the camera's color balance was referenced to a white diffuser, certified reflectance standard (Labsphere, USRS-99-010 AS-01158-60).

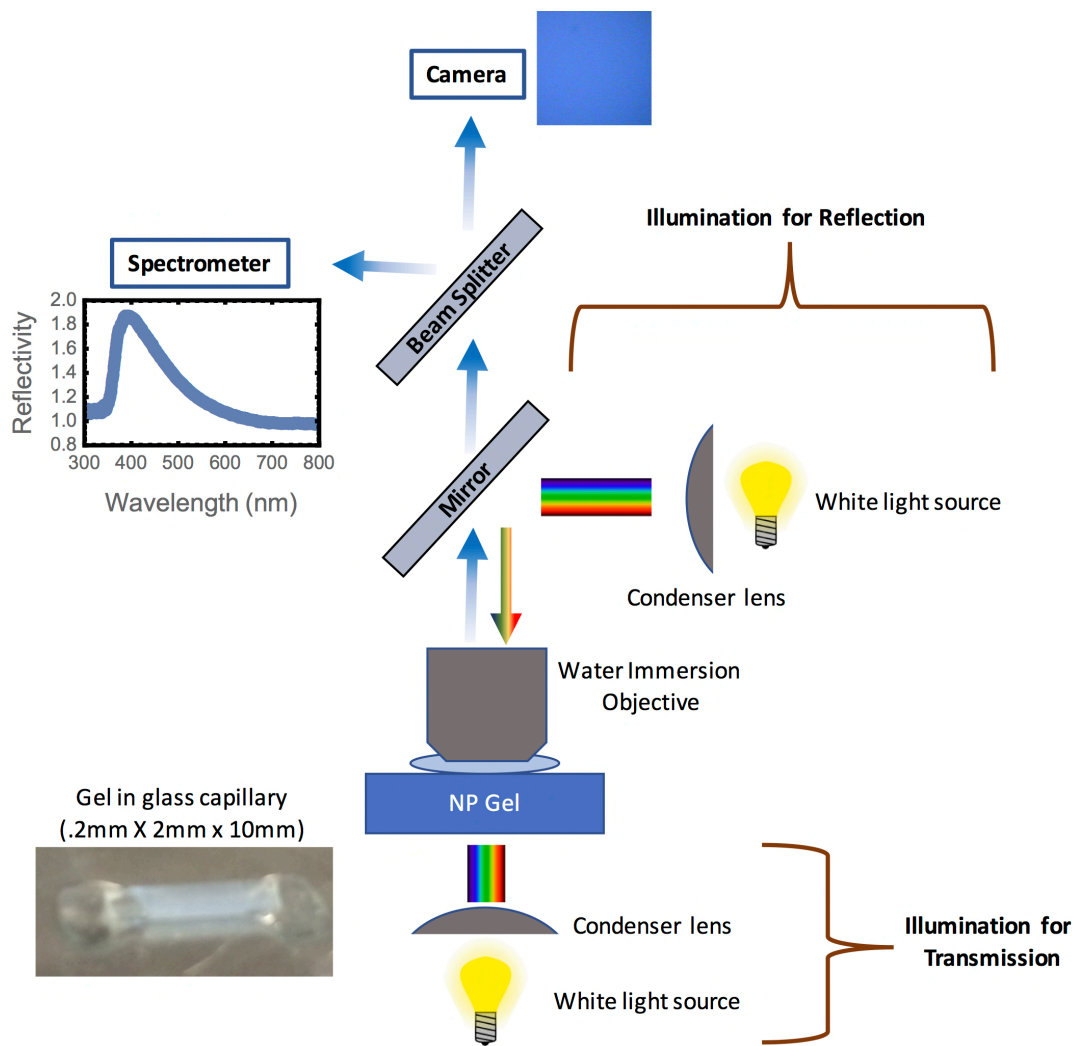


Figure 15: Optical Microscopy setup where gel samples can be illuminated either for reflection or transmission measurements. Light is collected in parallel using an optical spectrometer or a CMOS camera.

### 2.3.2 Electro-Impedance Spectroscopy

Electro-impedance spectroscopy (EIS) measures the electronic polarizability of materials and devices through the application of a small AC potential across a sample and measuring the flow of current. EIS instrumentation measures both the real (resistive or dissipative) and imaginary (capacitive or storage) contributions to a sample's current response over a wide frequency range (1 Hz to 20 MHz). Since even in simplistic systems there are multiple contributions to the impedance response, measuring over a wide frequency range allows for the separation of the individual contributions to the impedance response through a process's relaxation time. The frequency dependent response is then fitted to an equivalent circuit

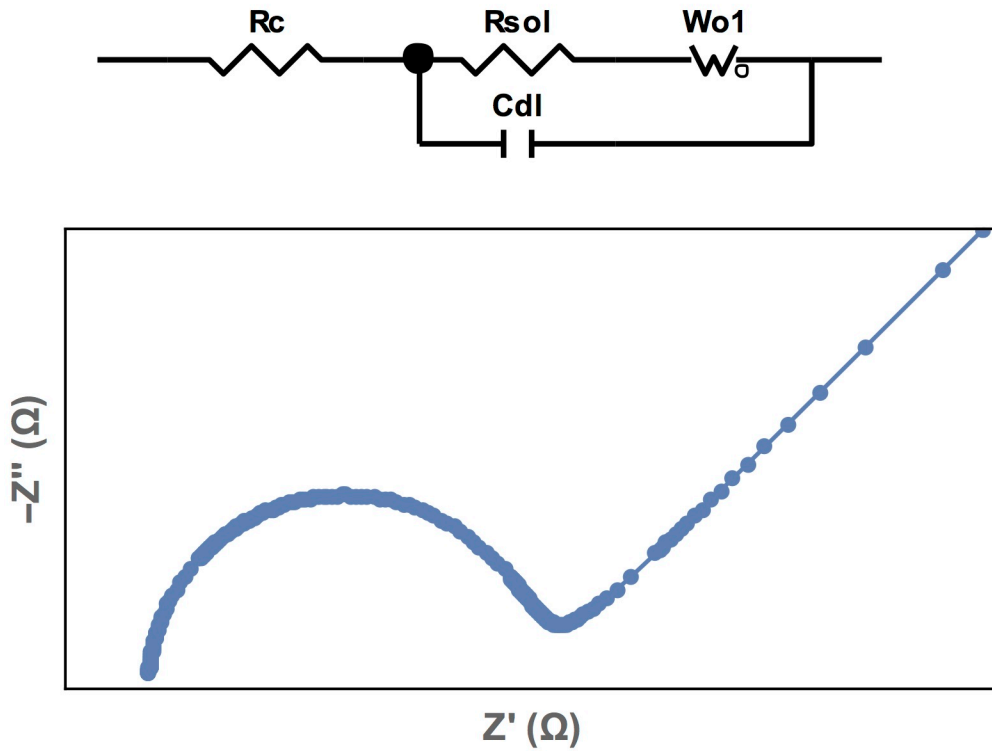


Figure 16: Example of an equivalent circuit (top) to model the impedance response of the impedance data shown in the Nyquist plot (bottom). This circuit is used later in the thesis to model the impedance response of electrolytes.

model to separate of the impedance response into the contributions from each conduction pathway in the sample to extract physical constants.

Electrical impedance is a concept that incorporates both the time dependent ( $t$ ) resistive and capacitive response of a system to a small applied voltage with an amplitude ( $V_a$ ) and a frequency ( $f$ ).

$$V(t) = V_A \sin(2\pi ft) \quad (18)$$

In the linear regime, the current response to the applied AC potential will have an amplitude ( $I_A$ ) and a phase shift ( $\theta$ ) with respect to the applied potential.

$$I(t) = I_A \sin(2\pi ft + \theta) \quad (19)$$

The impedance response of the system at a given frequency is obtained by dividing the applied voltage by the current response.

$$Z(t) = \frac{V(t)}{I(t)} \quad (20)$$

Circuit element	Impedance
Resistor	R
Capacitor	$\frac{1}{j\omega C}$
Constant Phase Element	$\frac{1}{C (j\omega)^\alpha}$
Warburg Diffusion (infinite)	$\frac{R_w}{\sqrt{j\omega}}$

Figure 17: Equivalent circuit elements for modelling impedance.

The impedance response then is separated mathematically into real and imaginary components to obtain its resistive and capacitive components. Nyquist plots, where the real and imaginary components are plotted at a given frequency, are often used as graphical representations of the impedance response (Figure 16).

An equivalent circuit model then is used to represent the different impedance contributions of a physical system by adding circuit element in series and in parallel (Figure 16). A table of the most common circuit elements can be seen in Figure 17. By fitting the parameters of the equivalent circuit elements to the experimentally collected impedance response, it is possible to extract values for the physical processes that occur in a given system. Although EIS can be used to collect a large amount of data relatively quickly, it is critical to have suitable models for fitting the data. Additional circuit elements can always be added to a model to improve its agreement with the impedance data leading to the creation of a model that may not accurately reflect the physical processes in a sample. Therefore, it is important to always correlate the impedance model to the physical processes to obtain meaningful results.

### 2.3.3 Raman Spectroscopy

Raman spectroscopy probes the coupling between the electronic and lower frequency, vibrational and rotational modes in molecules and materials. When a photon interacts with a material, only a small fraction of incident photons will be scattered inelastically, while the majority will scatter elastically (Rayleigh scattering). Due to the low efficiency of the inelastic

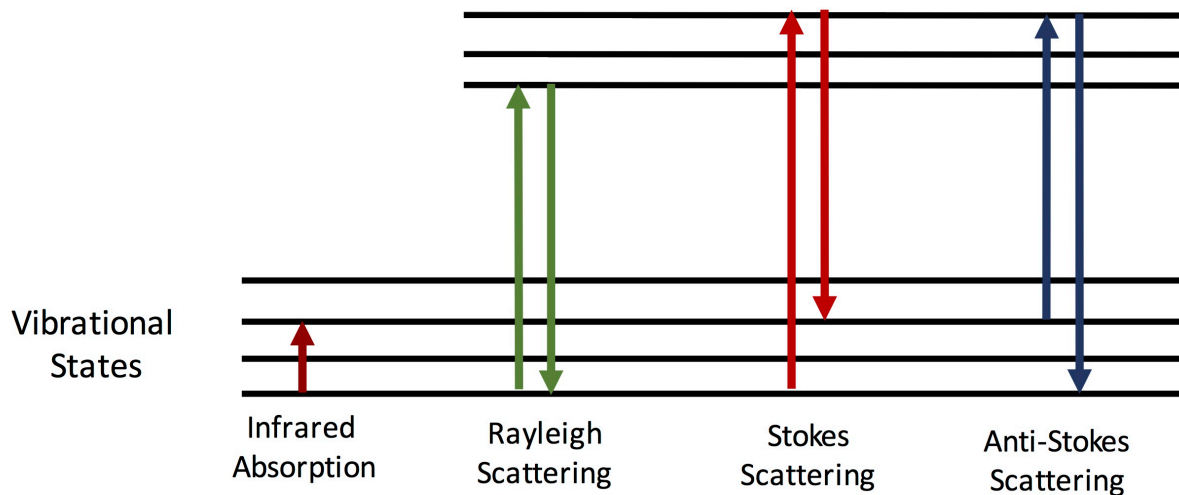


Figure 18: Cartoon depicting Raman scattering.

scattering processes, lasers must be used to obtain an appreciable Raman signal. The frequency of the inelastically scattered light can either decrease (Stokes) or increase (Anti-Stokes) with respect to the incident beam as energy is either lost or gained. In Raman spectroscopy, typically only the Stokes shift is measured, since observation of the Anti-Stokes shift requires more complex phase matching conditions. Since the low frequency modes are material specific, a Raman spectrum can be used both to characterize and identify molecules and materials in a similar manner as the infrared spectrum.

Surface-enhanced Raman spectroscopy takes advantage of the localization of optical fields to increase the coupling between electronic and lower frequency modes in materials. Raman scattering is directly proportional to the square of the induced dipole moment,

$$\vec{\mu} = \hat{\alpha} \vec{E} \quad (21)$$

where  $\hat{\alpha}$  is the chemical polarizability and  $\vec{E}$  is the incident electromagnetic field.<sup>9</sup> In SERS, the non-linear increase in Raman scattering with the incident electric field is further amplified through increasing the local electric field at a surface. The change in chemical polarizability of molecules located on surfaces also contributes to an increased Raman response, but it is typically a factor of  $10^1$ - $10^2$  rather than the  $10^4$ - $10^8$  achieved through the field enhancement.

The local field enhancement is commonly achieved through the excitation of plasmon modes in metallic nanoparticles (Figure 19). Plasmon modes are due to the collective motion of electrons in an electric field and there will be a peak in the response at a resonant frequency. The field enhancement will be localized at the nanoparticle surface with the

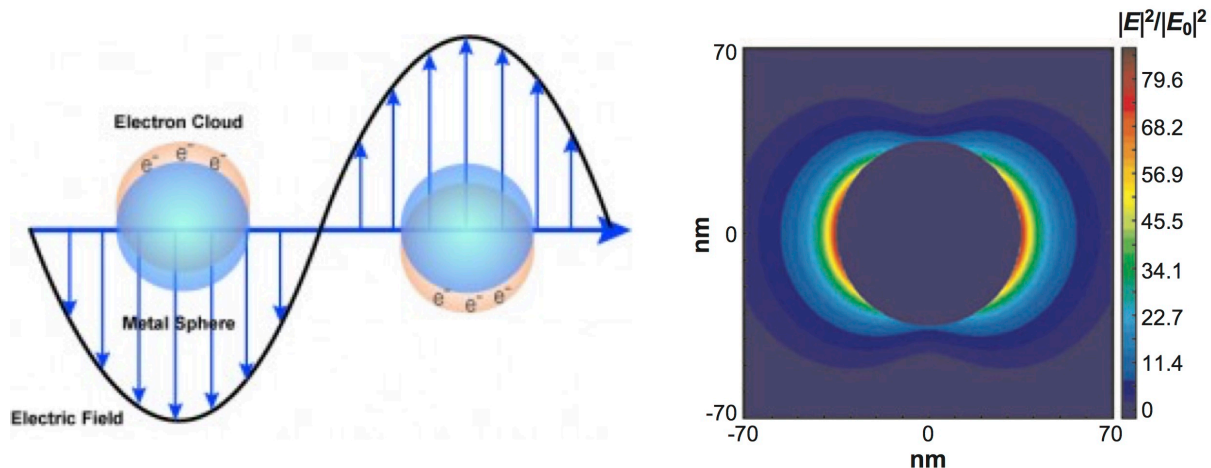


Figure 19: Cartoon showing the collective motion of free electrons in response to an electromagnetic excitation (left). Calculated electronic field intensity distribution of a spherical metal particle under electromagnetic excitation (right). Figure adapted with permission,<sup>9</sup> Copyright 2008, Annual Reviews.

intensity decreasing rapidly from the nanoparticle surface. The plasmonic resonance is responsible for the characteristic red color of isolated gold nanoparticles, which is used as an indication of colloidal gold being well-dispersed in solvents.

To achieve even greater field enhancements, nanoparticles can be incorporated into assemblies with nano-gaps between the metallic surfaces, which can be engineered to create hot spots. These hotspots can lead to an electric field enhancement of three to four orders of magnitude compared to isolated nanoparticles.<sup>81</sup> Such assemblies have enabled Raman

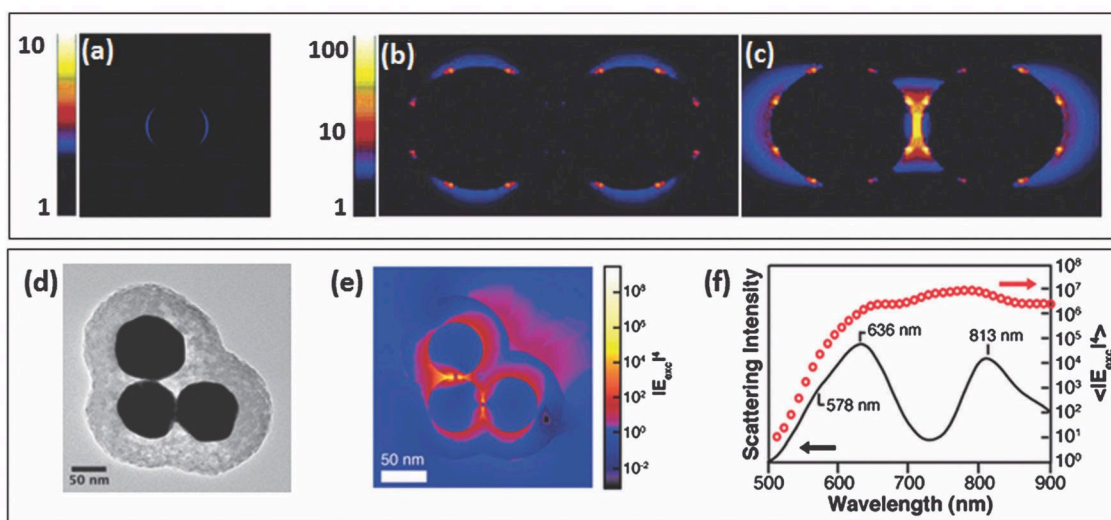


Figure 20: Calculations for the electric field enhancement of an individual metallic nanoparticle (a) and nanoparticle dimers excited in the transverse (b) and longitudinal (c) modes. TEM of gold in silica nanoparticle trimer (d) with the corresponding electric field intensity super imposed (e). The corresponding scattering intensity and calculated enhancement factor for the nanoparticle trimer (f). Figure adapted with permission,<sup>11</sup> Copyright 2012, Royal Society of Chemistry.

enhancements on the order of  $10^{10-11}$ , which is sufficient for single molecule detection.<sup>81, 82</sup>

Figure 20 shows calculations for the difference in magnitude of the electric field intensity for isolated nanoparticles and nanoparticle dimers. Such calculations are commonly made for nanoparticle assemblies using numerical methods.

Both the Raman and SERS measurements in this thesis were made using a Raman microscope (Horiba LabRAM HR Evolution). The instrument is equipped with four laser lines (485 nm, 532 nm, 633 nm and 785 nm). Gold nanoparticle samples were loaded into glass capillaries and sealed following the same protocol used for optical microscopy. The sample was illuminated with a white light source for visualization and the microscope was used to focus on the desired features in the sample.

### **2.3.4 Electrochemical measurements**

Electrochemical testing is important for both characterizing the performance of batteries and for understanding the physical properties of their components. In academic research, galvanostatic testing or the application of a constant current to a device is the most common method of testing. Typically, a constant current is applied until the cell reaches a given potential and then the direction of the current is reversed to cycle the battery. The rate of electrochemical testing is characterized by a “C” rate where C/75 rate would take 75 hours to reach the theoretical capacity of an electrode. To visualize the electrochemical data, the total applied charge or capacity ( $\text{mA h g}^{-1}$ ) over a given charge or discharge cycle commonly is plotted against the cell potential (Figure 71). In this way, electrochemical processes can be easily identified at cell potentials where there is a plateau in the charge versus potential plot. In section 5.2.4, this analytical approach is used to identify both the phase changes in battery electrodes and electrolyte decomposition (Figure 71).

To test the composite anode materials synthesized in chapter 5, solutions of anode material were “drop-cast” onto stainless steel discs by pipetting small volumes of the anode solutions onto the stainless-steel discs and letting them dry. The coated stainless steel discs were then assembled into coin cells with lithium metal cathodes to form half-cells (Figure 21). The lithium cathode and the composite anode were separated by both a borosilicate and a polymeric separator (Cellguard) to ensure that the two materials did not short circuit. A commercial electrolyte, LP30 (1.0 M lithium hexafluorophosphate in 1:1, ethylene carbonate:

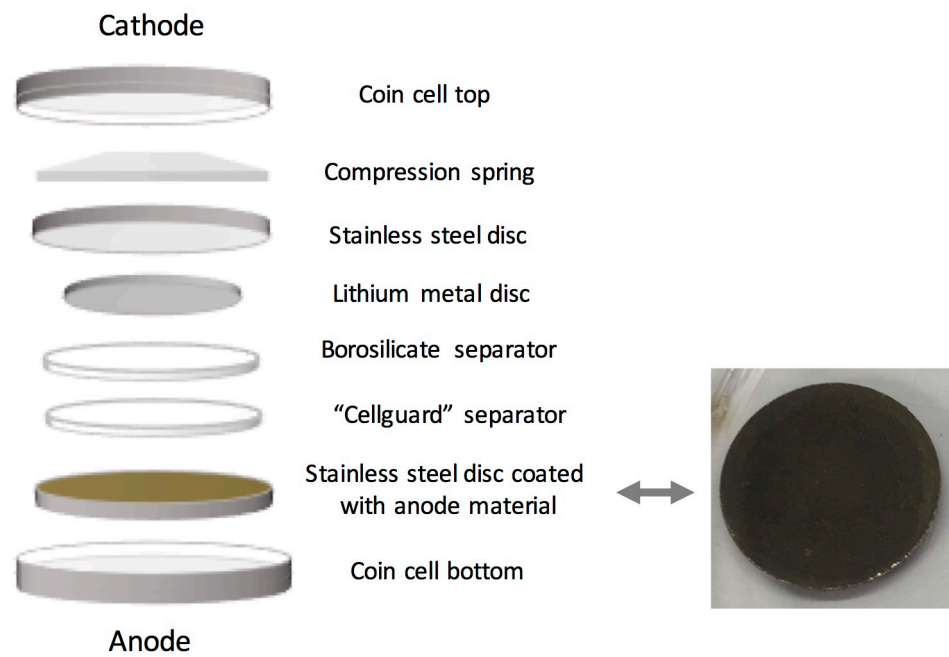


Figure 21: Diagram of coin cell assembly (left). Photograph of composite anode material "drop-cast" onto a stainless-steel disc (right).

dimethyl carbonate) was added to the coin cell to ionically couple the two electrodes. The cell components were assembled in a press that crimps the top and bottom casings of the coin cell assembly together and the compression spring ensures that all components are in good physical contact.

### **3 Gold Nanoparticle Gels**

It is now over twenty years since the functionalization of gold nanoparticles with DNA was first demonstrated.<sup>26, 27</sup> Subsequently, DNA-functionalized gold nanoparticles have been used in research as atomic analogs<sup>46, 83</sup>, biosensors<sup>84</sup>, plasmonic antennas<sup>85</sup> and SERS substrates<sup>86, 87</sup>. Although these applications span a variety of scientific disciplines, all of these demonstrations have involved the formation of discrete aggregates, spanning at maximum microns in size. Here, instead DNA-functionalized gold nanoparticles are used to form three-dimensional macroscopic objects with short-range order by taking advantage of the highly selective, tunable and thermally reversible attractions between the colloids.

To form these macroscopic gels, a protocol was developed for coating gold nanoparticles with DNA at scale. The phase transitions of the DNA-gold nanoparticles were then studied by measuring their UV-VIS absorption as a function of temperature in dilute colloidal suspensions. The temperature of the transition could be tuned through changing the interaction potentials between the colloids, agreeing with previous work.<sup>40</sup> The colloids were concentrated to form dense DNA-nanoparticle gels and the gel microstructures were studied using fluorescence microscopy.

In the second part of the chapter, the gels were characterized using techniques that take advantage of properties specific to gold nanoparticles. A new electron microscopy technique, liquid SEM, was used to image the gel nanostructure in the aqueous state. The high electron density of gold enabled sufficient contrast between the nanoparticles and the surrounding aqueous solution to resolve the individual nanoparticles in the gel. Since gold nanoparticles are chemically inert and conductive, the gels were a useful system for measuring the conductivity of DNA-nanoparticle gels. Electro-impedance spectroscopy was used to identify the conduction pathways in the gels and to test their applicability for forming porous electrodes. Finally, the plasmonic response of the gold nanoparticle gels was studied to take advantage of the plasmonic properties of gold nanoparticle aggregates and to test the suitability of the gold nanoparticle gels as substrates for surface-enhanced Raman spectroscopy.

#### **3.1 Functionalization of gold nanoparticles with DNA**

As there is now a history of functionalizing gold nanoparticles with DNA, it was possible to develop a scaled-up nanoparticle functionalization process starting from well-established

protocols. The initial protocol to coat 50 nm gold nanoparticles was based on the process developed by Mirkin<sup>26</sup> and Alivisatos<sup>30</sup> using thiol-functionalized DNA to anchor it to the surface of colloids. Gold-thiol interactions are particularly favorable for assembling oligomers onto surfaces due to both the high strength of the interaction and the mobility of the thiols across gold surfaces.<sup>38</sup>

A pair of commonly used ssDNA sequences was selected from the literature, consisting of a thiol-functionality, a non-binding spacer motif (series of thymine bases) and a binding sequence.<sup>15</sup> Since the ssDNA sequence had previously been used to functionalize 13 nm colloids, its binding sequence was shortened by three base-pairs to compensate for the higher melt temperature associated with the increased number of oligomers that can pack on colloids with larger contact areas.<sup>28</sup> This consideration led to the design of complementary 25 base-pair ssDNA sequences (15-bp spacer with a 10-bp binding motif). Due to the wide use of ssDNA in the scientific community, it was possible to purchase ssDNA already functionalized with a terminal thiol functionality, eliminating the need for further modification of the oligomer. The DNA was then used to functionalize 50 nm, citrate-stabilized gold nanoparticles also purchased commercially (Nanocomposix). 13 nm gold colloids synthesized in house as described in section 2.1.1 also were later functionalized with DNA using the same procedure.

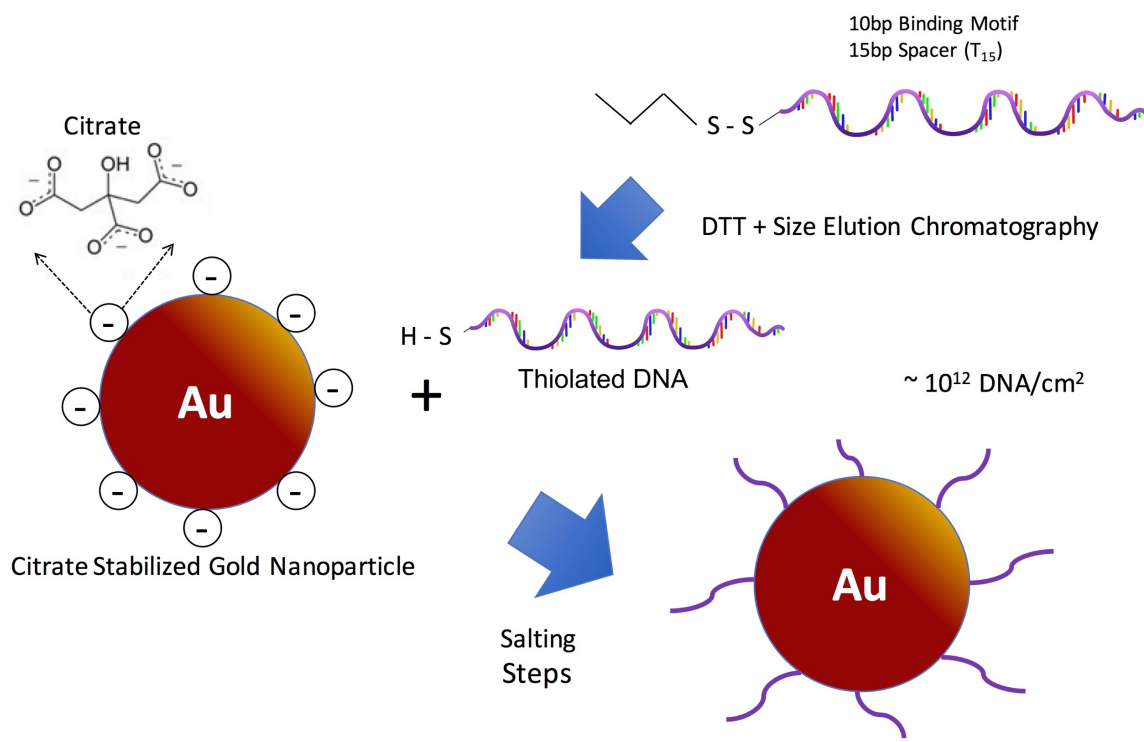


Figure 22: Cartoon of functionalizing gold nanoparticles with DNA through metal-thiol interactions.

A cartoon of the DNA coating procedure is shown in Figure 22 and is described in detail in section 2.1.2. First, to activate the thiol functionality on the DNA, the disulfide bridge is cleaved in 100  $\mu$ M dithiothreitol (DTT). The activated DNA is then separated from the alkane-thiol using differential size-chromatography. The solution of purified DNA with a free thiol is then immediately mixed with citrate-stabilized gold nanoparticles. As the DNA diffuses to the surface of the gold nanoparticles, the thiolated-DNA begins to displace the citrate molecules due to the energetically favorable metal-thiol interactions. NaCl is added to the solution in a step-wise manner (0.05 M and 0.1 M increments to 0.7 M) decreasing the Debye screening length of the nanoparticles, allowing more of the highly charged oligomers to diffuse to the nanoparticle surface. The gradual salting of the solution allows for the colloidal stability of the dispersion to be maintained above a threshold value, preventing irreversible aggregation. As more DNA attaches to the nanoparticle surface, the stability of the colloids against aggregation steadily increases due to both the electrostatic and steric properties of the oligomer.

After each salting step, the DNA-nanoparticle solution is sonicated briefly for 10 seconds, which has been shown to increase the final surface density of DNA on the gold nanoparticles.<sup>41</sup> The surface density of DNA on the gold colloids has been demonstrated to increase asymptotically with the final salt concentration of the dispersion.<sup>41</sup> After the salting is completed, the nanoparticles are washed with phosphate buffer by centrifugation to remove the excess DNA and salt from solution. The DNA-functionalized nanoparticles can be stored in dilute phosphate buffer for months or even years without aggregating.

Adapting this procedure allowed us to quickly replicate some basic experiments that demonstrated the thermally-reversible aggregation behavior of DNA-gold nanoparticles. As discussed, the previous works by Mirkin<sup>26, 42, 46</sup> and Gang<sup>44, 88, 89</sup> targeted the formation of discrete aggregates rather than macroscopic gels. Demonstrating a fully percolating gel even at small volumes ( $\sim 10$   $\mu$ l) necessitated developing a protocol for coating an order of magnitude more nanoparticles with DNA than previously reported. Due to the cost of DNA, it was not feasible simply to scale up the volume of the reaction solution while maintaining the concentration of reactants. However, calculations based on the maximum demonstrated grafting densities of DNA on a 50 nm gold nanoparticle<sup>41</sup> ( $\sim 1000$  ssDNA/NP) showed that literature procedures were already using over a hundred times excess of DNA in solution with respect to the final DNA coating density. This result suggested that it would be possible to

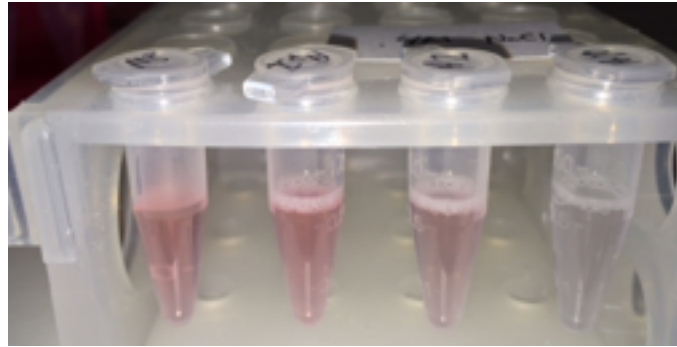


Figure 23: Gold colloids in solution with varied DNA concentrations after salting to 0.4 M NaCl. From left to right: 1x dilution, 2x dilution, 5x dilution and 10x dilution of DNA concentration (10  $\mu$ M, 5  $\mu$ M, 2  $\mu$ M and 1  $\mu$ M).

coat over 10 times more nanoparticles with the same amount of DNA, while still allowing for a large excess of DNA strands in solution using a modest quantity of DNA. As a first attempt to increase the efficiency of the literature protocol, it seemed reasonable to simply add the same amount of DNA to a larger volume of the nanoparticle solution. However, applying the protocol in these altered conditions led to colloidal aggregation, which was easily identifiable by the dark aggregates that precipitated from the suspension during the salting steps.

To understand the rate-limiting step of the functionalization process, simple experiments were performed. First, four samples were prepared with the stock concentration of 50 nm nanoparticles ( $4 \times 10^{10}$  NP/ml) with decreasing DNA concentrations varying by a factor of 10 (1x, 2x, 5x, 10x) and the same functionalization protocol was applied to each. The minimum DNA concentration (10x dilution, 1  $\mu$ Molar) still maintained a 5 times excess above the maximum binding capacity of the DNA on the gold surface. The solutions were then salted in a step-wise fashion following the previous protocol. The solutions with 5x and 10x dilutions became clearly darker during the salting process, showing nanoparticle aggregation (Figure 23). The experiment suggested that the coating process required a critical amount of DNA in solution with a 2x dilution as the critical DNA quantity for coating nanoparticles in this kinetic regime. We then hypothesized that the DNA concentration may be the critical process parameter, rather than the total amount of DNA in solution.

The next step was to see if the efficiency of the coating process could be increased by concentrating the gold nanoparticles in solution and adding the quantity of DNA used in the 2x dilution. An ionic surfactant, SDS, was added to a stock solution of citrate-stabilized gold nanoparticles and the dispersion was centrifuged until there was a clear supernatant over a dark pellet at the bottom of the centrifuge tube.

After lightly vortexing the tube, the gold solution returned to the original red color of the dispersion without any dark aggregates at the bottom of the tube, suggesting that surfactant stabilized the pelleted gold nanoparticles and prevented irreversible aggregation. The DNA functionalization process was then applied to a 15x concentration of SDS stabilized gold nanoparticles. Under these functionalization conditions, there was no sign of aggregation, suggesting that the rate limiting step of the functionalization process was between the solution and the nanoparticle surface. An alternative approach may have been to increase the reaction time in between salting-steps, which would not be desirable due to the increased time needed to perform the protocol.

The simple insight to concentrate the gold nanoparticles before the reaction, allowed for the DNA-functionalization of gold nanoparticle sufficient for the experiments described later in this chapter. The modified protocol increased the efficiency of the process, such that the cost of the gold nanoparticles now became the more expensive component for forming the composite material.

### **3.2 Thermally reversible aggregation of gold DNACC**

The collective binding of DNA strands leads to the phenomenon of a well-defined melt temperature between nanoparticle aggregates and nanoparticle dispersions. The transition temperature can be tuned by changing the concentration of salt in solution, the nanoparticle diameter, the density of DNA on the nanoparticle surface and the number of base-pairs in the binding sequence.<sup>40</sup> The melt temperature of DNA-functionalized colloids is largely independent of colloidal volume fraction, enabling the melt transition of the nanoparticles to be studied in dilute samples.<sup>8,13,80</sup> The aggregation state of the dilute colloidal solutions could be monitored optically using both the absorption of DNA and the gold nanoparticles making temperature dependent optical spectroscopy a good approach for characterizing the phase transition.

The colloidal aggregation process was followed using the relative absorption of dilute nanoparticle solutions ( $\phi = 10^{-4}$  by volume) in PBS (10 mM PB, 100 mM NaCl) at three wavelengths of interest (260 nm, 524 nm and 700 nm, Figure 24). Although the source of the signals is different for the three wavelengths, any one of them can be used to measure the relative number of nanoparticles free in solution compared to those in aggregates. At 260 nm, single-stranded DNA absorbs approximately 37% stronger than double-stranded DNA,<sup>37</sup>

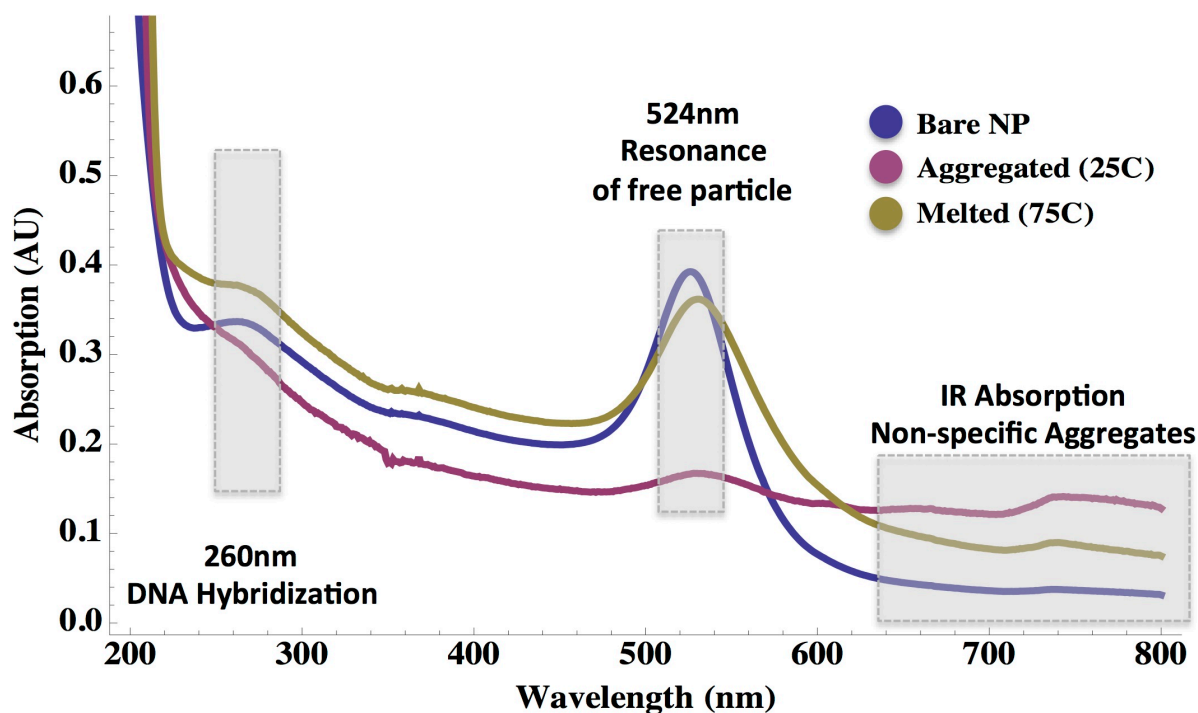


Figure 24: Absorption spectrum of the bare gold nanoparticles and coated gold nanoparticle at temperature below and above the melt temperature (60 °C) of the sample at 0.1 M NaCl concentration.

leading to a reduction in absorption in the hybridized state. The peak plasmonic absorption of isolated gold nanoparticles is at 524 nm. The absorption of the dispersed nanoparticles decreases during the melt transition at the expenses of the increased absorption throughout the near-infrared of the colloidal aggregates. 700 nm is a good measure of the broad, non-specific, red-shift in the absorption of the aggregates.

Figure 24 shows the absorption spectrum of melted and aggregated gold DNACCs as well as uncoated gold colloids. Above the melt temperature, where the gold DNACCs are isolated, there is stronger absorption at 260 nm with respect to the bare-colloids, indicating that DNA has been successfully bound to the nanoparticle surface. The UV absorption peak of bare-colloids is at a lower wavelength than 260 nm and is due to the d-band absorption of gold.<sup>90</sup> The red-shifted plasmonic resonance is attributed to the increased refractive index of the dielectric environment around the colloids due to the DNA coating,<sup>87</sup> which is further evidence of the DNA coating. The decreased signals at 260 nm and 524 nm for the sample in the melted state compared to the aggregated state is clearly visible as well as the complementary process at 700 nm.

With the optical properties of the DNACC samples now correlated to their phase, optical spectroscopy was performed as the samples were gradually heated and then cooled

to study the melt behavior (Figure 25). Samples were first heated to 85 °C for 30 minutes to homogenize the sample in the gas phase before cooling or heating slowly at 0.3 °C per minute with an absorption measurements taken every 1 °C at the wavelengths of interest. The melt curves on the top left of Figure 25 show that all three wavelengths show a continuous transition between the gas and aggregated phases reinforcing that any one wavelength is sufficient to characterize the samples. At halfway between the minimum and maximum absorption values, we can define a melt temperature of the system. This melt transition does not have the same clear physical interpretation as the melt temperature measurement for free ssDNA strands in solution, which have a clearly defined equilibrium constant of a binary equation of state. Instead, the Gibbs free energy will depend on the number and configuration of adjacent colloids each colloid is bound to in the aggregated state.

In the top right of Figure 25, there is a clear hysteresis between the cooling and heating curves. The more gradual melt transition upon cooling may be attributed to the

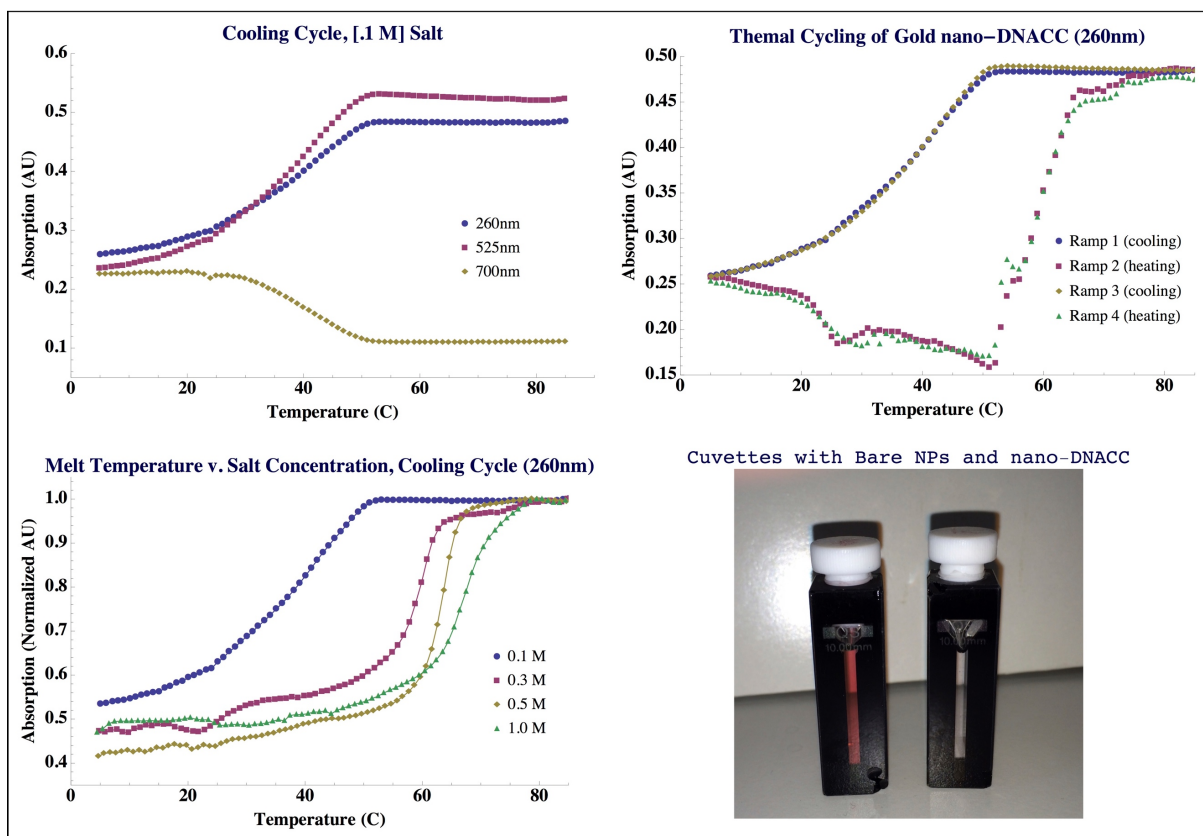


Figure 25: UV-Vis Measurements on gold nano-DNACCs. Top-left: the absorption spectrum cooling from the melt at the three wavelengths of interest. Top-right: the absorption spectrum at 260 nm of the sample during two heating and cooling cycles showing both the hysteresis and repeatability during cycling. Bottom-left: melt curves of gold nanoparticles as a function of salt concentration at 260 nm. Bottom-right: photograph of the citrate-capped (left) and DNA-coated gold nanoparticles (right) after thermal cycling. The coated nanoparticles have aggregated and have sedimented, while the citrate-capped nanoparticles remain in solution and appear red.

diffusion-limited aggregation of the nanoparticles in a dilute solution, since the colloids can be expected to aggregate upon a collision once cooled sufficiently below the melt temperature, due to the strength of DNA hybridization. The mean square displacement for colloids diffusing in solution after time,  $t$ , is given by:

$$\langle r^2(t) \rangle = 6Dt, \quad (22)$$

where  $D$  is the diffusion coefficient (equation 9).<sup>91</sup> 50 nm diameter colloids can be expected to diffuse approximately 10  $\mu\text{m}$  ( $\langle r^2(t) \rangle \approx 100 \mu\text{m}$ ) during the time step between absorption measurements (200 seconds). For comparison, the mean free path<sup>92</sup>,  $\lambda$ , of the colloids can be estimate to be approximating 50  $\mu\text{m}$  ( $\lambda \approx (n\sigma)^{-1}$ , where  $n$  is the colloid number density,  $\sigma$  is the cross-sectional area of the collision,  $\sigma = 2\pi(d)^2$ , and  $d$  is the colloid diameter). Since these two distances are the same order of magnitude, the colloid diffusivity can be expected to impact the aggregation behavior of the colloids. This effect will be become more pronounced as the gold aggregates become less diffusive due to their increased size and the number density decreases as aggregates subsequently sediment due to their reduced gravimetric height.

Upon heating the cuvette, the absorption of the solution slowly decreases until the sample undergoes a sharp melt transition just above 50 °C. The sharp onset of the melt transition upon heating more accurately reflects the melt transition of the nanoparticle gel than the cooling curve, since the colloids only need to diffuse less than a colloid diameter to dissociate, which they can easily do during the time step between measurements. Despite the geometric limitations of the measurement technique, the hysteresis is repeatable over numerous cycles, showing that the gold-thiol bond is robust under cycling and that the DNA coating is sufficient to prevent aggregation and adhesion to the cuvette walls.

The bottom left of Figure 25 shows the effect of the salt concentration on the nanoparticle aggregation process. Increasing the salt concentration decreases the Debye screening length of the nanoparticles, reducing the contribution of electrostatic repulsion to the colloidal interaction potential. In the temperature-dependent UV-VIS measurements, this effect is reflected in both a sharpening of the melt transitions and a shift to higher temperatures. Changing the salt concentration was the simplest method for demonstrating the effect of the colloidal interaction potential on the melt transition. Alternatively, changing

the length of the DNA binding sequence, the DNA surface coating density or the colloid's diameter could also have been used.

### **3.3 Formation and fluorescent microscopy of DNA-gold nanoparticle gels**

After studying the phase transitions of dilute samples of DNA-gold nanoparticles, more concentrated samples of nanoparticles were used to investigate the system in the gel state using optical microscopy. Previously, our group had formed DNA colloidal gels using larger 500 nm polystyrene particles.<sup>13, 48</sup> Making DNA-colloidal gels from 50 nm particles would mean the incorporation of building blocks an order of magnitude smaller than our previous studies enabling the formation of colloidal gels with truly nanoscale features.

Gold nanoparticles coated with complementary DNA were mixed in a 1:1 ratio (A to A') in PBS solution and centrifuged to concentrate the colloids. Concentrating the stock solutions of DNA-functionalized gold nanoparticles was difficult without a high-speed centrifuge (>20,000 G) due to electrostatic repulsion. However, dilute solutions of complementary DNA-gold nanoparticles in PBS buffer could easily be sedimented using low-speed centrifugation due to the reduced gravitational height of the aggregates. The excess supernatant could then be removed using a pipette. Once the samples were concentrated, they were transferred into a glass sample chamber in either the aggregated (room temperature) or melted (heated) state. The sample chambers used for these initial experiments were made from glass coverslips and UV-epoxy and later replaced with rectangular glass capillaries.

Dark aggregates are clearly visible in the sample loaded into the chamber at room temperature (Figure 26). The black color is indicative of the broad plasmonic absorption of the gold nanoparticles in the aggregated state. When the samples were heated, the nanoparticles repel each other and become freely dispersed in solution, causing the sample to appear a dark red color due to the plasmonic resonance of the isolated particles. When the sample is once again cooled, it appears homogeneously black throughout, as the aggregated particles are distributed uniformly throughout the sample volume.

Because the gold nanoparticles are absorbing throughout the visible and near-infrared spectrum, a small amount of fluorescent dye was added to the solution as a negative contrast agent. Fluorescein salt (Sigma Aldrich) was selected, since its peak emission (515 nm) overlaps well with the peak absorption of the isolated gold nanoparticle plasmonic resonance

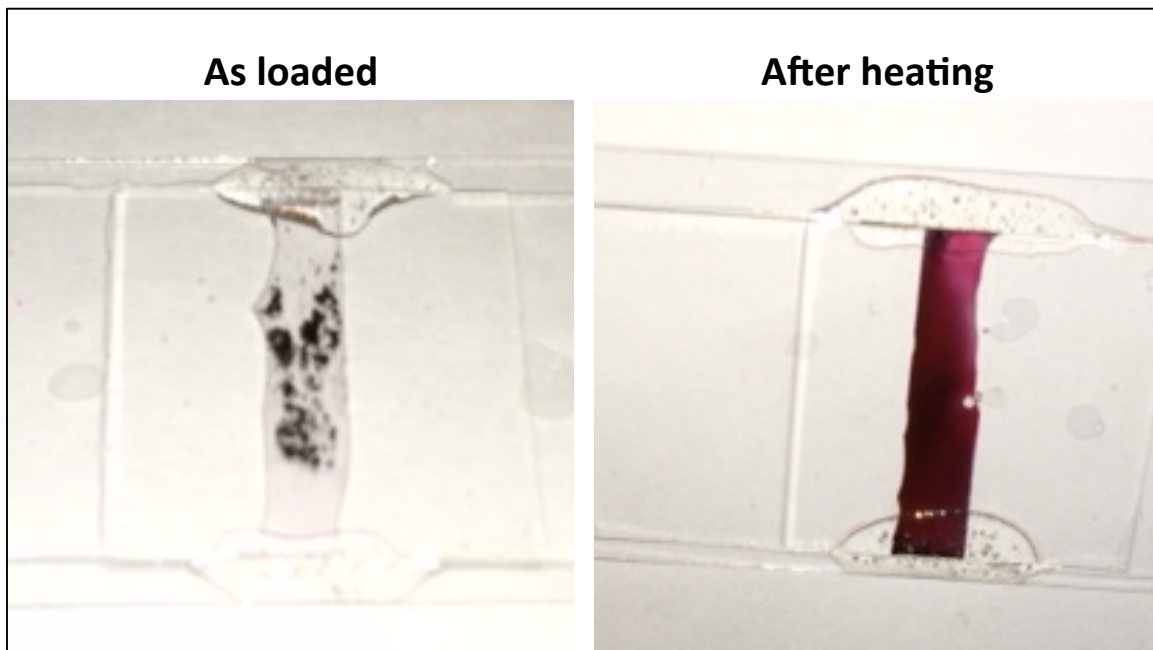


Figure 26: Gold nanoparticle sample chambers, as loaded (aggregated, left) and heated (melted, right).

and its high solubility in aqueous solvents. The sample could then be illuminated with a LED to excite the fluorescent background, allowing for negative imaging of the gold nanoparticles. A fluorescent microscope with a home-built Peltier stage was used to image the sample as a function of temperature.

When the nanoparticles are heated, they are free in solution and appear as mobile dark pixels in the camera (Figure 27). As the sample is cooled, the nanoparticles aggregate and their positions are fixed on the micron-scale. The gold aggregates sink to the bottom of the sample chamber and locally form a dense gel. As the sample is now biphasic, the gel pores appear bright due to emission from the fluorescent solution and the gel structure appears black due to the absorption of the gold colloids.

The sample was first homogenized by heating it above the systems melt temperature (60 °C) for 30 minutes allowing for the colloids to diffuse uniformly throughout sample chamber. The sample was then thermally cycled to temperatures above and below the gel melt temperature, while microscope images of the sample were collected every 1 °C. After data collection, the microscope images were then analyzed using a Mathematica script to obtain two quantitative metrics. The intensity of each pixel was averaged for each image to get an average image intensity. The average image intensity can be used in an analogous manner to the previously presented spectroscopic technique to monitor the phase of the

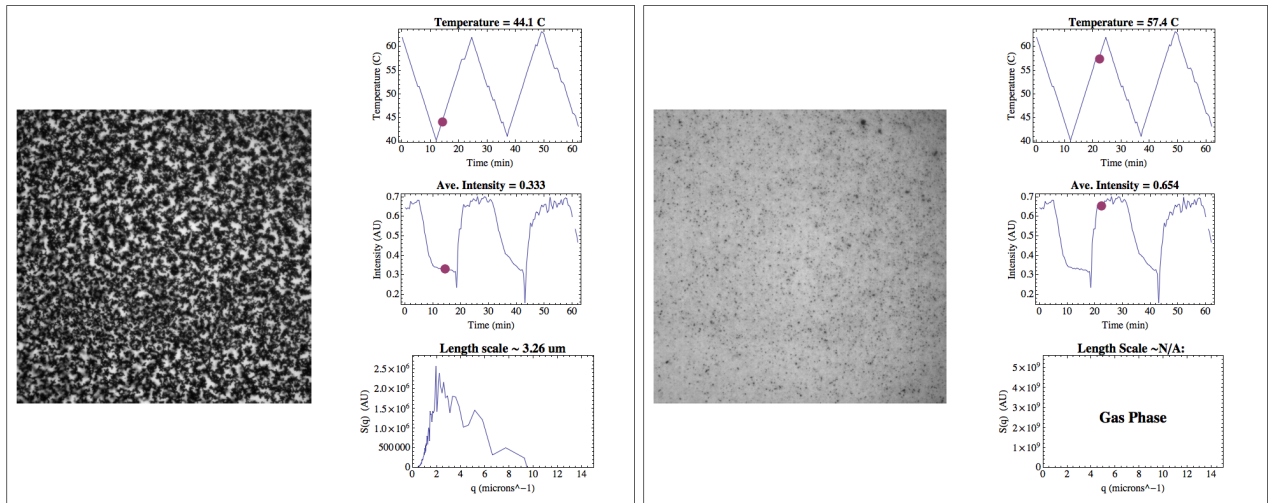


Figure 27: Frames showing the microscopy images, temperate data, image intensity and structure factor of sample of DNA-gold nanoparticle gels. Example from of sample in the gel (left) and gas (right) phases.

sample. The structure factor of the image was calculated by taking the radial distribution function of the two-dimensional Fourier-transform of the image and the peak position of the structure factor was converted to a real-space length ( $a=2\pi/q$ ). This length-scale can be used as a quantitative metric to characterize the gel’s morphology at the microscale.<sup>8, 13</sup> At each 1 °C increment, a frame was generated using a custom Mathematica script to display the microscopy image of the sample, sample temperature, average image intensity and image structure factor. These frames were then stitched together to form movies, to help study the nanoparticle gelation process. Example frames of a nanoparticle samples in the gas phase and the gel phase are shown in Figure 27. We have found that videos created by stitching together these frames are a good tool for communicating the behavior and properties of DNA-colloidal gels.

These experiments were the first example of DNA colloidal gels made from colloids with diameters that are tens of nanometers rather than hundreds of nanometers.<sup>21, 48</sup> The microstructure of these gels is studied in more detail in section 5.1, using both chord and structure factor analysis. The structure of these gold nanoparticle gels is compared to a composite material made from gold nanoparticles and high-aspect ratio cylindrical colloids. The nanostructure of the gold nanoparticle gels is imaged in situ using a SEM technique in the next section.

### 3.4 Electron microscopy of DNA-gold nanoparticle gels

Since optical microscopy is limited to imaging the nanoparticle gels above a resolution of a few hundred nanometers, a complementary technique was needed to look at the gel's nanostructure. In the absence of access to a central user X-Ray facility for small-angle X-ray scattering or X-ray tomography, electron microscopy was a natural choice. However, conventional SEM requires a high-vacuum environment, which would have necessitated imaging the gel in the dry state. Unfortunately, techniques such as super-critical drying or encapsulation<sup>93</sup> would alter the gel's nanostructure. Environmental SEM in a high-pressure environment of water vapor was considered, but it was not performed due to concerns about changing the sample volume and salt concentration during sample preparation, homogenization and imaging.

Instead, the DNA-gold gels were imaged using a relatively new technique where a small volume of the gel can be sealed into a chamber with a thin nitride window using a silicone gasket mounted on a conventional SEM holder (wetSEM, Electron Microscopy Sciences). The nitride window allows for electrons to pass through to image the nanoparticle dispersion and keeps water molecules from escaping into the high-vacuum environment of the SEM chamber. The wetSEM capsules therefore are compatible with conventional SEM instruments and can be imaged in a similar manner to dry samples.

We performed some basic experiments to understand the capabilities of the technique. A solution of 15  $\mu\text{l}$  of 50 nm, DNA-gold nanoparticles with  $\phi = 1\%$  (1:1 mixture of

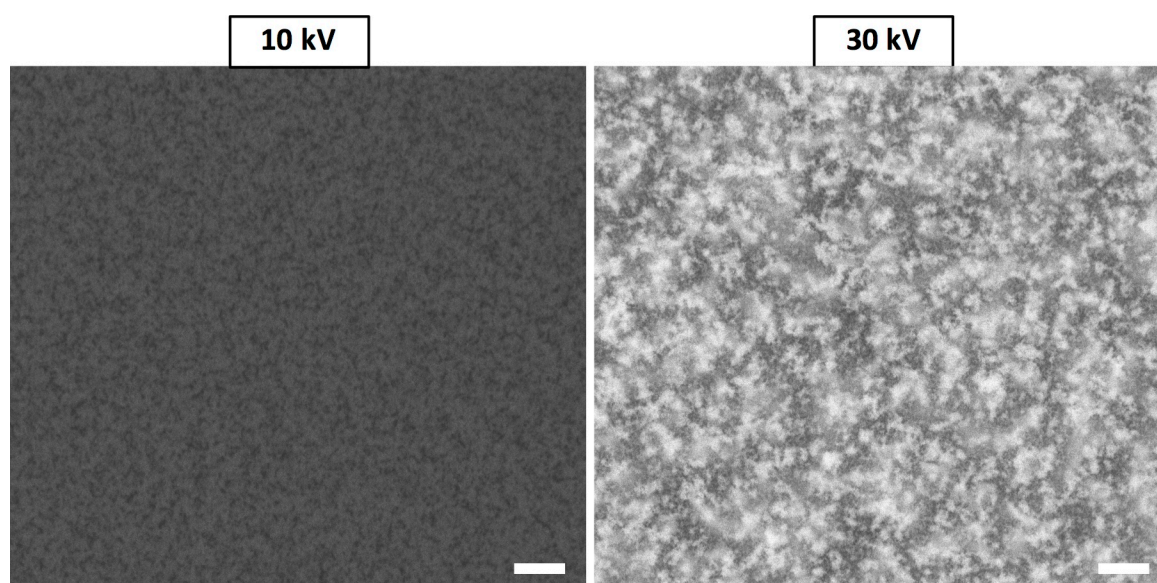


Figure 28: SEM imaging depth in wetSEM capsule as a function of acceleration voltage. The images are not normalized for intensity. The scale bar is 10  $\mu\text{m}$ .

A and A', 10mM PB, 100mM NaCl) were loaded in the SEM capsule. The capsule was then put on a heating plate 30 minutes above the gel's melt temperature (60 °C) to homogenize the sample. The power on the heating plate was then turned off and the gel was allowed to cool slowly to form a homogeneous gel. The sample was prepared with the nitride membrane facing down onto the heating plate, so that as the colloids aggregated, they would sediment onto the nitride membrane and adhere to it with sufficient force that the film could be imaged when the capsule was flipped 180 degrees in the SEM.

The gel was then observed under various conditions to understand the imaging depth, the effect of the electron beam energy on the sample and the ultimate resolution of the technique. Figure 28 shows the effect of acceleration voltage on the imaging depth. At 10kV, the image appears to contain information that spans only the first layer of colloids in the sample. However, at 30 kV, information from additional imaging planes becomes visible, creating a more three-dimensional image. Not surprisingly, the depth of imaging is less than what can be achieved for dry samples due to the absorption of electrons by water molecules.

Figure 29 shows the effect of the electron beam on the gel structure. The image was stopped during the second scan to show the effect of the electron beam on the sample. Clearly, the second scan has a very different morphology than the first scan. The energy of the electron beam is likely locally heating the sample causing the gold nanoparticles to rearrange. Further experiments with an in-situ heating of the SEM capsule could be used to examine if the rearrangement is due to irreversible aggregation or if the rearrangement can

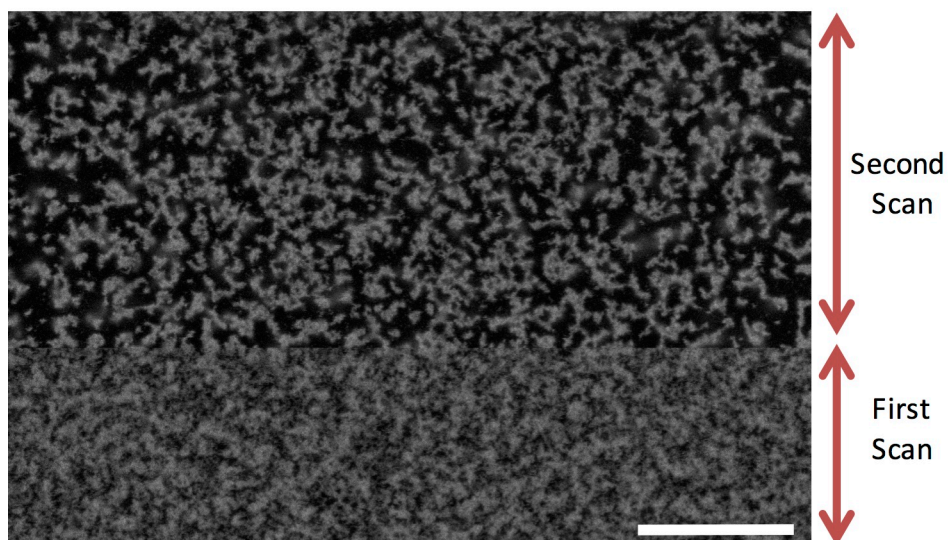


Figure 29: Effect of electron beam on sample in wetSEM capsule. The acceleration voltage is 15kV and the scale bar is 10  $\mu$ m.

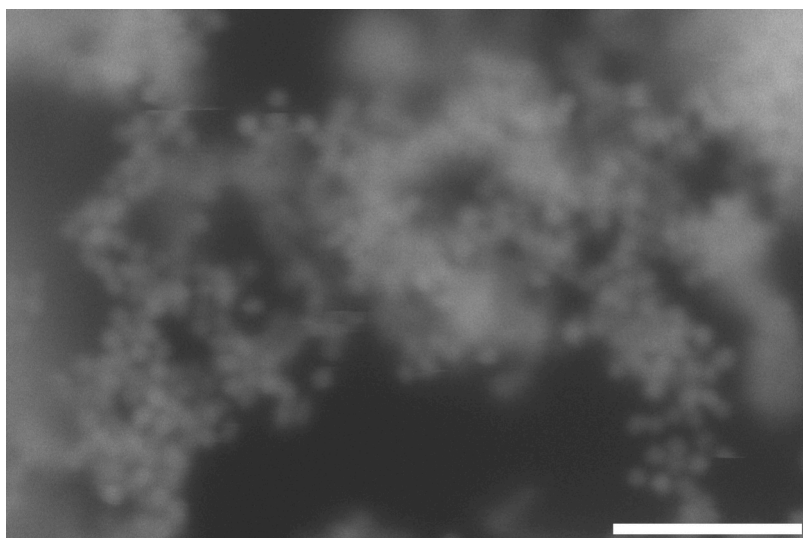


Figure 30: SEM micrograph of gold DNACC gel imaged such that single 50 nm colloids are visible. The acceleration voltage is 30 kV and the scale bar is 400nm.

be simply reversed by homogenizing the sample. The electron beam may be a good method for locally heating the gel to cause rearrangement and introduce local features to an otherwise homogeneous gel.

The ultimate resolution of the technique is important, as previously we did not have a method for imaging the individual nanoparticles in situ. Figure 30 shows a high-resolution electron micrograph of the DNA-nanoparticle gel. For the first time, it was possible to image individual gold nanoparticles rather than simply the colloid-rich gel branches. The micrograph was taken by first focusing on a portion of the gel and then moving towards another portion to ensure that there was no damage from a prior pass of the electron beam. The colloids closest to the surface can be seen with a clear gap visible between the colloids. The gap between the colloids is due to the steric barrier of the DNA. Such micrographs can be used to examine the local order of the individual colloids and the porosity of the gel. As predicted, the packing of the colloids does not appear to be locally crystalline, rather the gels form a kinetically-trapped structure. Since the gold nanoparticles are not transparent to electrons, it was only possible to examine the surface of the gel. Small angle X-ray scattering (SAXS) measurements at the Grenoble facility in December 2017 are scheduled to measure the nanostructure of the bulk of the gel.

### 3.5 Electro-impedance studies in Gold Nanoparticle Gels

Colloidal self-assembly is a promising technique for creating porous electrodes with morphological control on the nano-, micro- and macro-scales. Optimizing electrodes at these different length-scales can allow for an increase of an electrode's surface area improving the reaction kinetics of surface-limited processes, while retaining sufficient microporosity to enable diffusion of the charge carriers through the electrolyte. This optimization is particularly relevant for battery applications, where compromises are often made between power and energy densities, which are limited by electrodes' thicknesses.<sup>62</sup> DNA-gold nanoparticles are a good model system for experimentally exploring conduction in three-dimensional self-assembling electrodes, since the inter-particle spacing can be tuned using the length of the DNA sequences, the nanostructure and microstructure can be controlled by the colloid interaction potential and gold is a good conductor and is electrochemically inert.

Figure 31 shows a cartoon of a DNA-gold nanoparticle network spanning two gold contact electrodes. The inter-particle spacing between adjacent gold nanoparticles will be determined by both the length of the DNA binding sequence and the spacer. The hybridized DNA can be considered rigid as the persistence length of dsDNA is approximately 35 nm.<sup>34</sup> Here, the length of the DNA binding sequence is 10 base-pairs, which will lead to a rigid, linear structure of approximately 3.3 nm in length. On either end of the hybridized DNA are 15 base-pairs of ssDNA, which are flexible in solution as the persistence length of ssDNA is approximately 1 nm (3 base-pairs).<sup>33</sup> In good solvent conditions, the radius of gyration ( $R_g$ ) of the DNA oligomer can be calculated from the number of repeat units ( $N = \frac{15 \text{ base-pairs}}{3} = 5$ ) and the persistence length of a unit ( $a = 1 \text{ nm}$ ) and is approximately 2.6 nm.<sup>94</sup>

$$R_g = a N^{\frac{3}{5}} \quad (23)$$

However, since the DNA oligomers are attached to the gold surface at a high density, the DNA strands are stretched into in the "brush" regime. In the stretched regime, the length ( $L$ ) of a grafted oligomer can be determined from  $N$ ,  $a$  and the average distance between grafting sites ( $D = \sqrt{\frac{\text{stands}/NP}{\text{Area}}} = 2.2 \text{ nm}$ ), giving a length of approximately 4.3 nm.<sup>94, 95</sup>

$$L = \frac{Na^{\frac{5}{2}}}{D^{\frac{2}{3}}} \quad (24)$$

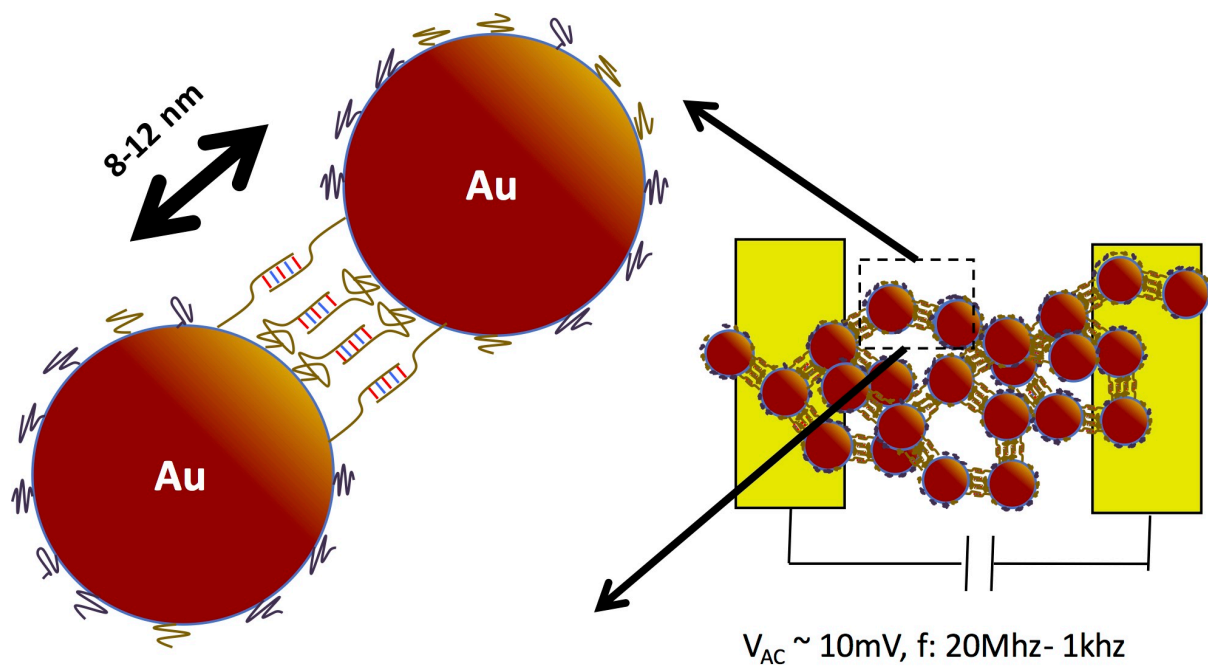


Figure 31: Cartoon of the impedance measurement on DNA-gold nanoparticle gels. Diagram showing the average distance between gold nanoparticle dimers (left). Cartoon of DNA-gold nanoparticle network spanning two electrodes with an applied AC voltage.

Simply summing up the contributions from ssDNA and the dsDNA segments gives an approximate inter-particle spacing of approximately 11 nm, but the nanoparticles are likely somewhat closer than this distance, since dsDNA and ssDNA do not necessarily have to be co-linear. Moreover, to minimize the free energy of DNA hybridization, the DNA strands will maximize the number of hybridized base-pairs and DNA strands along the colloids' surface will stretch to form more bonds reducing the spacing between colloids as shown in the cartoon in Figure 31.

Electro-impedance spectroscopy (EIS) experiments were designed to probe whether the inter-particle spacing between the gold nanoparticles was small enough to measure the conductivity of the gels. Liquid EIS cells were designed and fabricated in-house (Figure 32). Approximately, 50 nm thick gold contacts (2 mm x 6 mm) separated by 1 mm were thermally evaporated onto microscopy slides with a thin chromium adhesion layer. U-channels were machined into glass to form 25 mm long, 2 mm wide, and 0.2 mm deep inset channels. The channels were then placed upside-down on the gold contacts such that the channel spanned the contacts perpendicularly and were adhered to electrode substrates using UV-epoxy. The

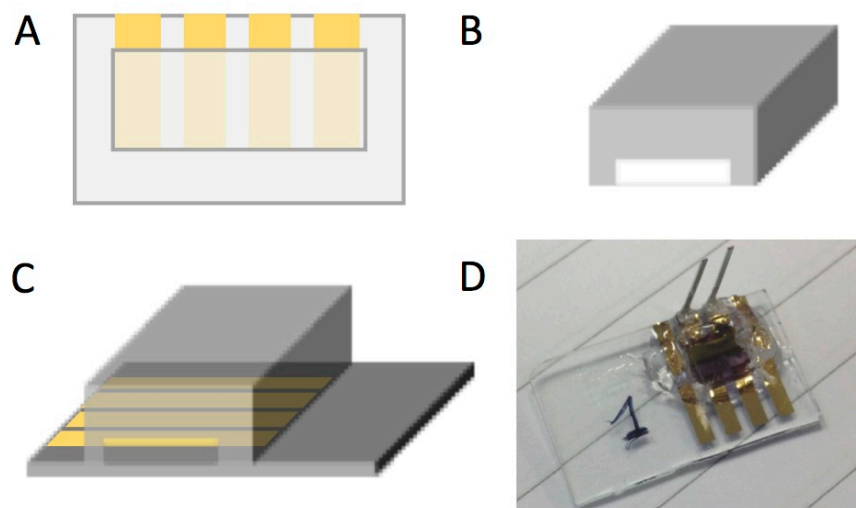


Figure 32: Diagram of the top-view of liquid impedance cell consisting of gold contacts deposited on glass substrate and a u-channel (A), machined glass U-channel (B) and assembled cell (C). A photograph of an assembled cell containing a DNA-gold nanoparticle film (D).

resultant channel had a volume of 10  $\mu\text{l}$ . Pins were soldered to the gold contacts to provide reliable electronic contact with the external circuit.

Samples of gold DNACCs at different volume fractions,  $\phi = 0.5\%$ , 1%, 2% and 5% in PBS (10mM, 0.15 M NaCl) were loaded into the liquid EIS cells and sealed with a two-part epoxy. The samples were heated above their melt temperature for 30 minutes and quenched to homogenize the gel samples. Reference samples with 0.01 M KCl and 0.15 M NaCl were also prepared. After homogenization, the gel samples appeared black due to the overlap of the plasmonic resonances of the sedimented gold nanoparticles, which formed thin films that were in close contact with the gold electrodes. An EIS cell filled with DNA-gold gel at room temperature can be seen in Figure 32.

To understand the impedance characteristics of the DNA-gold nanoparticle network, it is useful to first look at the impedance response of the EIS cells filled with the KCl and PBS reference solutions. KCl commonly is used as a reference solution, since it fully ionizes in water. The impedance of the cells filled with the salt solutions is well modeled by the Randles cell in Figure 33, consisting of a contact resistance ( $R_c$ ), a solution resistance ( $R_{sol}$ ), double-layer capacitance ( $C_{dl}$ ) and a Warburg diffusive element ( $W_o$ ). The contact resistance contains the impedance information of the wire leads, metal pins, solder and chromium-gold contacts.

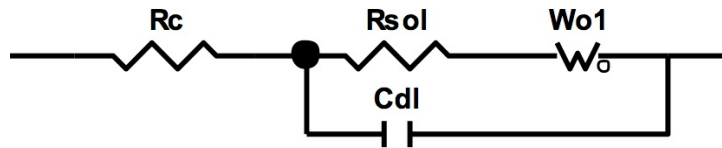


Figure 33: Randles equivalent circuit for impedance cell with salt solutions.

The double-layer capacitance comes from the Debye length of the gold contact electrode in solution and the Warburg impedance comes from the diffusion-limited transport of ions through the solution.

The impedance spectrums for the KCl and PBS solution (0.15 M NaCl) can be seen in the Nyquist plot in Figure 34. The difference in the diameter of the arcs is a graphical representation of the increased solution resistance of the KCl solution ( $R_{sol-KCl} = 2.6 \times 10^4 \Omega$ ) compared to the PBS solution ( $R_{sol-PBS} = 8.8 \times 10^2 \Omega$ ). The order of magnitude difference is expected, since the PBS solution contains approximately 15 times more ions than the KCl solution. The other clear difference between the two samples is the frequency where the right side of the arc approaches the x-axis, which is determined by the large difference between the  $C_{dl}$  of the PBS sample ( $C_{dl-PBS} = 4.1 \times 10^{-12} \Omega$ ) and the KCl sample ( $C_{dl-KCl} = 8.2 \times 10^{-13} \Omega$ ), and comes from the reduction of the thickness of the Debye layer at the electrode surface due to the higher ionic concentration of the NaCl solution. The right-side of the arc touches down at 1 MHz for the PBS sample, while the right-side of arc is at a minimum at 23 kHz for the KCl sample. It is relevant to note that most impedance spectrometers can only

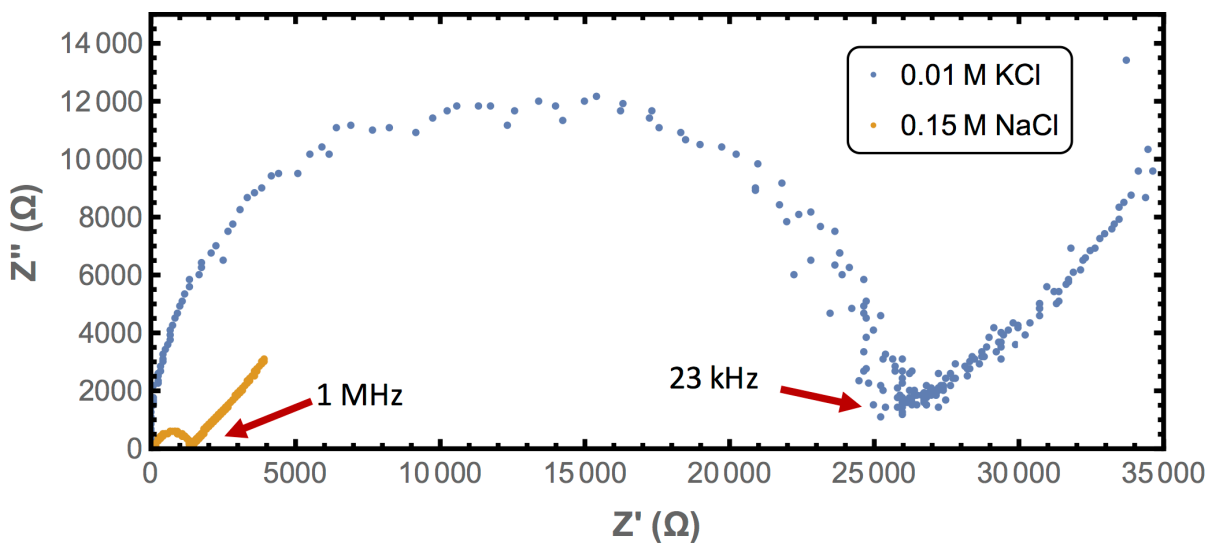


Figure 34: Nyquist plot showing impedance of KCl reference solution and NaCl-PB electrolyte. Red arrows point to the local minimum with the frequency labeled on the plot.

measure frequencies below 1 MHz, but because of the extended sensitivity of the Solatron instrument used here, it was possible to resolve  $R_c$ ,  $R_{sol}$  and  $C_{dl}$  separately. The Warburg impedance dominates the low frequency response of both salt solutions and is identifiable by the 45° angle of the response on the Nyquist plot.

The impedance responses measured using our custom-built impedance cell can be calibrated using  $R_{sol-KCl}$  to obtain the cell constant. The cell constant is an experimental factor that relates the geometry of an impedance cell to a conductivity standard. Here, the cell constant is obtained by dividing resistance of 0.01 M potassium chloride ( $R_{KCl} = 1.27 \times 10^7 \Omega \cdot \text{m}^{-1}$  at 20 °C)<sup>96</sup> by the measured solution resistance using the cell ( $k_{cell} = 490 \text{ m}^{-1}$ ).

$$k_{cell} = \frac{R_{KCl}}{R_{sol-KCl}} \quad (25)$$

The value of the cell constant is an important contributor to the sensitivity, resolution and accuracy of the measurement.

The impedance response of the PBS sample is useful for interpreting the high-frequency response of the DNA-gold gel samples (Figure 36). The frequency where the right-side of the arc approaches the x-axis remains at 1 MHz for all samples, which agrees with the expectation that the  $C_{dl}$  should be the same as for the PBS reference sample and remain constant with  $\phi$ . The radius of the arcs increases with  $\phi$ , corresponding to an increased resistance with the gel volume fraction. As this resistance is present in the PBS sample, it can be associated with the ionic conductivity of the PBS electrolyte in the gels. The increased resistance with  $\phi$  may be a result of the nanoparticles acting as a physical barrier to the motion of ions, which would be consistent with the gold nanoparticles not acting as a conductive element above 1 MHz.

The frequency response below 1 MHz gives information about the properties of the DNA-nanoparticle gel itself. The impedance response can be modeled by the equivalent circuit in Figure 35, where the response above 1 MHz is represented by a resistance,  $R_{c+sol}$ , for simplicity. The resistive properties of the DNA-nanoparticle film are represented by resistance,  $R_{NP}$ , the capacitive properties are modeled using the constant phase element,

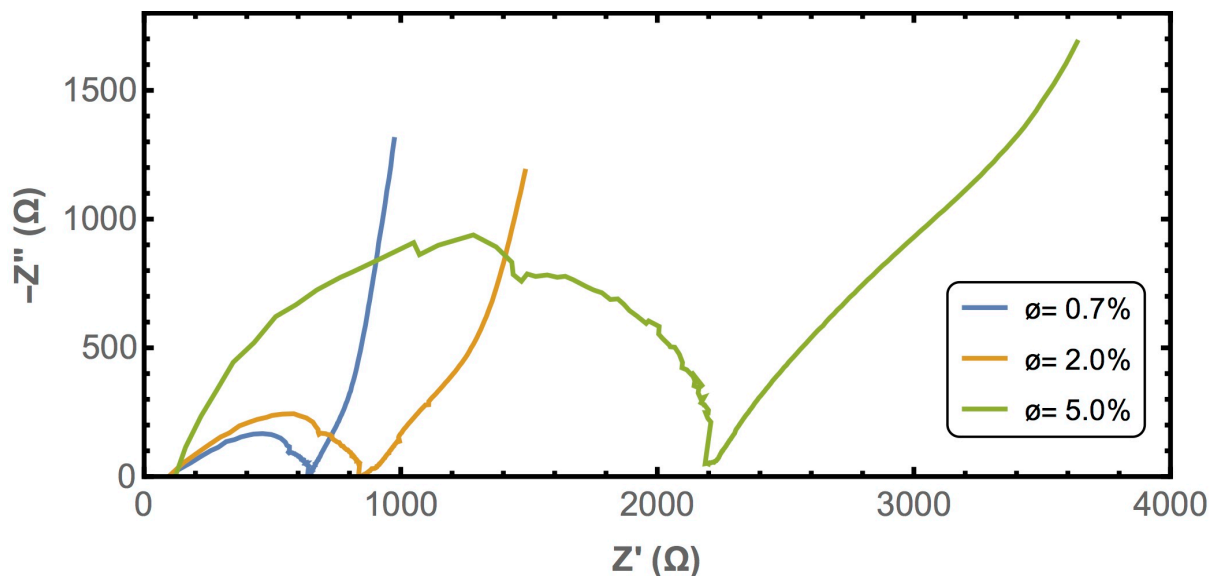


Figure 36: Nyquist plot showing impedance response of DNA-gold nanoparticle gels as a function of volume fraction in 10 mM PB and 150 mM NaCl.

$CPE_{NP}$  and the diffusive portion is again modeled using a Warburg element. Constant phase elements are commonly used to capture the non-ideal capacitive behavior of nanoparticles and porous electrode in solution. When the exponent of the  $CPE_{NP}$ ,  $CPE_{NP-P}$ , equals 1 the constant phase element behaves as an ideal capacitor, while if  $CPE_{NP-P}$  equals 0.5, it behaves as a Warburg element (section 2.3.2). As  $\phi$  increases, the resistance and capacitance of the film increases and the capacitive behavior becomes less ideal. The change in these three

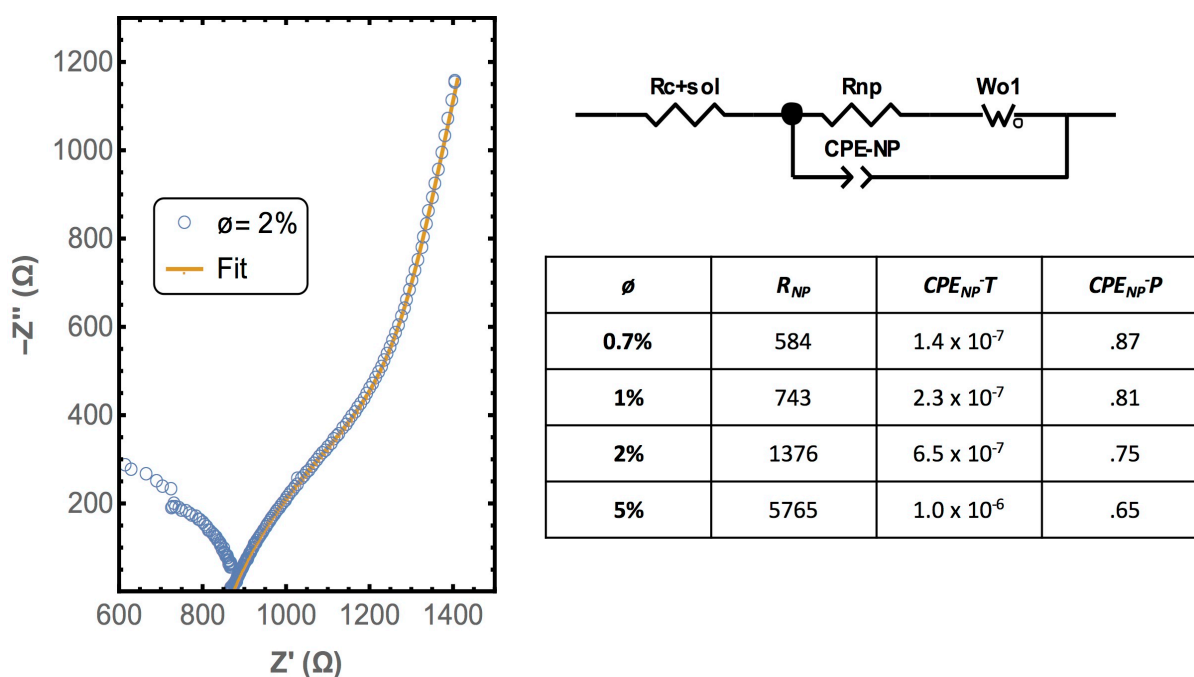


Figure 35: Randles equivalent circuit for the impedance response below 1 MHz for DNA-gold gels (top right). Impedance response for gel with  $\phi=2\%$  and a fit (left). Table summarizing the fit parameter for the Randle circuit as a function of  $\phi$ .

parameters are consistent with a thicker and denser film of nanoparticles in the conduction path with increased  $\phi$ .

The frequency dependence of the impedance of the DNA-nanoparticle film is consistent with the de Levie model for porous electrodes.<sup>97-99</sup> In porous electrodes, the frequency dependence is determined by the penetration depth of the applied AC wave. At high frequencies, the pores are small compared to the penetration depth appearing semi-infinite, leading to diffusive behavior. At low frequencies, the penetration depth becomes greater than the pore dimensions and the impedance response becomes capacitive. A similar impedance response has also been seen in electrode films made from gold and nickel particles.<sup>97</sup>

The DNA-gold nanoparticle networks were capacitive as they approached low-frequencies (direct current). Since no significant conductance was measured at low frequencies, additional efforts were not spent correlating the impedance model to the physical processes in the system. It may be possible to measure the low frequency conductance of the nanoparticle film with more sensitivity using an impedance cell with a lower cell constant. Microelectrode arrays are available commercially and may be useful for this purpose.

Reducing the inter-particle spacing by shortening the length of the DNA binding sequences and spacers could potentially increase the conductivity of the gel. However, studies on networks of gold nanoparticles separated by alkane-thiols, have shown that an inter-particle spacing above a couple of nanometers leads to a significant reduction in conductivity.<sup>39, 100, 101</sup> The conductivity in such systems is described with an electrostatic model developed by Abeles<sup>102</sup>, with a thermally-activated hopping energy that is a function of both the colloid diameter and the inter-particle spacing. The conductivity of DNA-gold nanoparticle networks in the dry state also have been found to be governed by this mechanism.<sup>103</sup> However, SAXS measurements on the dried sample showed that the distance between nanoparticle decreased such the gold colloids were “almost touching” upon drying.

Alternatively, aqueous DNA-gold nanoparticle networks also could be made more conductive by forming nanowires along the DNA linkers.<sup>104</sup> There are numerous examples of seeding DNA heterogeneously with small nanocrystals and subsequently growing the nuclei into nanowires in the literature.<sup>105, 106</sup> Similar nanowires have also been achieved by coating

DNA with conjugated polymers.<sup>107</sup> A flow cell has been designed and built to metalize the DNA bridges the nanoparticle gels and is an interesting avenue for further research.

### **3.6 SERS on Gold Nanoparticle Gels**

Colloidal assemblies of gold nanoparticles are a common substrate for surface-enhanced Raman spectroscopy (SERS).<sup>9</sup> As discussed in section 2.3.3, the nano-gaps between the gold colloids create a local electronic field enhancement or hot spots, which can be used to drastically increase the sensitivity of Raman spectroscopy. Most of the current SERS literature using nanoparticle assemblies as substrates has focused on obtaining sharp plasmonic resonances through tight control over inter-particle spacing. However for SERS, it is not necessary for the peak spectral resonance of the hot-spot to be positioned precisely at the wavelength of the incident laser and it has also been shown that the near-field plasmonic modes may differ significantly from the far-field modes.<sup>108</sup>

To obtain tight control over the inter-particle spacing, colloids typically are arranged using techniques designed to form discrete assemblies, such using DNA-origami.<sup>87, 109</sup> Although such assemblies can be engineered to have highly controlled distances between nanoparticles, these assemblies are typically hundreds of nanometers or at best a few microns in size, which is comparably small to even a highly collimated, focused laser beam. Therefore, much of the incident electric field will not overlap spatially with the colloidal assembly and will not contribute to the sample's Raman response. Moreover, there is the additional challenge of sorting, selecting and exciting such small objects, increasing the difficulty in making simple and repeatable Raman measurements.

DNA-gold nanoparticle gels are fundamentally macro-sized objects. An excitation laser beam easily can be focused onto a colloidal gel without the need for locating a specific sample volume containing the active element. The entire focused beam will spatially overlap with the colloidal gel and contribute to the Raman signal. Although the nano-gaps will vary throughout the gel, the inter-particle distance will be defined by the DNA oligomers consisting of both rigid and flexible components. The gel will contain an ensemble of inter-particle distances, rather than a tight distribution. The broader distribution of nano-gaps also can be advantageous, since the gel will also support more near-field electronic modes, albeit with lower peak intensities. Even a Raman instrument with a micro-spot size will be large enough

to excite many local resonant environments, such that they all will contribute to the Raman signal.

To test the feasibility of using the DNA-gold nanoparticle gels as Raman substrates, samples were prepared from 50 nm gold colloids functionalized with DNA consisting of a 10 base-pair binding sequence and a 15 base-pair spacer. From the calculations in the previous section, we saw that the inter-particle spacing with this sequence is approximately 10 nm. Gels were prepared by DNA-gold nanoparticles with complement DNA (1:1, A:A') in PBS (10 mM PB and 100 mM NaCl). The gels were homogenized above the melt temperature for 30 minutes and then quenched. A 633 nm laser was then used to excite the gel as it was found experimentally to have better signal to noise than exciting the sample using either a 532 nm or 785 nm laser. The optimal excitation wavelength was not predicted before the measurement, since techniques were not available to measure either the near-field modes of the gel's nano-gaps or calculate them based on the inter-particle spacing. As mentioned in the introduction, the far-field absorption spectrum has been shown to not be a good predictor of the resonant near-field modes in nanoparticle systems<sup>108</sup> and our measurements support this result. The absorption spectrum for DNA-gold aggregates in solution is relatively flat from the visible through the near-infrared region (Figure 24) and therefore does not account for the wavelength dependence of the excitation wavelength.

Figure 37 shows the Raman response of three different locations in DNA-gold nanoparticle gel at 633 nm using a 50x objective. Numerous Raman bands that have previously been identified can be observed<sup>1-4</sup> and are highlighted in the plot. The DNA sequences and wavenumbers of selected Raman bands of the bases are shown in Figure 38. As the position and intensity of the Raman bands of ssDNA have been shown to be sensitive to temperature<sup>3, 110</sup>, hybridization state<sup>3, 110</sup> and oligomer configuration<sup>4</sup>, the measured results vary slightly from the nominal position of the Raman bands. Although there is approximately five times more thymine than the other bases in the DNA sequences (A and A'), thymine is not the dominant Raman signal. This result is not unexpected, since the Raman intensities for nucleotides have been shown to vary by an order of magnitude depending on the vibrational modes with adenine having the highest intensity.<sup>1, 4</sup> The intensities of the Raman signals will also depend on the position of the bases, since the response is also a function of the spatial overlap between the near-field electronic modes and the nucleotides.

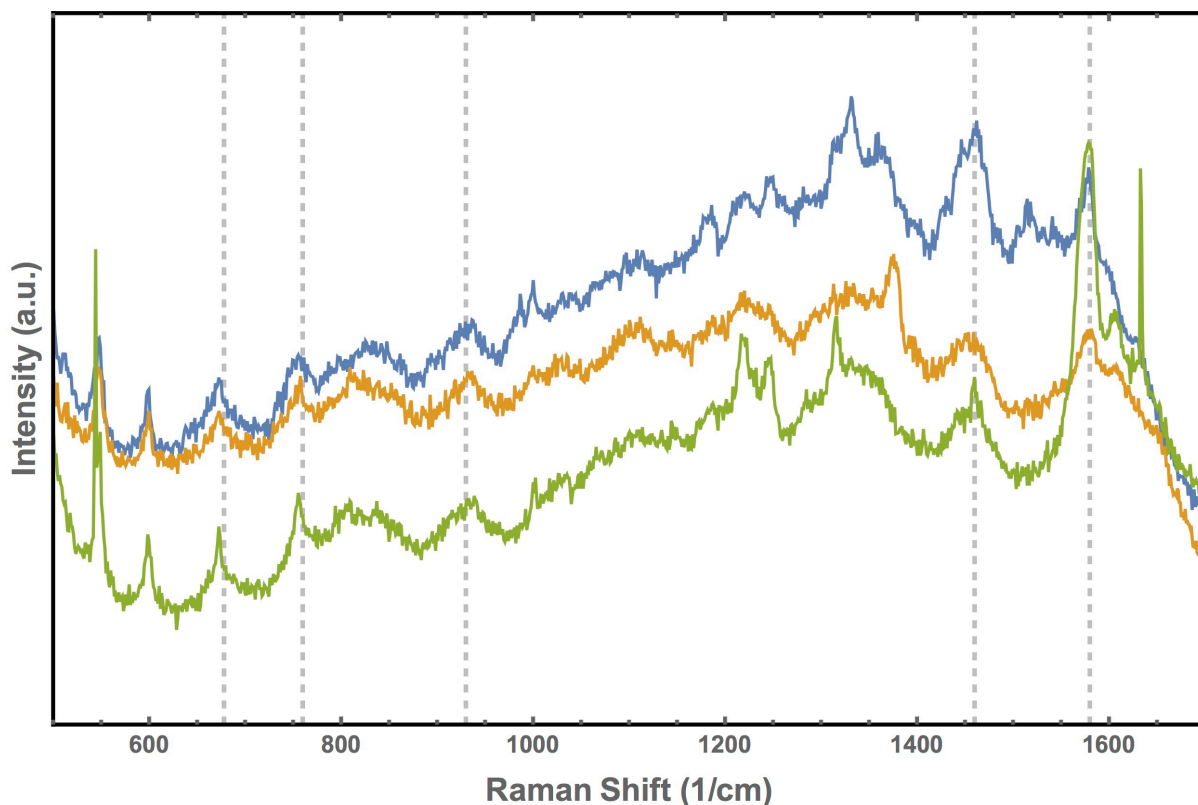


Figure 37: Raman spectroscopy of DNA-gold nanoparticle gel with the laser focused at three separate locations in the gold-nanoparticle gel. The vertical lines show selected wavenumbers of Raman active mode in DNA oligomers.

Although the coupling between the electronic and vibration modes is complex, there is a clear Raman signal from the DNA oligomers showing the gel's suitability as a Raman substrate. DNA was used as the Raman probe, since it was already present in the nanoparticle gel and it could be assured to be positioned in a hot-spot. However, any Raman active analyte that can be located near the local electric field enhancement would also be suitable.



Raman Band (cm <sup>-1</sup> )	Assignment
678	G
739	T
930	G
1485	A, T, C
1576	A

Figure 38: The DNA sequences A and A' (top). Assignments for Raman bands from the literature.<sup>1-4</sup>

The simple sample preparation of the DNA-nanoparticle gel is in contrast with the more complex methods commonly used to assemble colloids for SERS substrates. The DNA-gold gel appears also to share the same properties as assemblies of colloids with precisely engineered nano-gaps. Moreover, the micro-porosity of nanoparticle gels can also facilitate mass transport through the sample. This combination of both nanoscale and microscale features opens the opportunity for chemical species to be flushed into and out of the gel sample for microfluidic and diagnostic applications. We are currently considering additional experiments that may best demonstrate the benefits of the gel system.

## 4 Silica Nanoparticle Gels

In this chapter, I will describe how silica colloids can be self-assembled into gels with feature sizes that span the macro-, micro- and nano-scales by controlling the interaction potentials between the colloids. I will describe three methods developed to functionalize silica colloids covalently with both PEG chains and DNA oligomers. The functionalized colloids are used to form macroscopic nanoparticle gels through a spinodal decomposition mechanism. The microstructure of these gels is characterized using confocal microscopy and quantified using image analysis techniques. Finally, I will discuss how information about the gel's nanostructure can be gained from its optical scattering spectrum. The colloid-rich gel branches and the colloid-free gel pores lead to gels showing an isotropic blue color. The color of these gels is similar to those that have been observed in bird feathers. These nanoparticle gels open new routes for creating structural color where the gel structure factor is decoupled from the form factor of the individual colloids. This approach can be extended to create novel three-dimensional macroscopic materials with length-scales spanning hundreds of nanometers, which has been difficult to achieve using other methods.

### 4.1 Functionalization of Silica Nanoparticles

Colloidal silica is an important material for both large-scale applications as abrasives, stabilizers, filters and food additives as well as for more specialized applications including optical coatings, drug delivery and luminescent markers. Colloidal silica can easily be prepared by precipitating amorphous gels from precursor solutions for less demanding applications or as a monodisperse suspension using the Stöber sol-gel process.<sup>70</sup> The silica colloids used in this chapter were purchased from commercial vendors, who were able to provide silica nanoparticles with both a variety of surface functionalities and fluorescent labels inexpensively. Silica nanoparticles were prepared also in the laboratory as described in section 2.1.1 to gain a better understanding of the Stöber synthesis process.

Silane coupling reagents can be used to introduce most functional groups to the surface of silica colloids, making silica a good model system for studying the attachment of DNA to nanoparticles. Functional groups also can be introduced to the terminal ends of ssDNA oligomers either by the DNA vendor or using simple laboratory protocols. To covalently couple DNA to nanoparticles, we can draw upon the field of bioconjugate chemistry, which has a rich literature of using functional groups to cross-link chemical compounds for

diagnostic, therapeutic and research applications. The maturation of bioconjugate chemistry has led to the development of a chemical toolbox of molecules, oligomers and polymers that can be purchased commercially or synthesized using established laboratory protocols, eliminating the need to develop new organic synthesis procedures. The approach of using readily available nanoparticles, DNA strands and cross-linking reagents allowed us to focus on the specific challenges of attaching DNA to colloids in solution, rather than developing new chemical pathways.

The bioconjugate tool box consists of reagents to form covalent bonds between various functional groups including amines, thiols, carboxyls, alkynes and azides. These cross-linking reagents were used to attach the functional groups on the DNA oligomers to those on the surface of the colloids either through direct coupling of the two groups using a “zero” length cross-linker or through intermediate reagents with finite sizes. Functionalizing colloids first with an intermediate reagent can introduce other functional groups with improved reactivity on the nanoparticle surface and increase the stability of the colloidal dispersion both sterically and electrostatically. These intermediate cross-linking reagents can be either hetero-functional or homo-functional cross-linkers, but hetero-functional linkers are general preferable for coupling DNA to nanoparticles due to their inherent selectivity. Heterofunctional polyethylene glycol is the most common of these reagents, since it is chemically inert, biocompatible, soluble in both polar and apolar solvents and its length can be varied from a few repeat units (PEO) to a few thousand (PEG).

Recently, the protocols for functionalizing nanoparticles with DNA have improved significantly, even since the start of this thesis. Both the Mirkin<sup>63</sup> and Gang<sup>62</sup> groups have used physio-absorbed amphiphilic polymers to coat both hydrophobic and hydrophilic nanoparticles with functional groups that allow for subsequent DNA functionalization using amide or click reactions respectively. More recently, the Pine group has used click-chemistries to functionalize silica and titania colloids with diameters of a few hundred nanometers with DNA using azide-anchors located directly on the nanoparticle surface<sup>111</sup> and on the free ends of polyethylene glycol (PEG) chains embedded in polystyrene micro-colloids in conjunction with surfactants<sup>72</sup>.

In this section, three approaches to functionalizing silica will be presented. The approaches were developed in response to an increasing understanding of the importance of maintaining colloidal stability, controlling the electrostatic environment and minimizing the

steric barriers during the DNA-functionalization of nanoparticles. The first method involved a two-step reaction based on our groups previous experience attaching DNA to fd-viruses and gold nanoparticles. The second method was a one-step reaction based on a common approach for forming amide couples. The last strategy was developed as a general approach for stabilizing colloids sterically during the DNA-functionalization process. The development of this strategy occurred concurrently with the Pine group's approach for stabilizing polymeric colloids using a similar method.<sup>111</sup> The details of the experimental protocols can be found in section 2.1.2.

An amine to sulfhydryl linker, sulfo-SMCC, was chosen as the initial method for functionalizing silica nanoparticles with DNA, as our group had previous experience using sulfo-SMCC to functionalize fd-viruses with exposed amine groups to thiolated-DNA. Therefore, we could start by simply substituting aminated silica nanoparticles for the fd-viruses. Moreover, the approached enabled the use of the same thiolated-DNA sequence used in the gold system, eliminating the need to purchase additional DNA sequences and

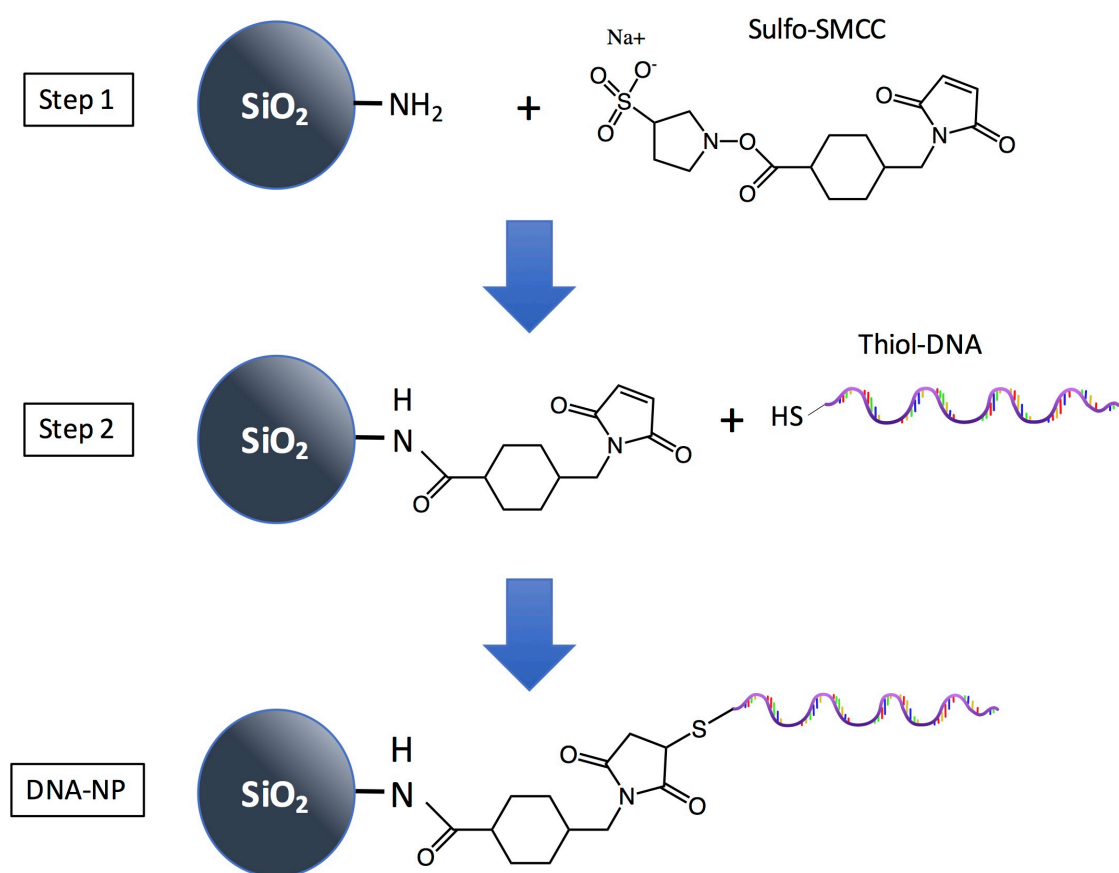


Figure 39: Cartoon of the two-step reaction for covalently bonding silica colloids to DNA by first reacting amine-functionalized nanoparticles with sulfo-SMCC (step 1) and then with thiolated-DNA (step 2).

allowing us to form composite gels consisting of both silica and gold colloids. The Alivisatos group has previously used the sulfo-SMCC chemistry to functionalize small quantities of silica-coated quantum dots with DNA.<sup>112</sup>

A protocol was developed to functionalize 100 nm silica nanoparticles using the sulfo-SMCC cross-linker and is shown in the cartoon in Figure 39. The silica colloids were first reacted with sulfo-SMCC in an 80:20, ethanol to distilled water solvent, since the nanoparticles were not stable in a pH above 5.5, due to the high surface density of amine groups on the colloids. After reacting the nanoparticles with sulfo-SMCC, the colloids were sufficiently stable in a phosphate buffer solution (pH=7.4) for the subsequent reaction with the thiolated-DNA. However, the solution did appear to be slightly turbid, suggesting there may have been some aggregation of the nanoparticles. After the DNA functionalization step, the nanoparticle suspension appeared clear, suggesting an increased stability of the dispersion. The DNA-functionalized nanoparticles also showed an increased absorption at 260nm compared with the sulfo-SMCC functionalized nanoparticles, indicating a successful reaction of DNA to the maleimide group. However, the silica nanoparticles did sediment in the timescale necessary for melt temperature measurements in quartz cuvettes, suggesting that the functionalized colloids did not form a stable dispersion. Therefore, nanoparticle sedimentation prevented accurate melt temperature measurements of these samples under thermal cycling.

To better understand the sulfo-SMCC functionalization approach, samples were prepared by mixing 100nm silica colloids coated with complementary DNA in PBS (10mM PB, 100mM NaCl) and loading them in a glass capillary. Upon mixing, the colloids immediately gelled. Temperature dependent optical microscopy then was used to see if the gelation was thermally reversible. The DNA-silica gels had a melt temperature transition between the gas and gel phase at approximately 55 °C, which was repeatable over a several heating and cooling cycles. However, above the gel melt temperature, a significant portion of the colloids remained in aggregates and some colloidal aggregates were stuck to the surface of the glass capillary at all temperatures. These non-idealities suggested that there either was not a sufficiently dense coating of DNA on the colloids to prevent irreversible aggregation and adhesion to the glass capillary or that there was significant irreversible aggregation during the functionalization process.

Although it was possible to form DNA-silica gels using the sulfo-SMCC method,

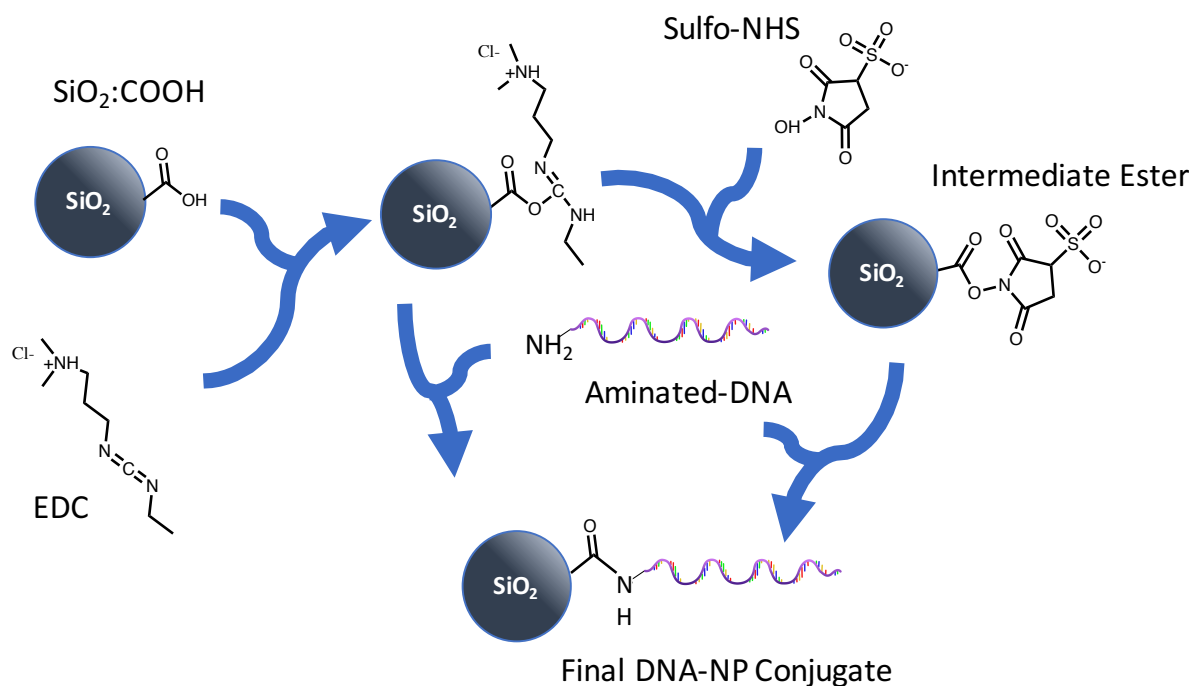


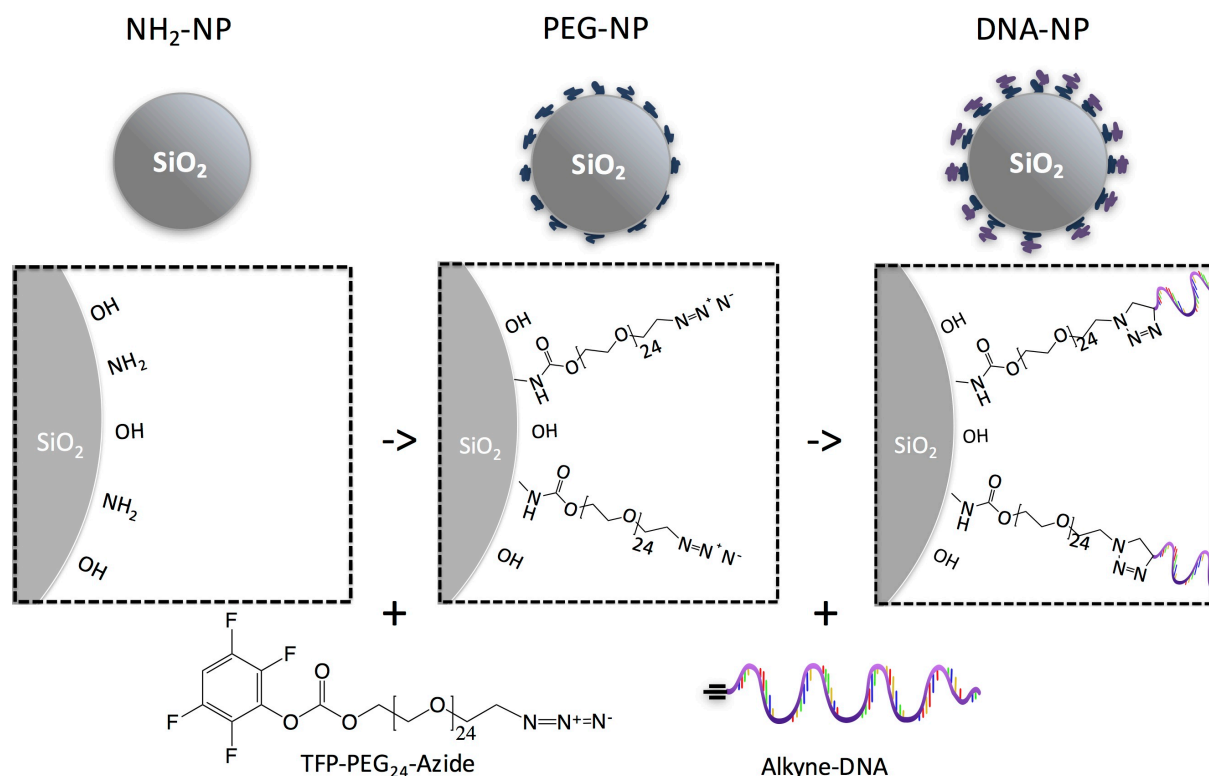
Figure 40: Cartoon of EDC/Sulfo-NHS coupling chemistry. The cross-linking reagents form an amide bond between the carboxyl group on the surface of the nanoparticle and the amine group on the end of the DNA oligomer.

alternative chemistries were pursued rather than optimizing the approach due to concerns about its inherent drawbacks. Both the maleimide and ester functionalities on the sulfo-SMCC linker are susceptible to hydrolysis, leading to concerns about diminished reactivity of the linker over the course of the functionalization procedure. The maleimide group is particularly susceptible to hydrolysis, since it is exposed to aqueous conditions throughout both the first reaction step and the subsequent washing of excess reagents. Also, the sulfo-SMCC linker has a spacer that is less than a nanometer and appeared not to provide sufficient steric stabilization through the solvent exchange process in step 1. As an alternative approach, a more simple one-step carbodiimide functionalization chemistry was explored that relies on directly forming an amide bond between a carboxyl group on the nanoparticle surface and an amine group on end of the DNA<sup>113</sup> directly, using two crosslinking reagents, sulfo-NHS and EDC, that can be added in large excess to mitigate the effect of hydrolysis.

The carbodiimide reaction using the “zero-length” cross-linking reagents can occur via two pathways leading to the same final conjugate (Figure 40). EDC can directly couple the carboxyl group on the nanoparticle surface to the amine group on the DNA. Alternatively, EDC will first couple the NHS-ester to the surface of the nanoparticle to form an intermediate. The ester can then spontaneously couple the amine to the surface of the nanoparticle before

being subsequently released into solution. Although the ester is not necessary for forming the amide bond, in practice the intermediate is critical for increasing the yield of the reaction. The intermediate hydrolyzes in hours rather than in minutes for EDC, allowing more time for the DNA to diffuse to the nanoparticle surface. Furthermore, as EDC and sulfo-NHS are much less expensive than aminated-DNA, the reagents can be added in large excesses to drive the reaction kinetics. The ester intermediate also may help stabilize the colloidal dispersion electrostatically during the reaction due to the higher pKa of the sulfate groups with respect to carboxyl groups.

The carbodiimide method proved very effective for functionalizing 100 nm nanoparticles. Nanoparticles functionalized using this approach were used to demonstrate the initial DNA-silica gels as described in the next section. However, it was not possible to functionalize 30 nm silica nanoparticles with DNA using this route under any explored experimental conditions without significant colloidal aggregation as observed by DLS. Rather than further optimizing a process that would be useful for our specific size and type of colloid, a more general approach was pursued with the hope of later applying the approach more generally.



The approach uses a heterofunctional PEG linker consisting of TFP-ester and an azide group separated by 24 repeat PEO units to couple DNA to the nanoparticle surface (Figure 41). This strategy was designed to address the universal challenge of maintaining colloidal stability in the high salt environment necessary for allowing strongly charged DNA strands to diffuse close enough to a colloid's surface to react. As an additional design constraint, we limited our procedure to using only commercially available components and reactions that could be performed in aqueous environments. Aqueous chemistries are generally simpler and safer to perform. Using commercial components also allows for the approach to be more easily adapted to other material systems and to be used by other research groups.

The PEG linker first was attached to the silica surface using an amide bond following both the sulfo-SMCC and carbodiimide approaches. The TFP-ester eliminated the need for additional coupling reagents for the PEG reaction and was selected over a NHS-ester due to the higher resistance of the fluorinated ester to hydrolysis.<sup>114</sup> The PEG spacers helped to sterically stabilize the colloids and provided an attachment point for further functionalization. The terminal azide provided a highly reactive group that is stable against hydrolysis, allowing for the excess PEG reagent to be washed away without loss of subsequent reactivity. Finally, by moving the reaction site away from the surface of the nanoparticle, the electrostatic interactions between the DNA and the nanoparticles surface are mitigated, reducing the need for optimizing the salting process commonly employed in DNA colloidal conjugates.<sup>41</sup>

In the second step, DNA is attached to the PEG coating using the copper-catalyzed azide-alkyne Huisgen cycloaddition. This reaction was chosen due to its fast kinetics, but other chemistries that are sufficiently resistant to hydrolysis could also be used. Copper ions have been shown to damage DNA through chain scission, crosslinking and oxidation<sup>115, 116</sup>, but any induced damage was not significant enough to be observed as an impediment in this work. A strained-alkyne/azide click reaction, using as a dibenzylcyclooctyne (DBCO) functionality, is good alternative and has been used successfully in concurrent investigations by both our group<sup>80</sup> and others.<sup>47, 111</sup> The azide-DBCO reaction occurs over a day rather than an hour, but does not require copper to catalyze the reaction.<sup>117</sup>

DLS and zeta-potential measurements provided a simple method for following the PEG and DNA functionalization reaction steps (Figure 42). After each reaction step, the hydrodynamic diameter of the colloids increased from 27 nm (NH<sub>2</sub>-NP) to 37 nm (PEG-NP) to 38 nm (DNA-NP). The increased hydrodynamic radius of the PEG-NP can be attributed to the

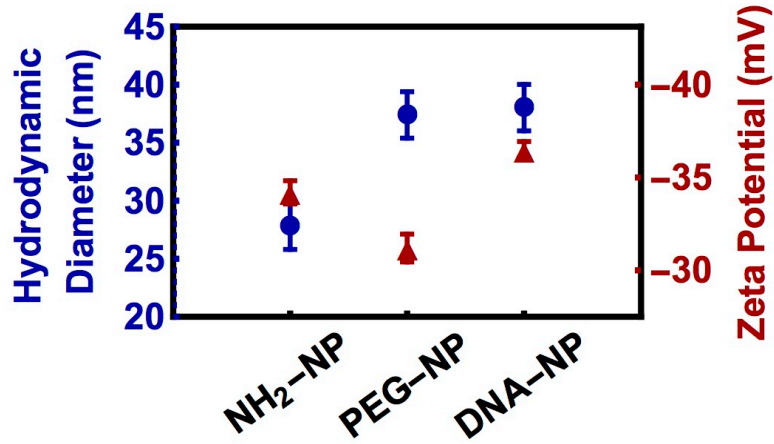


Figure 42: Dynamic light scattering (blue circle) and zeta-potential (red triangle) measurements of 30nm diameter green fluorescent silica nanoparticles performed in 10mM PB.

size of the PEG chains grafted to the surface of the colloid. In good solvent conditions, the radius of gyration ( $R_g$ ) of a PEG chain can be calculated from the number of repeat units ( $N=24$ ) and the persistence length of a unit ( $a=0.37\text{ nm}^{118}$ ) and is approximately  $2.5\text{ nm}^{94}$ .

$$R_g = a N^{\frac{3}{5}} \quad (26)$$

Single-stranded DNA has a persistence length of  $\sim 1\text{ nm}^{33}$ , which corresponds to 3 base-pairs ( $N = \frac{22\text{ base-pairs}}{3} = 7.33$ ) leading to a  $R_g$  of approximately  $3.3\text{ nm}$  for the oligomers used here. Since the tethering point of the ssDNA can be located throughout the volume of the PEG chain, it is reasonable that the addition of the ssDNA strand to the surface of the nanoparticle will not have a large effect of the hydrodynamic radius of the final nanoparticle composite. DLS measurements showed negligible aggregation after both PEG and DNA reaction steps.

The zeta-potential of the nanoparticles ( $-35\text{ mV}$  to  $-31\text{ mV}$ ) became slightly more positive after the PEG reaction step and then became more negative again after the DNA reaction step ( $-36\text{ mV}$ ). The small decrease in the zeta-potential of the nanoparticles after the PEG reaction step can be attributed to an increase in the diameter of the nanoparticles after the coating, where the slip-plane of the solvation sphere is pushed further away from the surface of the nanoparticle.<sup>119</sup> Neutralizing the amine groups on the surface would otherwise make the zeta-potential more negative at a pH of 7.4. The small change in zeta potential is due to the relatively low density of the PEG coating and short length of the PEG chains. In our work with functionalizing polymeric colloids with PEG, we have observed that the zeta-

potential of PEG coated colloids approaches zero with dense coatings of 5kDa MW PEG chains<sup>80</sup>, the chain lengths being five times longer than used here. It also has been shown that the zeta-potential of silica colloids with physically absorbed PEG chains decreases with both increased molecular weight and the number of absorbed chains.<sup>120</sup> The zeta-potential after DNA conjugation becomes more negative, which we attribute the increase in surface charge due to the strongly charged backbone of the DNA oligomers.

Although the DLS and zeta-potential measurements are simple to perform, both measurements have inherent uncertainty in the results, since they rely on fitting data. Silica colloids have a broad size distribution, especially below 100nm, but since DLS measures the average hydrodynamic diameter, the measurement should reflect a shift in the size distribution. Nonetheless, the results should be taken with caution as such a small change in diameter cannot be resolved with absolute certainty.

Fluorescent assays showed that the areal density of PEG chains was approximately  $10^{12}/\text{cm}^2$  ( $104 \text{ nm}^2/\text{oligomer}$ ) or 27 chains per 30nm diameter colloid. The DNA coating density was found to be similar to that of the PEG coating density within experimental error ( $\pm 5\%$ ). This finding suggests that all grafted PEG-azide ends were successfully functionalized with DNA via click chemistry. The complete reaction of the azide groups on the PEG oligomers with the alkyne functionalized DNA was somewhat unexpected as additional Cu(1) stabilizing ligands are often necessary to achieve 100% loading.<sup>121</sup> The high yield of our reaction is potentially due to the large excess of the alkyne groups with respect to the azide groups.

The surface coating density corresponds to an approximate inter-anchor spacing ( $d$ ) of 10 nm, which is larger than twice the radius of gyration of the PEG chains ( $R_g(\text{PEG}) \approx 2.5$

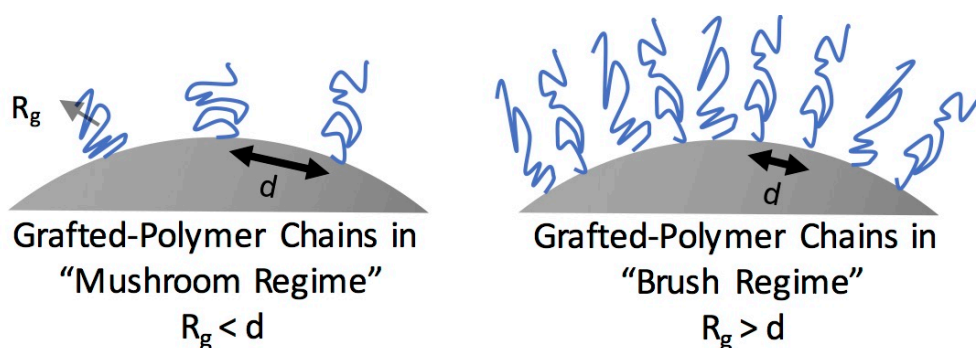


Figure 43: Cartoon depicting polymer chains grafted to the surface of a colloid in a good solvent conditions. When  $R_g < d$ , the chains are in the "mushroom" regime (left) and when  $R_g > d$ , the chains are in the "brush" regime (right).

nm). This result suggests that the PEG chains are in the mushroom (unstretched) regime rather than the “brush” (stretched) regime (Figure 43).<sup>94</sup> Therefore, there are likely exposed areas on the silica surface. This grafting density is approximately 2 times lower than what has been achieved by silanization of silica colloids with azides and DBCO-DNA<sup>111</sup> and an order of magnitude less than what has been achieved by coating colloids with azide functionalized amphiphilic polymers and DBCO-DNA<sup>47</sup>.

Since the nanoparticle coating density in this work was limited by the PEG coating density, a series of experiments were designed to test whether the coating density could be increased as a function of pH. At lower pH values, the hydrolysis rate of the TFP-ester decreases, allowing more time for the PEG chains to diffuse to the nanoparticle surface without a loss in reactivity. While at higher pH values more of the amine groups deprotonate, increasing the number of available surface reaction sites. For reactions in aqueous buffer solutions, the highest density of PEG coating was found to be in PB buffer (pH=7.4) as measured by the fluorescence assay (Figure 44). A ten-fold increase in the concentration of PEG in solution did not increase the coating density in PB.

However, it was found that it was possible to increase the density of the PEG coating by approximately 50% using the mixture of anhydrous DMSO and TEA in ambient conditions.

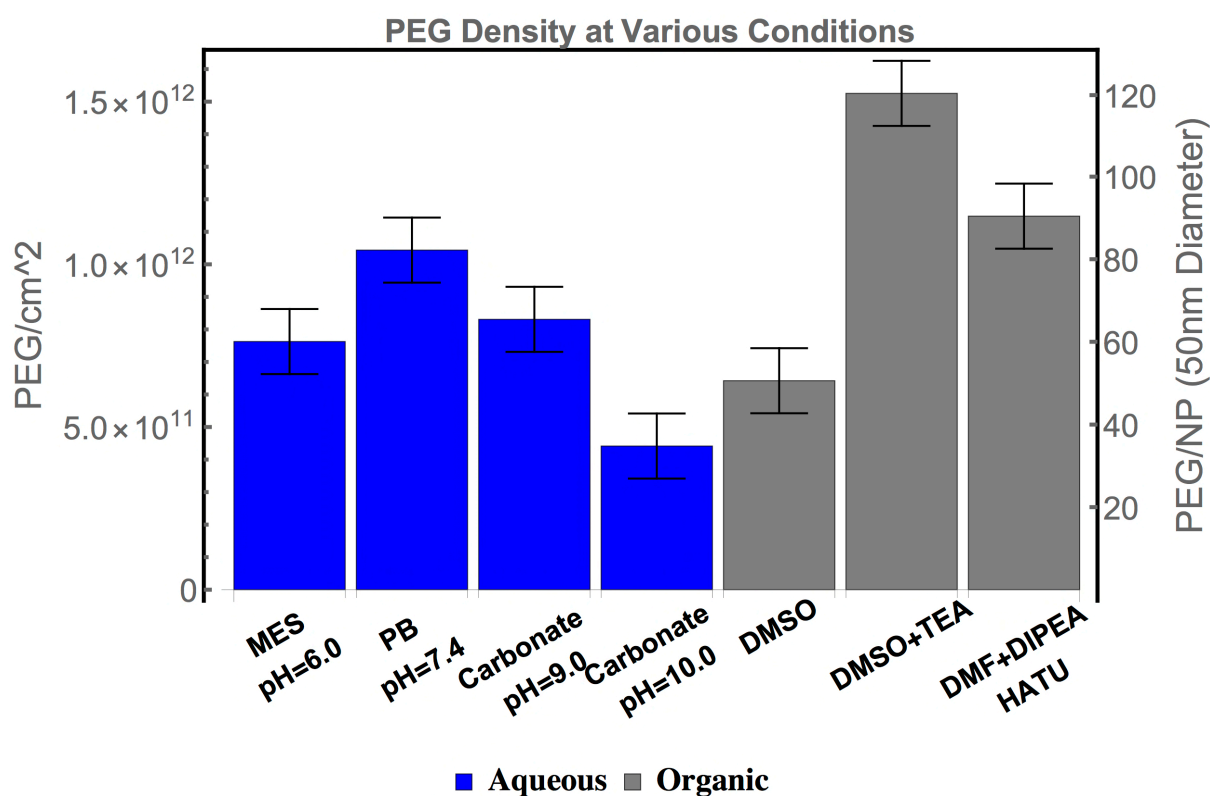


Figure 44: Histogram for the surface density of PEG ligands on the surface of silica nanoparticles under various aqueous and organic conditions.

This suggests that the density of the coating could be improved using organic solvents and hydroscopic conditions (Figure 44). Although all samples shown in Figure 44 were formed using amide bonds between 50nm diameter silica colloids and PEG oligomers, the DMF+DIPEA+HATU mechanism was slightly different as it involved silica colloids functionalized with carboxyl groups and PEG oligomers functionalized with amine groups. This reaction was catalyzed by HATU (1-[Bis(dimethylamino)methylene]-1H-1,2,3-triazolo[4,5-b]pyridinium 3-oxid hexafluorophosphate), which is a common reagent in peptide coupling.

The increase in grafting density in organic solvent conditions was not sufficient to move the PEG chains from the mushroom to the brush regime, since reaching the brush regime would require twice the coating density we have achieved in the best aqueous conditions. Therefore, our later experiments in this system used the nanoparticles prepared in PB, since the procedure did not require solvent exchange. To significantly increase the PEG grafting density, it is likely that we would need to address the steric barrier of the grafted PEG chains.

It is expected that the generality of the DNA-PEG functionalization approach can be extended to allow for the attachment of DNA to nanoparticles of other materials due to the range of terminal functional groups that can be introduced to the PEG chains. Subsequent experiments have shown the functionalization of silica and titania nanoparticles through silanization using PEG chains with terminal silane groups. The attachment of PEG chains to hydrogenated silicon nanoparticles through the hydrosilylation of a terminal alkene group is discussed in the Appendix.

## **4.2 Microstructure of 100nm silica gels**

DNA-NP gels were formed using the 100 nm silica colloids functionalized with DNA using the one-step carbodiimide approach. The carbodiimide system provided a convenient method for producing large quantities of highly stable dispersions of DNA-functionalized silica colloids which showed no aggregation in DLS measurements, enabling the demonstration of fully thermally reversible silica nanoparticle gels. This achievement was an important step, as it allowed us to demonstrate the applicability of DNA-mediated self-assembly to a materials system without significant optical absorption and therefore suitable for structural color experiments. As the gels are non-absorbing, it also allowed for the internal gel structures to be imaged using confocal microscopy and studied using image analysis

techniques of the micrographs. The microscopy studies of the gels allowed us to begin to develop a greater understanding for how the morphology of DNA-nanoparticle gels scale with both the colloidal diameter and gel volume fraction ( $\phi$ ).

The DNA-silica gels were formed by mixing concentrated solutions of 100 nm diameter green fluorescent colloids coated with complementary DNA (A and A') and 2M NaCl to obtain colloidal gels in PBS (10mM PB and 100mM NaCl). The nanoparticle samples were loaded into glass capillaries with rectangular cross-sections (.2mm x 4mm, Vitrocom) and sealed with a two-component epoxy. The samples were then heated to a temperature above the melt temperature (70 °C) and cooled at a fixed rate (1 °C/min) using a home-built Peltier heating stage. The gel microstructure was then imaged at room temperature using a confocal microscope with an oil immersion objective.

When the nanoparticles functionalized with complementary DNA are mixed together in PBS, the nanoparticles form dense aggregates (Figure 45). Once homogenized by heating above the melt temperature and cooled, the nanoparticles formed a gel network consisting of colloid-rich branches and colloid free pores. Samples made using non-complementary DNA (only colloids functionalized with A DNA) remain as colloidal dispersions at all temperatures. To gain an understanding of how the morphology of the gel branches and pores scale with the gel volume fraction, gel samples at  $\phi = 1\%$ ,  $2\%$ ,  $5\%$  and  $10\%$  were prepared, imaged using confocal microscopy and the micrographs were analyzed using chord analysis (Figure 46). Gel samples with  $\phi = 1\%$  formed discrete aggregates rather than a percolating gel and therefore were not suitable for chord analysis. Gel samples with volume fractions above  $10\%$  colloidal

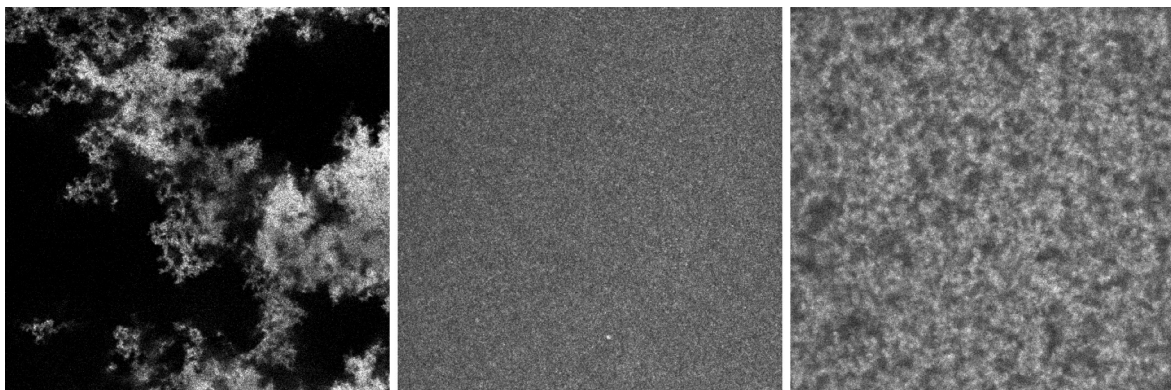


Figure 45: Confocal micrographs of DNA-NP gels before (left) and after (right) homogenization and nanoparticle dispersion consisting of DNA-NP that are not complementary (center). All samples were prepared from dispersions of 100nm silica colloids functionalized using the carbiidimide chemistry with  $\phi = 2\%$  in 100mM NaCl, PBS.

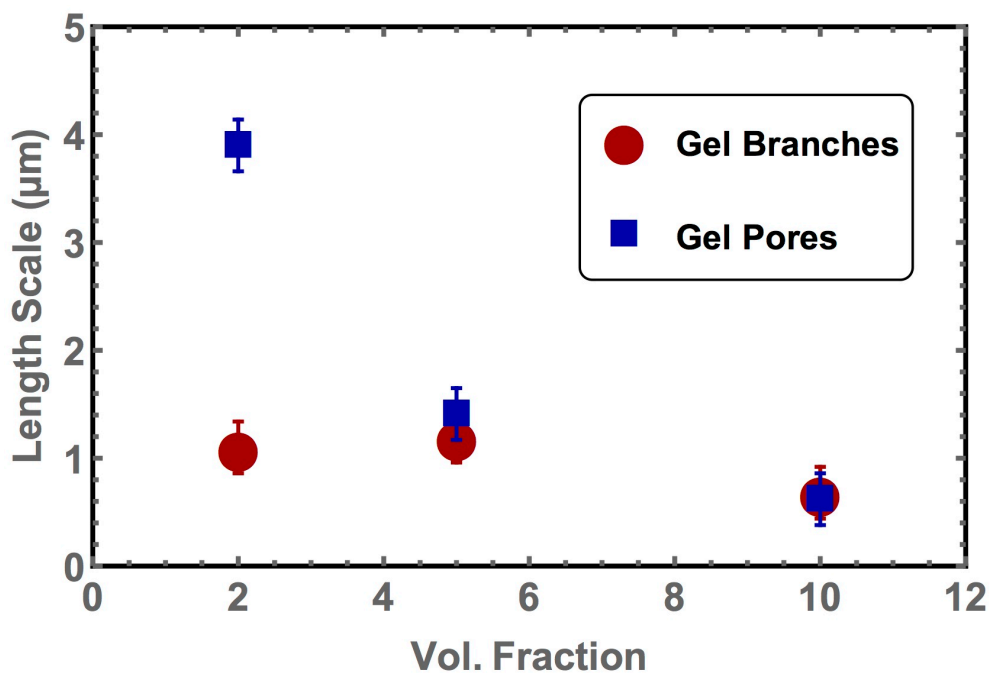


Figure 46: Chord analysis of 100nm DNA-silica nanoparticle gels as a function of volume fraction. Gels were cooled from the melt at 1C/min and the nanoparticles were functionalized with DNA using the one-pot carbodiimide approach.

volume fractions had features spanning only a couple of pixels in confocal microscopy and the underlying structure couldn't be resolved with confidence.

As the colloidal volume fraction increases, the colloid-rich phase fills a greater area of the confocal microscopy images. The decrease in the micro-porosity with increased  $\phi$  is reflected numerically in the decrease in the characteristic length-scales of the pores in the chord analysis. The length-scale of the colloid-rich phase remains largely unchanged with increased  $\phi$ . Therefore, increased  $\phi$  leads primarily to a greater number of micro-gel branches in the system rather than a thickening of the branches. This result is consistent with our previous experiments in DNA mediated colloidal gels in the polystyrene<sup>13</sup> and gold-virus systems<sup>8</sup> and has also been predicted previously in simulation studies<sup>21</sup>.

As discussed in the introduction, one of the goals of this thesis was to create nanoparticle gels showing structural color. The feature sizes of 100 nm silica colloidal gel branches are above the range where they can be expected to selectively scatter certain wavelengths of visible light more strongly, since the gel branches in these gels will be a few hundred nanometers. Therefore, nanoparticle gels were also prepared using the 30nm silica colloids prepared using the two-step click chemistry approach.

### 4.3 Gels formation mechanism in 30 nm silica gels with DNA and PEG

The development of the two-step DNA-PEG nanoparticle functionalization approach allowed for the functionalization of 30nm colloids with DNA, which was inaccessible using the carbodiimide approach. Gels formed using smaller diameter colloids will have thinner diameter gel branches and smaller pores that we expected to selectively scatter visible light based on extrapolating our results in the 100 nm diameter silica and 500 nm polystyrene colloid systems<sup>13, 21</sup>. While performing control experiments on the PEG-NP intermediates, we were surprised to find that they also formed thermally reversible gels that appeared to be have similar morphologies to the DNA-NP gels. In this section, the gel formation mechanisms in both gels prepared from dispersions of DNA-NPs and the PEG-NP intermediates using the two-step click-chemistry functionalization approach are discussed. The gel formation mechanism in the PEG-NP has not been well documented in the literature to our knowledge.

Colloidal gels were formed by mixing concentrated solutions of green fluorescent colloids coated with either complementary DNA (A and A', at a 1:1 ratio) or PEG and 2M NaCl to obtain colloidal gels with volume fractions,  $\phi$ = 1%, 2%, 5% and 10% in PBS. The suspensions were loaded into glass capillaries with rectangular cross-sections (0.2 mm x 4 mm) and sealed with a two-component epoxy.

The melt transition temperature of the  $\phi$ = 2%, DNA-NP gel was estimated by heating a sample from 25 °C to 75 °C and imaging it at 10 °C intervals (Figure 47). A phase transition from the as prepared colloidal gel to the gas phase was observed between 55 °C and 65 °C. When the sample was cooled again below the melt temperature, a homogenized colloidal gel was formed. Although the melt transition of the DNA-NP was sampled every 10°C, the phase transition for the DNA-NP is expected to occur over a few °C, due to the collective binding of the DNA strands.<sup>28, 40</sup> In systems with very high DNA grafting densities, the melt transition can be as sharp as 1°C.<sup>8, 40</sup> Observations of different systems of DNA-functionalized colloids supports the assumption that the melt temperature of DNA-NP gels is independent of volume fraction.<sup>13, 80</sup> By imaging the gels as a function of temperature we could obtain approximate melt temperatures of the gels, which otherwise would have been challenging. First, the relatively low DNA grafting density will lead to a broad melt transition of the colloidal gels.

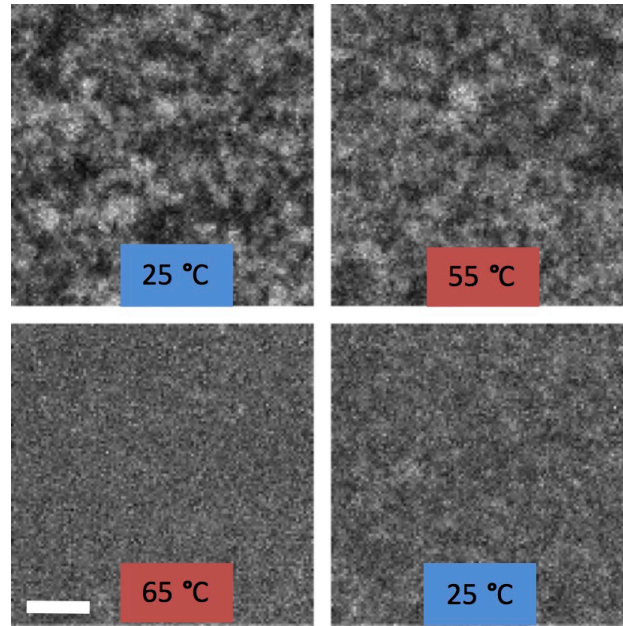


Figure 47: Confocal micrographs of DNA-NP sample with  $\phi=2\%$  starting at 25 °C, heated to 55 °C, 65 °C and subsequently returned to 25 °C. The gel transitions from the gel to the gas phase is between 55 °C and 65 °C. Scale bar is 20 $\mu\text{m}$  for all micrographs.

Second, the individual colloids cannot be resolved using conventional optical microscopy, which would be necessary for counting the fraction of colloids in solution compared to aggregates to generate a melt curve.

Using a similar heating and imaging procedure, we were surprised to find that the  $\phi=2\%$ , PEG-NP samples also underwent a thermally reversible melt transition, albeit at a lower temperature (between 45-55 °C). At low temperatures, the material is a gel and at high temperatures, a colloidal dispersion, similar to the DNA-NP gels. However, the melt transition of the PEG-NP may not be volume fraction independent as the gel formation mechanism is not determined by DNA hybridization. The melt temperature of the PEG-NP is phenomenologically different from the cloud point transition that has been observed in polymer-coated nanoparticle systems that aggregate upon heating<sup>122, 123</sup>, as here the colloidal aggregation occurs on cooling.

Grafting PEG chains to the surface of the silica colloids introduces two possible mechanisms for an additional attraction term to the colloidal interaction potential (Figure 48). First, the PEG chains on a colloid could interact with PEG chains on adjacent colloids. This mechanism is very unlikely, since at these temperatures and salt conditions the PEG chains are in good solvent conditions.<sup>122</sup> Alternatively, there is the potential for the PEG chains on one colloid to bridge to the exposed surface of adjacent colloids, since the PEG chains are in

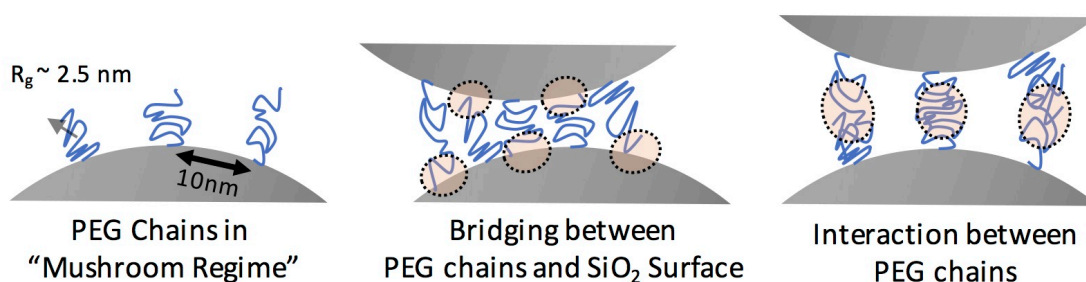


Figure 48: Cartoon depicting PEG chains in a good solvent in (left). Attractive interactions between PEG chains and the surface of the silica colloid (middle) and PEG chains on adjacent colloids (right). Interactions between PEG chains are unlikely to be the source of the attraction potential, since the PEG chains are in good solvent conditions. Ellipsoids highlight the areas of interaction in the 2D cartoon.

a relatively sparse “mushroom” regime rather than a dense “brush” regime. It has been shown that even in good solvent conditions, PEG chains have some propensity to adsorb to bare silica surfaces. In an earlier study, we have shown that bare silica beads stick to DNA-brushes with free ssDNA ends and to PEG chains at the pH and salt concentration we used here.<sup>124</sup> Moreover, PEG chains have been shown to transition from being non-adsorbing to weakly adsorbing on colloids as aqueous media become worse solvents for PEG.<sup>125</sup> Such polymer to surface interactions or bridging attractions have been shown to lead to colloidal aggregation under certain conditions.<sup>125, 126</sup>

In our PEG-NP system, we hypothesize that the free ends of the PEG chains bridge to the uncoated portions of adjacent silica colloids at low temperatures. When the sample is heated, the colloids become dispersed forming a colloidal gas phase as the increased thermal motion of the colloids is high enough to overcome the weakly attractive van der Waals interactions between the PEG chains and the bare colloid surfaces as the energy of the interaction will be of the order of a few  $k_B T$ .<sup>127</sup>

In water, PEG chains have both a lower and upper critical solution temperature (LCST, UCST). Shay et al. showed that the critical temperature for PEG-NP aggregation can be almost 100 °C lower than the LCST of free PEG chains in solution, which is about 170°C.<sup>122</sup> A more recent numerical study suggests that the phase transition in colloidal suspensions with low-PEG grafting densities are most likely due to polymer bridging.<sup>128</sup> The lower critical temperature of PEG-NPs can be further reduced by increasing the salt concentration in solution.<sup>123</sup> In this context, it is important to note that our PEG-NP samples in PB buffer and

no added salt (10 mM, 0 M NaCl) remained in the gas phase throughout the explored temperature range.

In other experimentally relevant colloid-polymers systems, the polymer chains were not grafted to the colloids.<sup>125, 126</sup> As a result, a low temperature bridging attraction could not be observed due to competing processes. In cases where the polymers were strongly absorbed to the colloid surface, the colloids did not aggregate due to being sufficiently sterically stabilized by the densely absorbed polymer.<sup>41</sup> Alternatively, in systems where the polymers were not strongly absorbed to the colloids, the colloids did aggregate at low temperatures, but the transition was instead driven by a depletant interaction<sup>125</sup>, which we do not have in our system due to the absence of free polymers.

We plan to further investigate the phase space for the observed gelation transition in the PEG-NP through varying the PEG grafting density, salt concentration, pH and PEG molecular weight. We expect that the system of silica colloids with a low density of grafted PEG chains offers an alternative approach to forming macroscopic colloidal assemblies and an opportunity to study further polymer-colloid interactions, which are currently not yet fully understood.

#### **4.4 Microstructure of DNA-PEG and PEG 30nm silica gels**

Confocal microscopy was used to study the microstructure of gels made from the DNA-NPs and the PEG-NP intermediates down to the optical diffraction limit, with a pixel volume of approximately 200 nm x 200 nm x 500 nm. Colloidal gels were formed by mixing concentrated solutions of green fluorescent colloids coated with either complementary DNA (A and A') or PEG and 2M NaCl to obtain colloidal gels with  $\phi=1\%$ , 2% and 5% in PBS (10 mM PB and 100 mM NaCl). Within each pixel, the intensity will be proportional to the number of colloids inside the volume, such that the underlying nanostructure is averaged over a pixel (Figure 13). Fluorescent NP gels with 10% colloidal volume fractions, prepared by transferring the sample from the gas into the spinodal decomposition region, had features spanning only a couple of pixels and the microstructure could not be resolved with confidence. Of course, this challenge was also present in the 100nm colloid system, but was less significant as approximately 24 100 nm colloids can be densely packed inside a pixel compared with 897 30nm colloids.

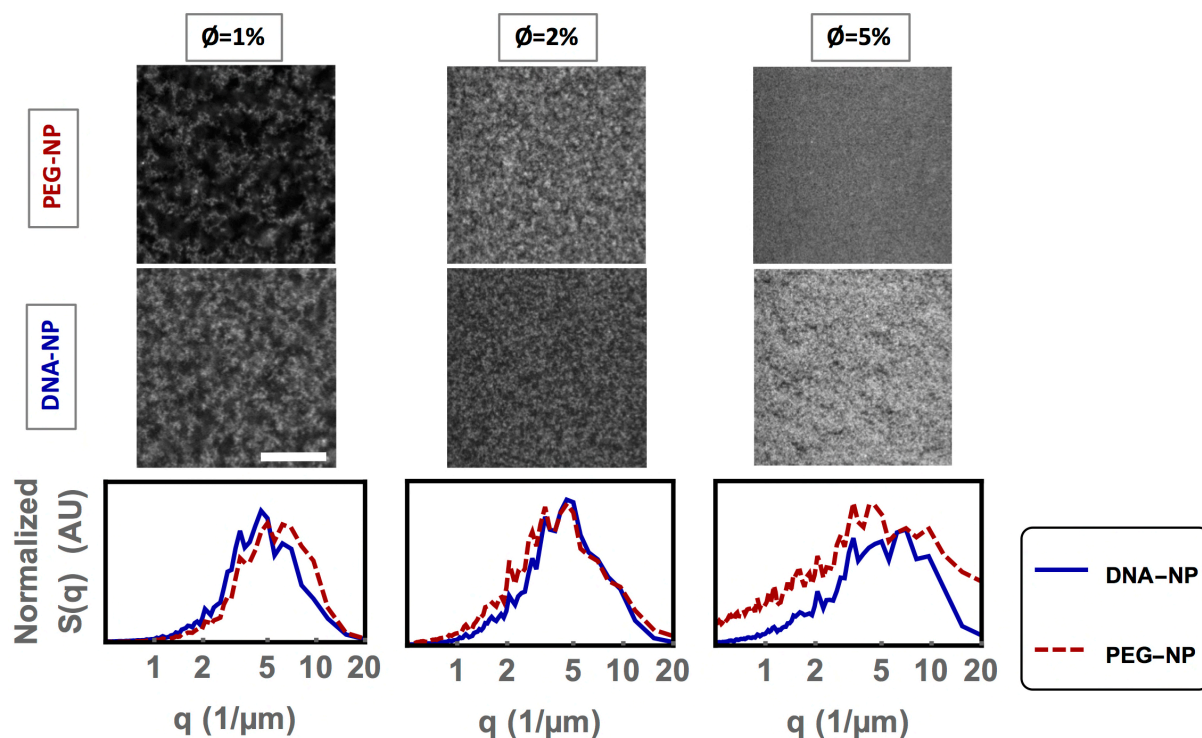


Figure 49: Confocal images and their respective structure factor,  $S(q)$  of DNA-NP and PEG-NP gels at  $\phi=1\%$ ,  $2\%$  and  $5\%$ . The intensity of the structure factors has been normalized to the maximum of the structure factor of each sample and the x-axis is a log-scale. All samples were measured at room temperature near the bottom surface of the capillary. Scale bar is  $20\mu\text{m}$  for all micrographs.

Nonetheless, the confocal images taken at lower volume fractions ( $\phi=1\%$ ,  $2\%$  and  $5\%$ ) do give valuable insight into the gel microstructure that can be used to understand the gel branch morphology. We gain further insight into the gel nanostructure by measuring the gel's optical reflectivity in the next section. As  $\phi$  increases, the colloid-rich phase fills a greater area of the confocal images. The decrease in the micro-porosity with increasing  $\phi$  is reflected numerically in both an increase in  $S(q)$  at higher wave-vectors and the decrease in the characteristic length-scale of the pores extracted from chord analysis (Figure 50). The characteristic length-scale of the colloid-rich phase remains constant with increased  $\phi$ . Therefore, an increased  $\phi$  leads to a greater number of micro-gel branches in the system rather than a thickening of the branches, as was previously demonstrated in simulation studies<sup>21</sup>. The  $S(q)$  data has a broad peak and lacks of periodicity with  $q$ , which is typical for the absence of long-range order.

In the DNA-NP system, the aggregation behavior has the additional contribution from the DNA hybridization energy, which provided a binding strength of the order of  $10k_B T$ .<sup>35</sup> Despite the difference in binding mechanism between the PEG-NP and DNA-NP gels only small differences between the measured  $S(q)$  was observed. Nonetheless, the additional

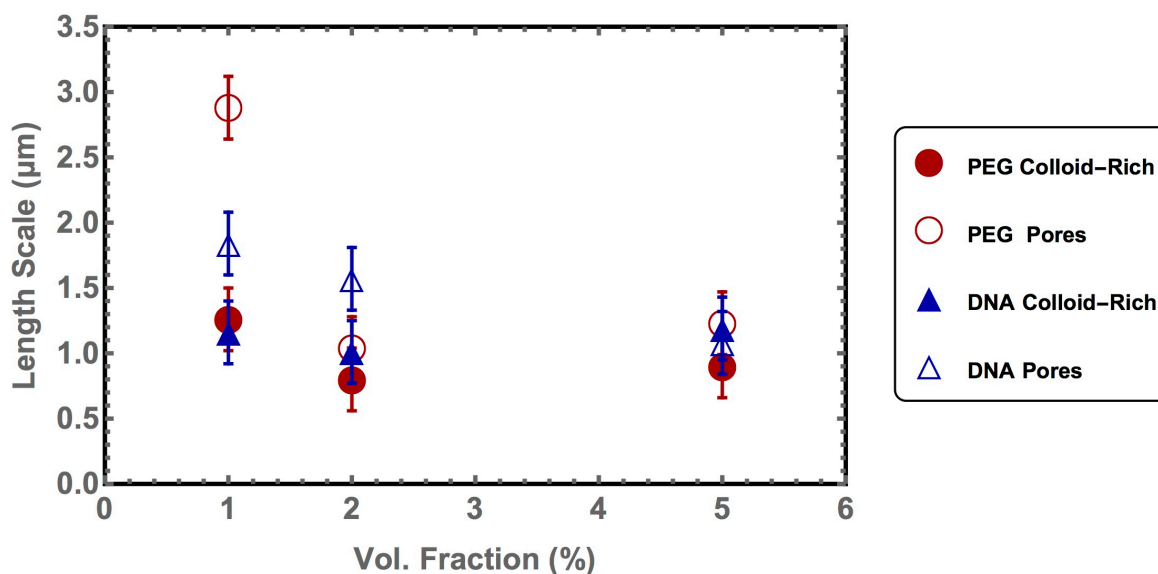


Figure 50: Chord distribution analysis of micrographs made of 30nm silica nanoparticle gels formed from both the DNA-NPs and PEG-NPs.

attraction provided by the DNA hybridization leads to a narrower  $S(q)$  at higher volume fractions for the DNA-NPs. This is in agreement with the findings that strongly attracting colloids simply show more rapid kinetic arrest when quenched into the spinodal decomposition region<sup>13, 21</sup> than weaker short-ranged attractive interactions of less than a few  $k_B T$ .<sup>127</sup> This supports that the weaker PEG-colloid attraction allows for rearrangements within the gel phase, so that the PEG-NP gel becomes more compact over time, which is not possible in DNA-NP gels. We will see later that there is evidence of rearrangement of the PEG-NP gels as they age. In the DNA-NP gels, the increased attraction from the complementary DNA strands prevent the colloids from arranging into a lower-free energy minimum.

Because the samples with low  $\phi$  scattered only weakly, it was possible to image deep inside the samples. In fact, the depth of imaging inside the gel with the oil-immersion objective was limited only by the relatively short working distance of the objective and the wall thickness of the flat capillaries. Confocal stacks of images were taken up to 70  $\mu\text{m}$  into the gel. Although the gel appeared homogenous in plane at a given height in the sample, the local colloidal volume fraction in the gel decreased as we imaged deeper into the gel. This is due to sedimentation of aggregates during gel formation. In the colloidal gas phase, the 30nm diameter nanoparticles are homogeneously distributed in all 3 dimensions as the gravitational height of the particles is larger than the thickness of the capillary itself. However, when the particles aggregate their gravitational height decreases, promoting sedimentation. A similar

	PEG-NP gels			DNA-NP gels		
$\phi$	1 %	2%	5%	1%	2%	5%
<b>Results from chord analysis, <math>\lambda \pm 0.2</math> [<math>\mu\text{m}</math>]</b>						
$\lambda_{\text{pore}}$	2.9	1.0	1.2	1.8	1.6	1.1
$\lambda_{\text{gel}}$	1.3	0.8	0.9	1.2	1.0	1.2
<b>Results from structure factor analysis, <math>2\pi/q_{\text{max}}</math> (<math>\sigma</math>) [<math>\mu\text{m}</math>]</b>						
$2\pi/q_{\text{max}}$	1.2 (0.6)	1.8 (1.1)	1.4 (1.3)	1.4 (0.7)	1.9 (0.8)	1.6 (1.2)

Figure 51: Numerical summary of the chord analysis and structure factor analysis for both the PEG-NP and DNA-NP gels. This information is also presented in the Figure 49 and Figure 50. The error of the chord analysis technique was determined by the resolution ( $d[x,y]$ ) of the confocal microscopy technique. The standard deviation,  $\sigma$ , was calculated by fitting the structure factor analysis presented in Figure 49 in real-space  $S(2\pi/q)$  with a normal distribution.

effect was observed in a system of DNA-functionalized fluorinated colloids<sup>80</sup> and suggests that the binding between the particles is sufficiently fast and strong to withstand the full collapse of the gel due to gravity. Nevertheless, the gel does appear to percolate throughout the capillary volume for values of  $\phi$  down to 1%. Electronic percolation has also been observed in similar sized carbon particles with  $\phi=1\%$ .<sup>129</sup>

An effective volume fraction of the gel cannot be calculated from the chord analysis at different depths into the gel, because it is unclear how the colloids pack inside the confocal pixel volume. Small-angle X-Ray scattering (SAXS) could be used to measure the colloidal packing density and is scheduled for December of this year. Nevertheless, characteristic length-scales for the gel-rich and colloid-poor regions could be extracted using chord analysis and compared to the results from the structure factor analysis (Figure 51). A difference in values from the  $S(q)$  and chord analysis can be expected as they measure different quantities. The  $S(q)$  approach is a function of the length-scales of both the colloid-rich phase and the colloid-poor phase, while the chord analysis technique looks at the two length-scales independently. As a result, the  $S(q)$  can be dominated by either length-scales of gel pores or branches or a sum of the two.

#### 4.5 Optical Spectroscopy and Nanostructure Analysis of Silica Gels

Since the nanoscale features of the gel branches and pores are below the optical diffraction limit, an alternative approach to studying the gel structure was required. Here, the optical scattering spectrum of the gel was used to gain information about the underlying

nanostructure. Alternative approaches to studying the gel nanostructure more directly are discussed in the next section.

The two relevant length-scales for understanding the optical properties of the nanoparticle gels are those of the individual colloid-rich gel branches and the colloid-free pores. The gel can be expected to scatter visible light when the dimensions ( $a_r$ ) of either become similar to the wavelength of light ( $a_r = \lambda_r / (2n_{eff})$ ). An effective index of refraction of the colloid-rich phase ( $n=1.40$ ) was calculated using the Maxwell-Garnett relation,<sup>130</sup>

$$n_{eff} = n_{water} \frac{\sqrt{2n_{PB}^2 + n_{SiO_2}^2 + 2\phi(n_{SiO_2}^2 - n_{PB}^2)}}{\sqrt{2n_{PB}^2 + n_{SiO_2}^2 - \phi(n_{SiO_2}^2 - n_{PB}^2)}} \quad (27)$$

and assuming random-close colloidal packing ( $\phi=63\%$ )<sup>75</sup>, where the effective refractive index arises from a weighted average of the silica colloids ( $n=1.45$ ) and the buffer solution ( $n=1.33$ ). A random-close packed system represents the upper bound for the refractive index of the colloid-rich phase, since the colloids are expected to be kinetically trapped upon aggregation. This leads to a range of feature sizes that will selectively scatter visible light from approximately 143 nm for blue light (400 nm) to 250 nm for red light (700 nm). In previously published work<sup>13</sup>, 500 nm DNA-coated polystyrene colloids were found to form gel branches with an average thickness corresponding to four colloidal diameters. Colloidal branches made of four 30 nm diameter colloids correspond to the lower bound of the predicted feature size.

To study the nanostructure of the gels, samples of non-fluorescent PEG-NP and DNA-NP gels were made at  $\phi= 15\%$ , 25% and 35% in PBS in capillaries with rectangular cross-sections. The concentrated NaCl solution was added to the capillary before adding the nanoparticles and the samples were allowed to equilibrate overnight, as the gelled samples were too viscous to pipette. The gels were heated above their melt temperature for an hour and then quenched to room temperature by placing them on a thick aluminum sheet. A capillary loaded with PBS was prepared as a reference. Samples of non-coated silica nanoparticle suspensions were prepared as controls.

The scattering spectra of the gel samples in capillaries were measured in both reflection and transmission using a light microscope as described in Figure 15. A beam-splitter allowed for light to be collected simultaneously with a color CMOS camera and a spectrometer through an optical fiber. The reflected spectrum was taken from several different focal planes ( $z$ ) and locations ( $x$ - $y$ ) inside the sample and were found to be invariant

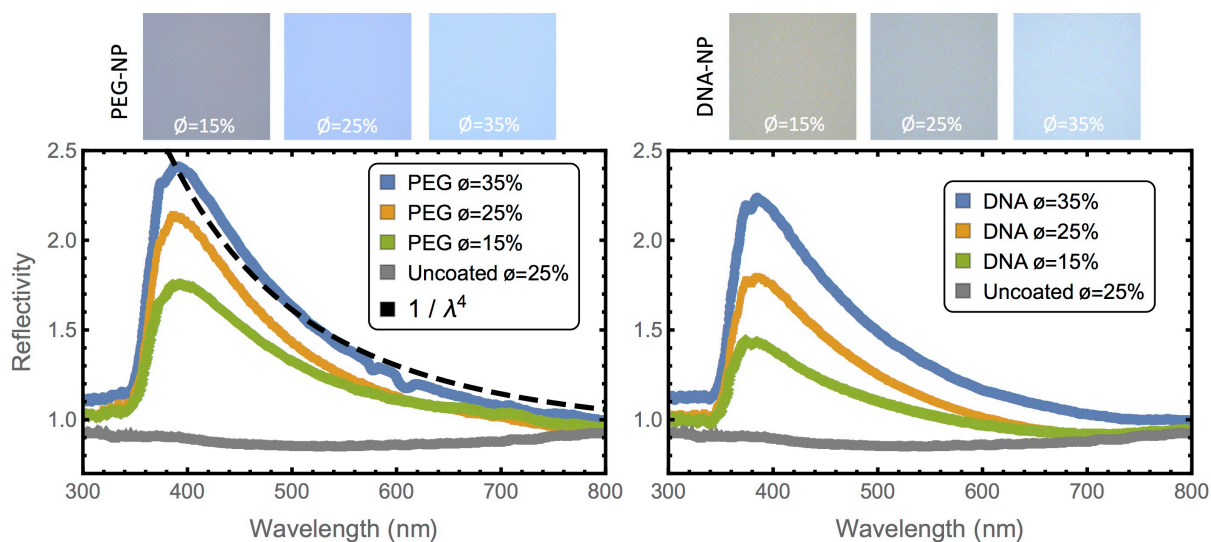


Figure 52: Spectral response (bottom) of the PEG-NP (bottom left) and DNA-NP gels (bottom right) taken perpendicular to the gel samples referenced to a capillary filled with PBS. The images (top) are taken from the center 500 pixels x 500 pixels of the camera image (43.9  $\mu\text{m}$  x 43.9 $\mu\text{m}$ ).

with position, suggesting that the samples were isotropic on the scale of the volume coupled into the optical fiber. The spectral responses of the gels were referenced to a PBS filled capillary to minimize the effect of reflections from the glass capillary and a white diffuser (certified reflectance standard) to compare our results to other works. The camera's color balance was referenced to the white diffuser.

Both PEG-NP and DNA-NP gels showed a blue color with an intensity that increased with an increased  $\phi$  of colloids in the sample (Figure 52). There is a peak in the reflectivity at approximately 385 nm. At shorter wavelengths, there is a relatively sharp decrease in reflectivity and at longer wavelengths, the reflectivity decreases more gradually and can be fitted by a  $1/\lambda^4$  dependence. The uncoated silica nanoparticles showed a relatively flat response slightly lower in magnitude than the PBS reference.

The  $1/\lambda^4$  dependence of the reflectivity is in good agreement with Rayleigh-Gans theory, which assumes both a small refractive index difference between the scattering objects and the surrounding media, and that  $a_r$  is similar to the incident wavelength.<sup>131</sup> Therefore, the spectral response supports that Rayleigh-Gans scattering primarily is responsible for the observed blue color rather than coherent scattering associated with structural color. There does appear to be some spatial variation in the gel's reflectivity, which can be seen in more detail in a five-times enlargement of a selected camera image shown in Figure 53. The sharp decrease in reflectivity at shorter wavelengths may be partially attributed to the absorption edge of silica colloids themselves and the glass capillary at

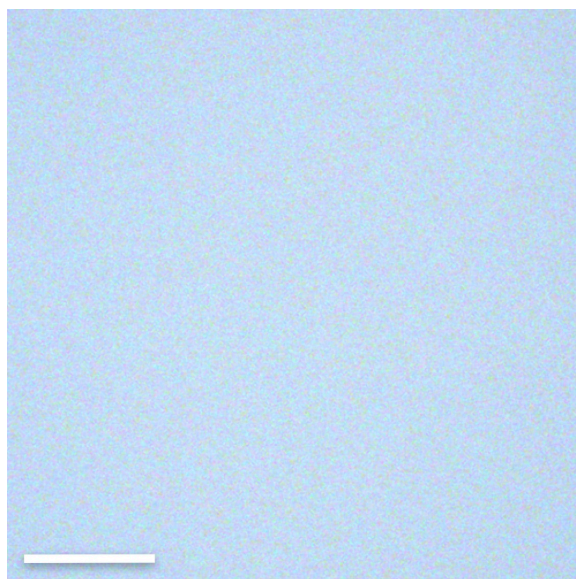


Figure 53: Camera image of the optical reflection DNA-NP at  $\phi=35\%$  (right), expanded 5x from the image in figure 7. Scale bar is 10  $\mu\text{m}$  and the image is 500 pixels by 500 pixels.

shorter wavelengths. However, the reflection spectrum was referenced against a PBS filled capillary minimizing any absorption effects. The limited impact of using glass capillaries also was confirmed by measuring the scattering spectrum in transmission. Repeating the spectral measurements with quartz capillaries (low UV absorption) would eliminate any remaining absorption effect from the glass capillary.

The magnitude of the reflectivity increases at higher  $\phi$ , while the shape of the optical response remains unchanged. We hypothesize that increased  $\phi$  leads to more branches (scatters) forming in the gel, rather than an increase in the thickness of the individual gel branches, which would be expected to change the shape of the reflected spectra. This hypothesis is consistent with the decrease in the gel micro-porosity with increased  $\phi$  from the confocal microscopy.

The stronger reflectivity of the PEG-NP gels could potentially be from the lower interaction potential of the PEG-NPs, due to the absence of the DNA interaction from the colloids' interaction potential. The lower attraction may have allowed the PEG-NPs to overcome the lower energy kinetic trap and rearrange into more compact gel arms with a higher average refractive index than the fully arrested DNA-NP gels. After about a week, the PEG-NP began to locally reach their crystalline equilibrium state (Figure 54). Such a crystallization was not observed in the gels with DNA-binding, suggesting that the stronger attraction leads to more stable gels. The decreased optical response of the uncoated

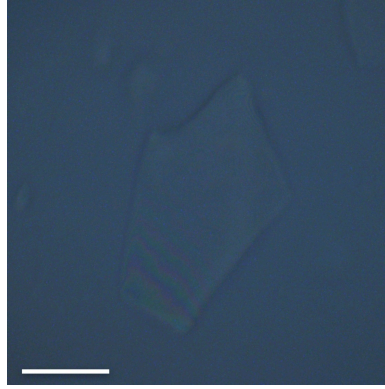


Figure 54: Optical micrograph of crystallite in observed in a PEG-NP gels one week after sample preparation. Scale bar is 20 $\mu$ m.

nanoparticle control sample with respect to the reference is likely due to the increased refractive index of the nanoparticle suspension compared to the PBS reference, which reduces the magnitude of the reflections at the solution/capillary interface.

The magnitude of the optical reflection spectra of the gels for all  $\phi$  is in the range of a single percent when referenced to the white diffuser (Figure 55). Colloidal gels formed using higher index materials could potential increase the peak intensity of the reflectivity. In bird feathers, high-index contrast structures made from proteins and air-filled pores approach 50% reflectivity<sup>56, 58</sup>.

In the artificial systems generating structural color discussed in the introduction, the structure factor is determined by the form factor of the colloids. Here, we can decouple the form factor of the colloidal building blocks from the nanoscale structure factor by starting from dense transparent colloidal suspensions that only scatter light when gelled. The transparency of the colloidal dispersions is a result of the negligible optical scattering cross-section of the colloids due to a combination of the small diameter ( $\lambda \gg d$ ) of the colloids and

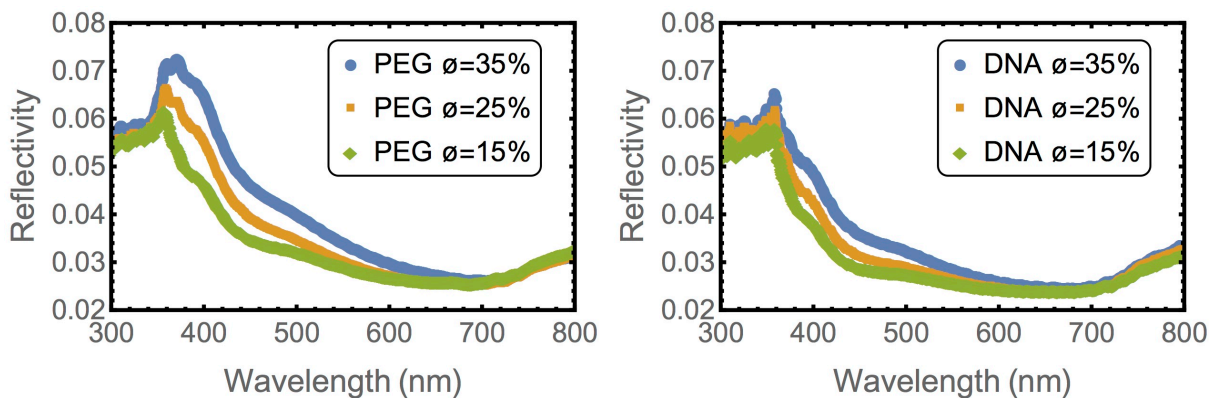


Figure 55: Optical reflection spectroscopy of the PEG-NP (left) and DNA-NP (right) at different  $\phi$  referenced to the white diffuser.

the low index contrast with the surrounding buffer solution as well as the low intrinsic optical absorption of silica. Although the Rayleigh-Gans is primarily responsible for the blue color here, decoupling the structure from the form factor may make it possible in future work to access colors that are not easily generated in other synthetic and natural systems.<sup>132</sup>

### Summary and Future work

This chapter described the development of self-assembling silica colloids gels with the goal of forming materials displaying structural color. The initial experiments using larger, 100 nm colloids were important for developing experimental techniques for studying both the properties of the functionalized nanoparticles and the DNA-nanoparticle gels. These studies led to the design and development of colloidal gels with feature sizes that preferentially scattered blue light using functionalized 30 nm silica colloids. The novel, two-step DNA-PEG chemistry presented allows for DNA-functionalization of silica colloids using only aqueous conditions and covalent bonds unlike previous methods developed by other groups. This strategy could potentially be applied to a variety of materials systems due to the flexibility of functional groups that can be attached to the PEG chains used in this approach. The PEG-NP gels present an opportunity to form nanocomposite materials using a simplified approach that may be more suitable for industrial applications.

The morphology of the nanoparticle gels can be tuned by changing the colloidal volume fraction. As  $\phi$  increases, the porosity of the gels decreases and leads to more gel branches, which preferentially reflect blue light. As  $\phi$  increases, the gel reflects more strongly, which

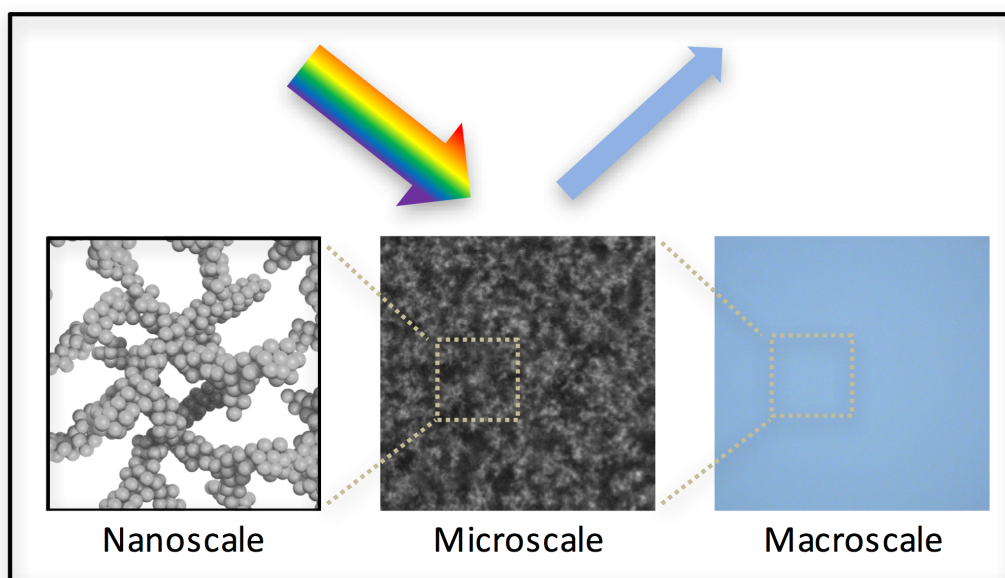


Figure 56: Silica nanoparticle gels on the nano-, micro- and macro-scales.

we hypothesize is due to more gel branches being formed rather than a coarsening of the gel branches. The magnitude of the optical reflectivity can potentially be improved using colloids with higher refractive indices and by engineering the interaction potentials of the colloids to increase the short-range order of the gel nanostructure.

The potential for generating coherence scattering between the colloidal branches remains unclear, as confocal microscopy is not able to generate a real-space image of the underlying nanostructure of such small colloids. Obtaining high quality electron micrographs of the gel that would be comparable to those taken of bird feathers<sup>56, 58</sup> requires drying the gel, which may fundamentally alter the nanostructure. One possibility to retain the structure could be super-critical drying. Our attempt at in situ scanning electron microscopy of the gel as was performed in the gold system did not allow for sufficient contrast between the silica colloids and the aqueous solution. We are currently performing a confocal microscopy study on colloids with diameters above the diffraction limit to understand how the feature size of the colloid-rich phase scales with the colloid diameter. Small angle x-ray scattering measurements and x-ray tomography are also planned to give information about the length-scales and degree of periodicity present in the gel branches. Both x-ray experiments are scheduled to be performed at the European synchrotron facility in Grenoble this fall.

## 5 Colloids, viruses and batteries

So far, this thesis has focused on the DNA-mediated self-assembly of spherical colloids made from a single material. This chapter explores how colloidal interactions can be used to assemble particles with non-spherical shapes and more than one material using both DNA and covalent bonds. The assembly of non-spherical objects leads to the formation gels with morphologies different than those accessible using only spherical colloids, while the formation of composites opens the possibility for materials with enhanced properties.

First, gels made from two very different classes of materials are used to demonstrate this concept, gold nanoparticles and viruses. Despite the obvious differences between metallic and biological matter, they both behave as colloids in solution, are subject to the same set of forces and can be assembled using DNA-mediated interactions. The viruses are functionalized with DNA grafted to their protein shell and interact with the complementary DNA attached to gold nanoparticles. The microstructure and the formation kinetics of the gold-virus composites are studied in detail using the fluorescent microscopy and image analysis techniques. The microporosity of these gels is increased compared to that of gels containing only gold nanoparticles and can be attributed to morphology of the constituent colloids. The gold-virus system is interesting from a fundamental perspective and there may be biotechnology applications for binding viruses to metallic structures.

The concept of using colloids with very different aspect ratios and constituent materials to form porous structures is used as inspiration for the assembly of silicon nanoparticles and carbon nanotubes to form a composite battery anode in the second part of this chapter. The incorporation of both an electrochemically active and a conductive component into an electrode is a common strategy for improving battery performance. The porous, composite material is a possible approach for addressing some of the key challenges for in silicon electrodes; namely silicon's high-volume expansion and the formation of an insulating polymeric species around the silicon nanoparticles upon lithiation. In this demonstration, covalent bonds are substituted for DNA bonds to join the silicon nanoparticles to the carbon nanotubes to design less costly and scalable systems.

### 5.1 Structural Studies in Gold Nanoparticle Virus Composite Gels

Rod-like viruses, such as the fd, M13, and Tobacco Mosaic viruses, are commonly used in soft matter physics as colloids, rather than for their biological function.<sup>10, 133</sup> In the lab, these

viruses can be produced at scale with precise dimensions due to the deterministic, biological origin of their shape. The viruses infect their hosts, either bacteria or plants, using the host's cellular machinery to self-replicate into millions of identical copies of high aspect ratio structures. To date, such high aspect ratio (of approximately 100:1) structures have been experimentally challenging to produce through solvothermal synthetic routes, which typically rely on limiting the growth of spherical seeds certain directions. The fd-virus used here consists of a coil of ssDNA encapsulated by approximately 2700 gp8 proteins with exposed amine groups, which are used to graft DNA to the virus.<sup>134</sup>

The DNA-functionalized fd-viruses are then mixed with 50nm gold nanoparticles functionalized with complementary DNA. A cartoon of the virus-gold composite formed using can be seen in Figure 57. The DNA on the gold nanoparticles and viruses are complementary such that the gold nanoparticles can bind to viruses, but the viruses cannot bind to other viruses and the gold nanoparticles cannot bind to other gold nanoparticles. The length of the viruses is an order of magnitude larger than the diameter of the gold colloids, allowing for multiple gold spheres to bind to a single virus. Therefore, the gold spheres can be considered a linker species connecting the viruses which form the backbone of the gels. The difference in aspect ratios between the gold spheres (50 nm diameter) and cylindrical viruses (8 nm diameter, 880 nm long) leads to porous gels with a morphology that can be tuned by altering the ratio of gold colloids to viruses in a sample.

The fd-viruses were functionalized using a two-step process, similar to the procedure used to functionalize silica nanoparticles in section 4.1 (Figure 58).<sup>10</sup> First, sulfo-SMCC was

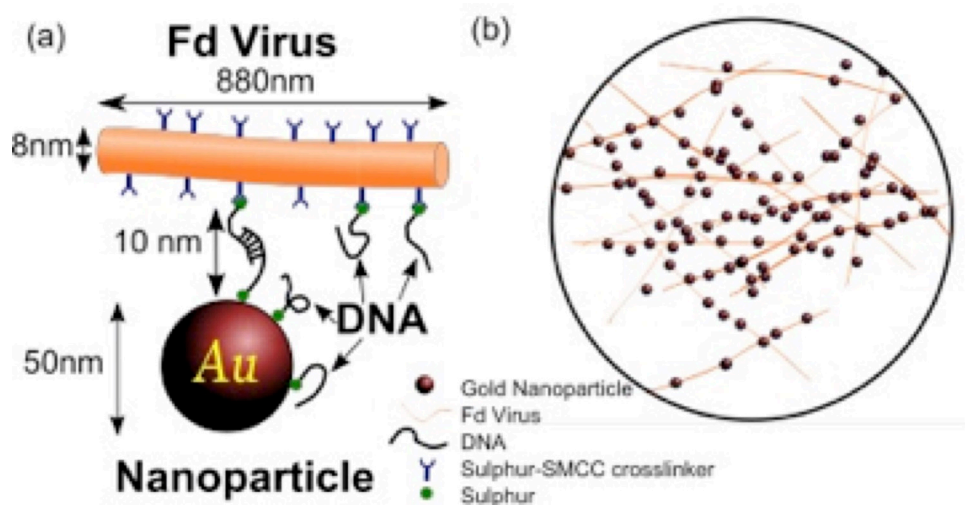


Figure 57: Cartoon depicting the DNA mediated interaction between gold nanoparticles and fd-viruses (a). Cartoon of the gold-virus gel network (b).<sup>8</sup>

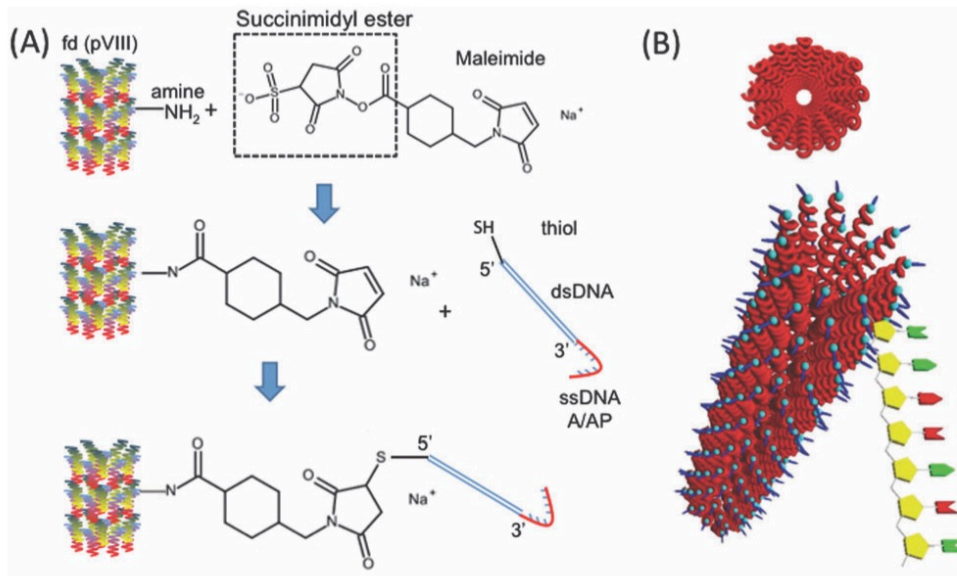


Figure 58: Cartoon of DNA-functionalization of fd-viruses with DNA using sulfo-SMCC (A). 3D representation of the fd-virus (B). Figure from Unwin et. al.<sup>10</sup>

reacted with the amine groups of the gp8 protein to introduce a thiol-reactive group. The functionalized viruses then were desalted using spin columns to remove the excess cross-linking reagent. The viruses with the maleimide functionality were reacted with thiolated-DNA that had been activated using DTT and the DNA-functionalized viruses were dialyzed to yield the final product. The grafting density of DNA was measured to be approximately 160 strands per virus by comparing the UV absorption of DNA-functionalized viruses to the sulfo-SMCC functionalized viruses.

The DNA-mediated gels were then prepared by mixing gold nanoparticles with viruses in number ratios ( $R_{GV}$ ) of 2, 5, and 10 to 1 with a fixed volume fraction of gold colloids ( $\phi = 0.1\%$ ) in 10mM Tris-EDTA buffer (tris(hydroxymethyl)aminomethane and ethylenediaminetetraacetic acid) and 50 mM NaCl. The colloidal gels were imaged using fluorescent microscopy with the gold nanoparticles acting as a negative contrast agent against the fluorescent background of the solvent (fluorescein salt). Images of a sample in the gas phase and as prepared and homogenized gels can be seen in Figure 59. Below each micrograph is the structure factor calculated from a series of images. Before homogenization, the gel morphology is more open and has a wider distribution of the pore size on the micron scale, which is reflected in the broad peak in  $S(q)$ . After homogenizing the gel for 30 minutes above the melt temperature and then quenching it, the colloids rearrange to form a more

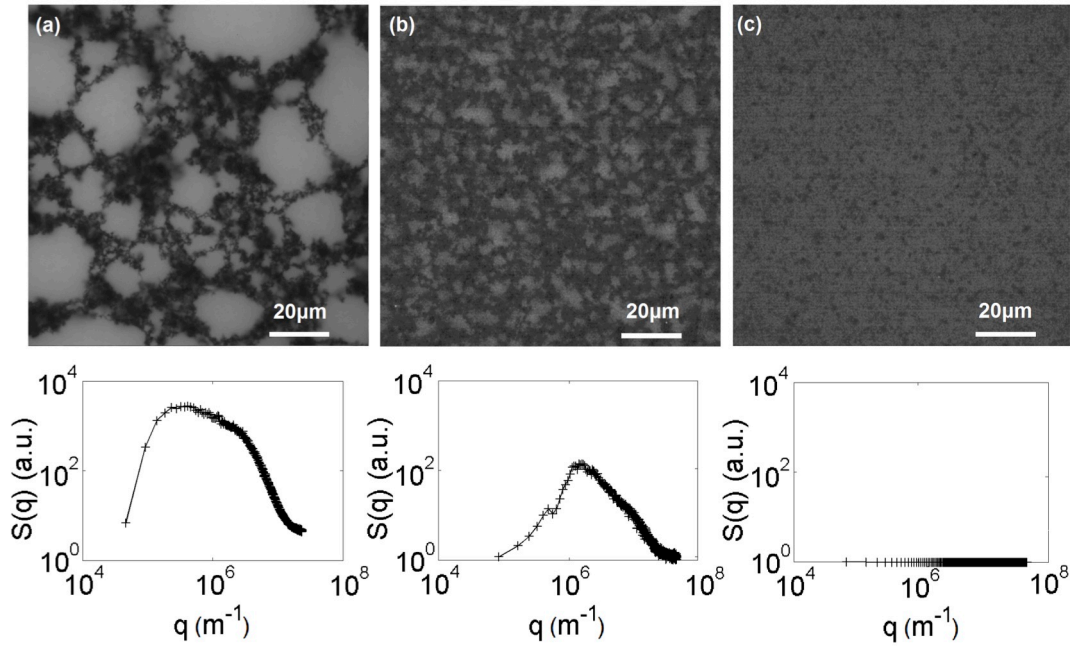


Figure 59: Fluorescence microscopy and structure factor analysis of gold-NP composites before homogenization (a), after homogenization (b) and above the melt temperature.

uniform and fine-stranded structure leading to a narrower peak in  $S(q)$ . The gold-virus aggregates sedimented to form a thin film of composite material at the bottom of the sample chamber. Samples heated to the gas phase appear speckled and have a flat  $S(q)$  across all wave vectors.

To study the kinetics of gel formation, dispersions of gold nanoparticles and viruses were quenched from the gas phase to four different temperatures below the melt temperature. Every twenty seconds, microscopy images were taken of the sample and the  $S(q)$  of the images was calculated. A plot summarizing the time evolution of the gel structure factor can be seen in Figure 60a. As the gel morphology evolves over time, the shape of  $S(q)$  remains the same and the magnitude of  $S(q)$  at each wave vector increases proportionally. The position,  $q_{max}$ , of the  $S_{max}(q)$  remains at a constant wavenumber as the intensity of  $S(q)$  increases. Therefore, as more of the sample is converted from the gas to the gel phase, the morphology of the gel structure remains similar and the gel does not coarsen.

The presence of a preferred wave vector,  $q_{max}$ , is indicative of spinodal decomposition as the gel formation mechanism.<sup>25, 135</sup> A constant  $q_{max}$  with time shows that subsequent coarsening of the gel is arrested after the initial phase separation. This result is due to the high energy of the DNA interaction. The collective binding energy of the DNA oligomers is on the order of tens of  $k_B T$  and is activated over a narrow temperature transition of a few

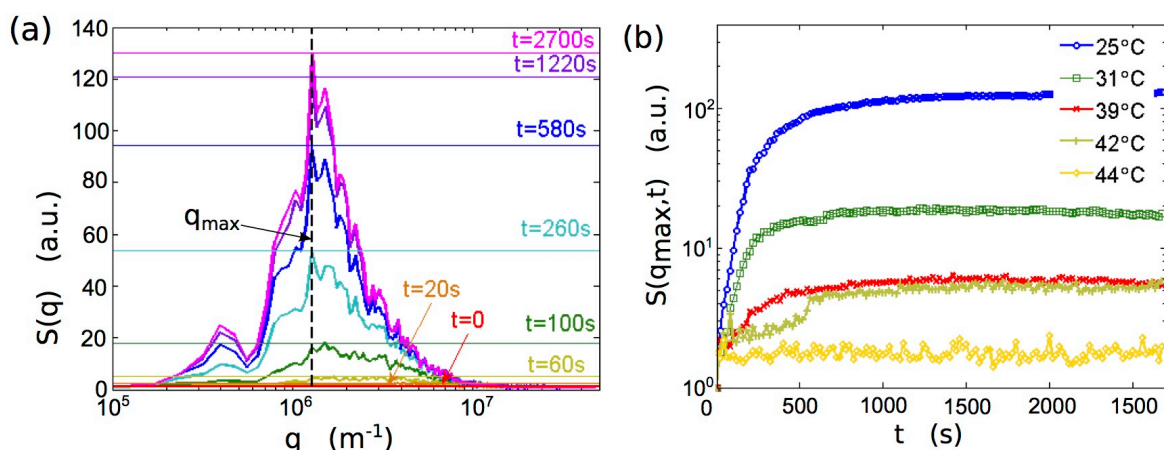


Figure 60: Time evolution of the structure factor for a gold-virus sample with a  $R_{GV}=5$  quenched from 50 °C to room temperature (a). The position of the maximum of the structure factor stays constant at  $1.3 \times 10^6 \text{ m}^{-1}$  throughout. Plot of the maximum intensity of the structure factor as a function of time for different quench depths (b). The microscopy images were taken every 20 seconds as the structure evolves.

degrees.<sup>35, 136</sup> As a result, quenching the sample even a couple degrees below the melt temperature is sufficient to suppress most colloidal rearrangement, fixing the position of  $q_{max}$ .

Since  $q_{max}$  remains constant during gel formation, the time-evolution of the magnitude of  $S(q_{max})$  can be used to follow the gelation kinetics at the different quench depths (Figure 60b).  $S(q_{max})$  increases quickly, before reaching an asymptotic value after approximately 1000 seconds. The rate of gel formation is similar for all quench depths with the asymptotic value of  $S_{max}(q)$  increasing with lower quench temperatures. At lower temperatures, the contribution of entropic term to the colloid interaction potential will increase, lowering the Gibb's free energy of the system. Therefore, the increase in  $S_{max}(q)$  with quench depth shows that tuning the interaction potential between colloids can control the gel morphology. Here, the distribution of length-scales in the gel is narrowed by increasing the attraction potential between the viruses and gold nanoparticles.

Chord analysis allows for measurement of length-scales of the gel aggregates ( $\lambda_a$ ) and the gel pores ( $\lambda_p$ ) independently, providing complementary information to  $S(q)$ . For the samples quenched to 25 °C and 39 °C, chord analysis was performed at two time intervals during gel formation; after 400 seconds where the gel was evolving and at 1200 seconds where the final gel structure had formed. At both quench temperatures and times, the chord analysis showed that the gels had similar values for both  $\lambda_a$  and  $\lambda_p$ . The similar length-scales in the samples at the highest and lowest quench temperatures suggests that the DNA hybridization energy rather than the entropic energy determines the most prevalent length-scales in the gel.

Sample	Time (s)	$\lambda_a$ ( $\mu\text{m}$ )		$\lambda_p$ ( $\mu\text{m}$ )
		short $\lambda_a$	long $\lambda_a$	
$R_{GV}$				
2	400	0.37	4.03	4.09
5	400	0.42	3.20	3.75
10	400	0.36	3.76	2.68
Control	400	-	1.95	3.19
2	1200	0.41	4.41	4.74
5	1200	0.39	4.09	3.02
10	1200	0.27	5.25	2.53
control	1200	-	5.18	3.89

Figure 61: Table summarizing the results of the chord analysis on gold-virus gels with ratios  $R_{GV}$  of 2, 5, 10 and a control sample with only gold nanoparticles. The length-scales of the aggregated ( $\lambda_a$ ) and pores ( $\lambda_p$ ) phases of the gel structure were calculated at 400 and 1200 seconds after quenching the samples from 50 °C to room temperature. Gels aggregates have both a short and a long  $\lambda_a$  which is not present in the control sample.

The histogram of the measured chord distribution in the confocal images for the gold-virus aggregates was best fit using two values for  $\lambda_a$ , one for shorter chords and one for longer chords. This result differs from the gold-gold, control gel (spheres only), which can be well-fit using only one value for  $\lambda_a$ . The two fit values for  $\lambda_a$  support that there are two different length-scales of gel branches in the gold-virus system, one at shorter length-scales and one at longer length-scales. In all  $R_{GV}$  ratios and times after quenching, the shorter length-scale of the aggregates ( $\lambda_a$ ) is at the diffraction limit of the optical microscopy set-up ( $d[x, y] \approx 350 \text{ nm}$ ,  $\text{NA} = .7$ ). Although the value of the shorter  $\lambda_a$  cannot be determined more precisely, it is possible to infer some information from that the length-scale is less than 350 nm and roughly one third of the contour length of the virus. If it is assumed that the viruses are acting as rigid, rod-like structural elements with the gold nanoparticles binding along their surfaces, the shorter  $\lambda_a$  may correspond to the diameter of the gel branches linked along the long axis of the viruses by gold nanoparticles. Viruses bound perpendicular to each other would support a length-scale at least as long as the virus. Since the viruses are semi-flexible, they may also bend to form features at the shorter length-scale, although there is an energetic cost of bending. A complementary technique, such as in-situ SEM or small angle x-ray scattering would be necessary to resolve the nanoscale features more accurately. The absence of the shorter length-scale in the gold-gold gels supports that this feature is a direct result of the gold-virus interactions. The longer value for  $\lambda_a$  is similar to the values observed

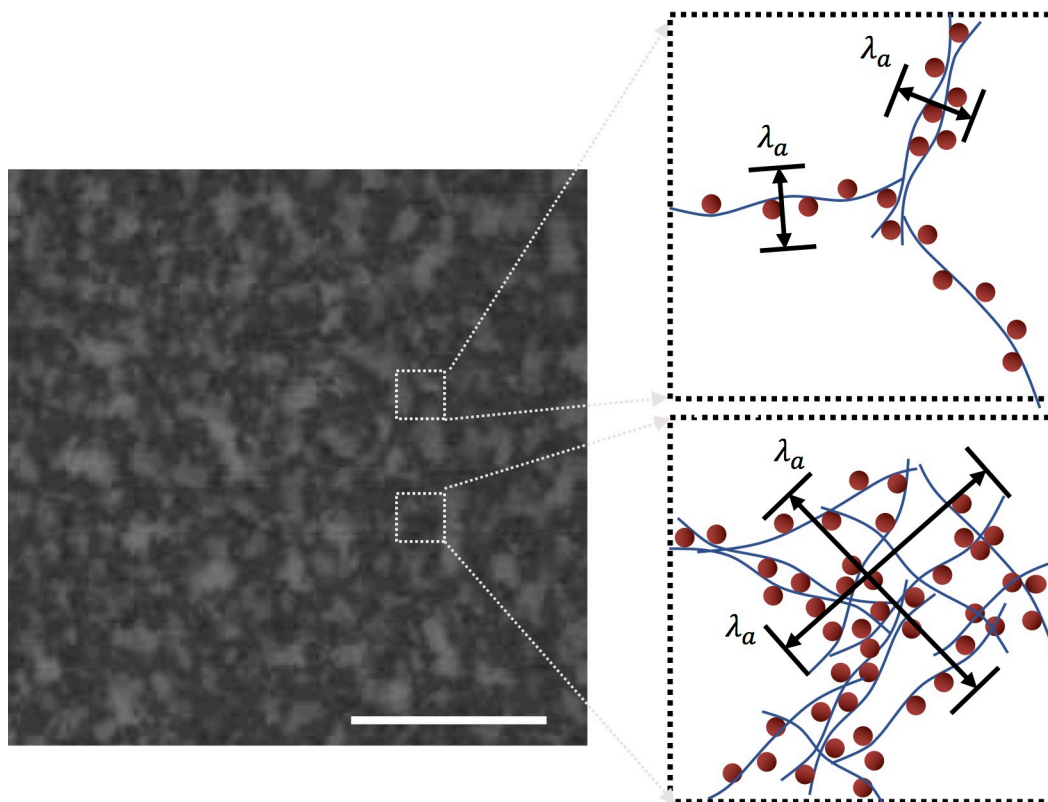


Figure 62: Enlarged micrograph of homogenized gel in Figure 59 (left), scale bar is  $20\mu\text{m}$ . Cartoon showing possible morphologies of aggregates spanning the width of the gel branches consisting of viruses (blue) and gold nanoparticles (red) leading to the short  $\lambda_a$  length-scale (top right). Cartoon showing possible morphologies of gel aggregates leading to the longer  $\lambda_a$  (top right).

in the gold-gold gel, suggesting a similar morphology. Cartoon representations of possible gel structures that would correspond to the shorter and longer  $\lambda_a$  are shown in Figure 62.

At the longer length-scale,  $\lambda_a$  has similar values for all  $R_{GV}$  values, while  $\lambda_p$  decreases with increasing  $R_{GV}$ . Lower  $R_{GV}$  values correspond to more viruses in the gel ( $\phi$  of the gold nanoparticles is constant). The decreased porosity with the increased viruses supports that the gold nanoparticles are acting as linkers or nodes for the virus network. As the number of viruses in the gel increases, the same number of gold nanoparticles are spread out through a greater volume leading to a decrease in the gel microporosity.

The relatively small volume fraction of colloids in this system led to the formation of a thin film of the gold-virus composite. By changing the ratio of rods to spheres, the morphology of the composite film was tuned, highlighting the opportunity for controlling the gel structure through the geometry of the colloidal building blocks. This concept can be extended to using colloids of various shapes, aspect-ratios and sizes. In the next section, composite materials made from silicon nanoparticles and carbon nanotubes will be presented, which was inspired in part by this the gold-virus gels.

## 5.2 Self-assembly of silicon nanoparticle and carbon nanotubes

Colloidal self-assembly has potential advantages over conventional planar processing for improving the performance of battery electrodes. As discussed in section 3.5, colloidal self-assembly can be used to form porous electrodes with large surface areas, leading to improved ionic transport through the electrolyte and at the electrolyte/electrode interface. These porous three-dimensional structures may allow for the formation of thicker electrodes with both higher power and energy densities than those accessible using conventional approaches. In principle, they can be designed to self-assemble with specific binding rules such that the conductive component (carbon particles) and the electrochemical component of an electrode are in intimate contact. Here as a first step towards achieving this ambitious goal, colloidal self-assembly is used to synthesize silicon anodes, which are one of the most promising and challenging anode materials currently under development.

Silicon is a heavily researched material for rechargeable lithium ion batteries primarily because silicon anodes have a nearly ten times higher specific capacity than state of the art carbon-based anodes (3578 v. 372 mA h g<sup>-1</sup>).<sup>137, 138</sup> Upon full lithiation, silicon forms a lithium rich silicide and undergoes a 300% volume expansion to accommodate 15 lithium atoms per 4 silicon atoms.



The volume expansion puts both the particles themselves and the interface with their surrounding materials under enormous stresses. Upon cycling, any silicon particles over approximately 100 nm will pulverize into smaller fragments.<sup>139</sup> This challenge is typically addressed by using silicon nanoparticles or nanowires,<sup>140</sup> which can better accommodate the cyclic stresses.

The interface between the silicon particles with both the liquid electrolyte and its conductive component presents a more challenging problem. Upon lithiation, an anode's potential (referenced to lithium) decreases and the electrolyte decomposes to form a solid electrolyte interphase (SEI) at surface of the anode.<sup>138, 141</sup> As the SEI layer grows, it forms an ionically conductive but electronically insulating, protective layer around the anode and prevents further degradation of the electrolyte. In graphitic systems, the result is an insulating layer approximately 10 nm thick that is stable under cycling. However, in silicon

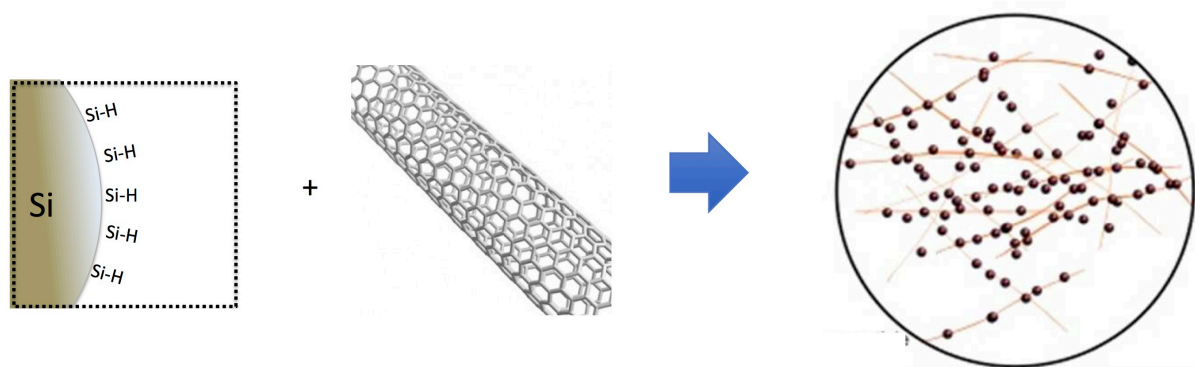


Figure 63: Cartoon diagram of concept to form a porous network of silicon nanoparticles and MW-CNTs.

anodes the SEI layer cracks under the cyclic mechanical stress exposing fresh surfaces to the electrolyte and leading to further SEI growth.<sup>138, 141</sup> The uncontrolled growth of SEI has been shown to be a primary mechanism for capacity loss in silicon anodes.<sup>138</sup>

The other consequence of continuous SEI growth is that the silicon particles lose contact with the surrounding conductive carbon particles, electronically isolating the silicon from the circuit. Maintaining good electrical contact between the electrochemically active silicon particles and the carbon particles remains a key challenge for both improving the performance of silicon anodes and studying the mechanisms contributing to SEI formation. There are currently numerous strategies under investigation to address both SEI growth and loss of electrical contact including the carbonization of the silicon particles<sup>142</sup> and the use of electronically conductive binders<sup>143</sup>.

Forming a flexible three-dimensional porous network of silicon nanoparticles connected with a conductive element such as carbon nanotubes is a possible solution for overcoming the challenges of silicon particles' large volume expansion upon lithiation (Figure 63). The free-volume in the porous structure can provide space for particle expansion upon lithiation and the specific interactions of self-assembly can ensure that the silicon particles remain in good electronic contact with the carbon nanotubes. Furthermore, the conductive backbone of the carbon nanotube network can allow for a low resistive path through the electrode. As the silicon particles expand and contract, the carbon nanotubes can ensure that the silicon particles remained "wired-up". Such an optimized composite material can enable the study of SEI formation without concern for loss of electrical contact between the silicon

particles and the external circuit. A “binder-free” electrode simplifies the analysis of the SEI formation and allows for failure modes to be more easily isolated.

Since the formation of reversible bonds between the CNTs and the silicon nanoparticles is not needed, DNA oligomers were replaced with covalent bonds to link two materials. Covalent bonds are expected to be more robust under electrochemical cycling. Moreover, although the cost of DNA has decreased significantly, making bonds with DNA remains more expensive. Since dense brushes of DNA lead to attraction energies on the order of tens of  $k_B T$ , the DNACCs do not rearrange upon quenching below the melt temperature and covalent bonds formed under an external stimulus, such as UV light, should behave in a similar manner to DNA-mediated interactions activated by temperature. Therefore, if both the silicon and CNTs can be engineered to be well-dispersed in the same solvent with complementary surface groups, they could be driven from the dispersed to the gel phase by activating the covalent bonds.

### 5.2.1 Functionalization of carbon nanotubes

Carbon nanotubes must be either chemically modified or mixed with surfactants to disperse in significant concentrations in solvents.<sup>144</sup> Therefore, a chemical modification route was needed to both increase the dispersibility of the CNTs and introduce a functional group for subsequent reactions. A diazonium coupling reaction was identified that could attach anilines derivatives to the surface on the CNTs and disperse the CNTs in organic solvents. A control reaction was also performed without adding the aniline to the mixture.

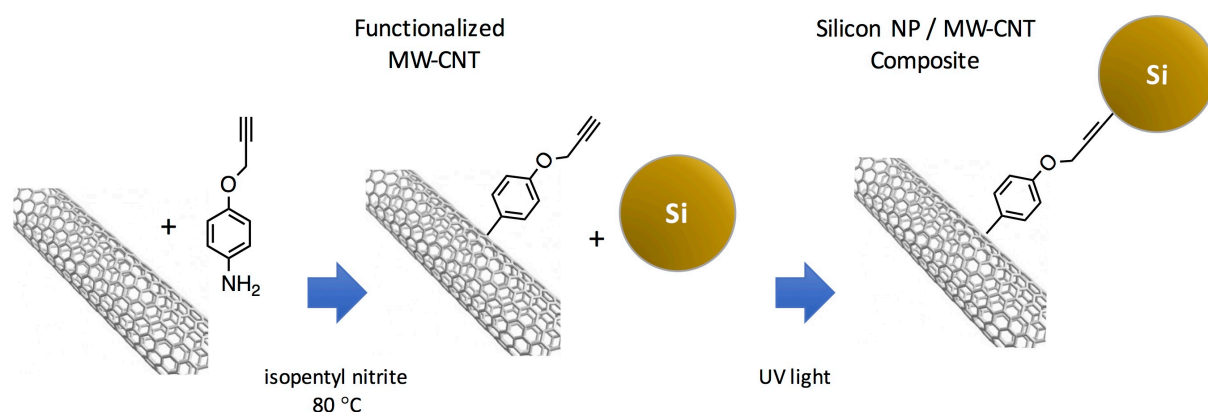


Figure 64: Diagram of two-step process to chemically bond silicon nanoparticles to MW-CNT. In the first set, the MW-CNT are functionalized with an alkyne group using a diazonium reaction. In the second step, the functionalized MW-CNT are attached to the silicon nanoparticles using a hydrosilylation reaction.

After the reaction, there was a clear change in the dispersion properties of the modified carbon nanotubes in DMF compared to the reaction without the aniline (Figure 65). The CNTs reacted without the aniline clumped together and sedimented to the bottom of the glass vial, while the samples reacted with the aniline formed a dark dispersion that remained in solution indefinitely, even when accelerated at the maximum speed of the centrifuge (8,000 G). To wash the excess reagents from the CNT dispersion reacted with the aniline, samples needed to be either dialyzed or mixed with anti-dispersants to precipitate the CNTs from the solvent mixture.

To characterize the organic modification of the CNTs, both ATR and transmission FTIR spectroscopy were performed on the samples. Alkyne groups have vibrational signatures at both  $2100\text{-}2200\text{ cm}^{-1}$  (C-C) and  $3000\text{-}31000\text{ cm}^{-1}$  (C-H). These resonances have been observed in single-walled nanotubes (SW-CNTs) modified using the reaction route used here.<sup>145</sup> However, the alkyne stretches were not detectable in MW-CNT samples here, which may be due to the higher surface to bulk carbon ratio in MW-CNTs (10-20 layers) than in SW-CNTs. The strong broad-band IR absorption of the CNTs swamped any signal in the ATR-FTIR using a diamond tip. Germanium tips, which have a shorter penetration depth into the sample than diamond tips, may enable measurement of the IR absorption, but one was not available. The MW-CNTs also were embedded in KBr pellets to measure the IR absorption in transmission, but the measurement could not be optimized to observe an alkyne signature in this

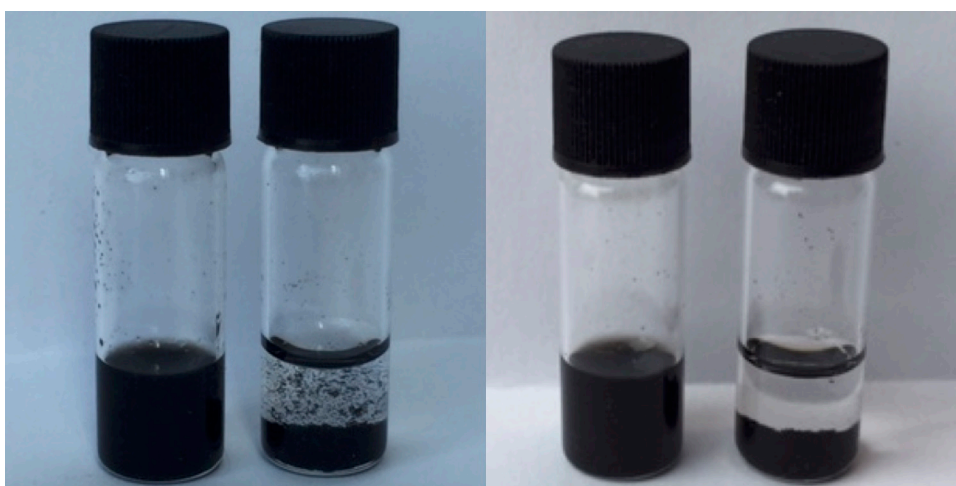


Figure 65: Photograph showing dispersion properties of carbon nanotubes in DMF reacted with and without the aniline. The samples were vortexed for 1 minutes and photographs were taken after 10 minutes (left) and 3 hours (right). In each photograph, the sample reacted with the aniline is on the left and the one without is on the right.

configuration either as the pellet introduced too many impurities to resolve such a weak signal.

The modification of CNTs is often characterized using Raman spectroscopy through the relative strength of the G (graphic) and D (defect) bands, which are measures of the  $sp^2$  and  $sp^3$  bonding present in carbons.<sup>145-147</sup> When the aromaticity of the CNTs is altered through chemical modification, the strength of the D band ( $1320\text{ cm}^{-1}$ ) will increase at the expense of the G band ( $1580\text{ cm}^{-1}$ ). Raman spectroscopy showed a reduction in the D/G band ratio between the unmodified and modified CNTs (Figure 66). However, sonication of the CNTs also changed the D/G ratio, so it was not possible to separate the effect of sonication from the effect of chemical modification with confidence. It may be possible to separate the effect by carefully controlling the sonication dose or omitting the sonication step altogether. Sonication has been shown to cleave carbon nanotubes into shorter fragments and introduce additional defects.<sup>148</sup>

Although Raman spectroscopy is more sensitive than IR absorption spectroscopy for measuring the presence of alkyne groups, to our knowledge Raman measurements of alkyne functionalities have not been reported on carbon nanotubes even in studies of nominally functionalized carbon nanotubes.<sup>145, 149, 150</sup> It was observed that the power density sufficient to make a Raman measurement with a good signal to noise ratio noticeably altered the

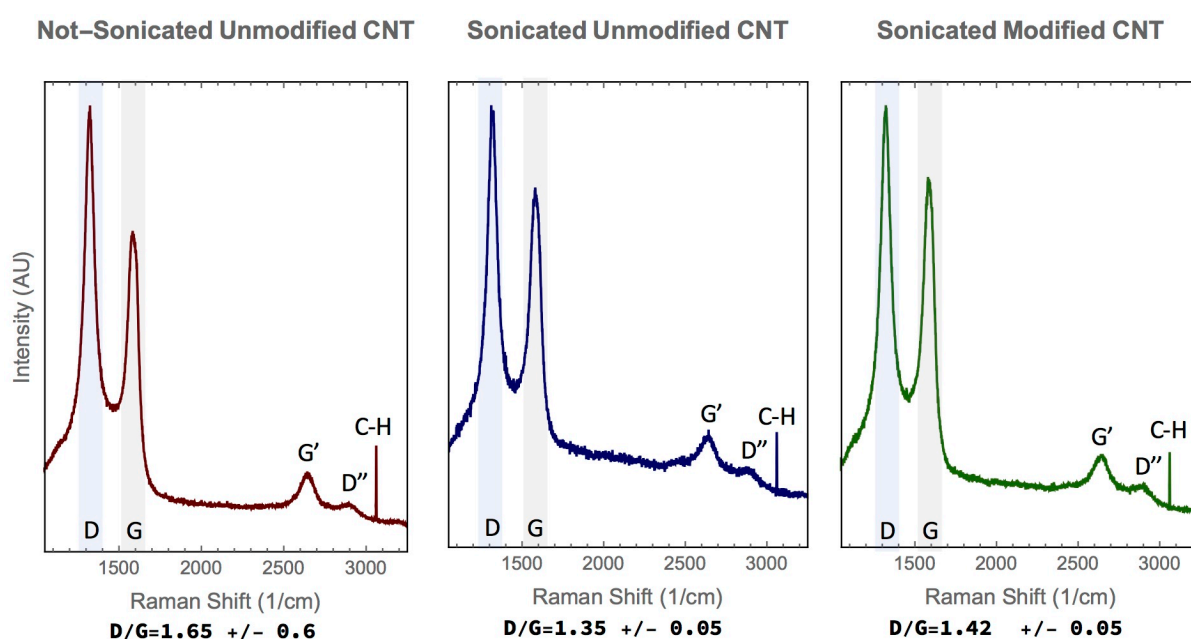


Figure 66: Raman spectra of unmodified, sonicated and sonicated and modified MW-CNTs with the key bands highlighted. The ratio of D/G band is below each example spectra.

samples. The organic groups may be thermally removed from the nanotube surface at the power density necessary for the Raman measurement. The C-H stretch ( $3065\text{ cm}^{-1}$ ) was observed in all the nanotube samples and therefore can be attributed to defects in the CNTs before modification.

There is strong evidence in the literature supporting the efficacy of the diazonium route to modify SW-CNTs and repeating the reaction on a SW-CNT substrate could give more confidence that the protocol was applied correctly. X-ray photoelectron spectroscopy (XPS) could also be used to test for the presence of the organic groups. A fluorescence assay based on an azide functionalized dye could probe for the presence of the alkyne groups using a copper catalyzed click reaction. Without additional experimental data, the change in dispersibility of the MW-CNT is the strongest evidence for successful modification. The change in dispersion properties can be attributed to the presence of the aniline, since the control sample without the aniline precludes the solvent or the initiator alone being sufficient for the change in dispersion.

### **5.2.2 Functionalization of silicon nanoparticles**

The chemical modification and characterization of the silicon nanoparticles is a less challenging problem. Silicon surfaces oxidize immediately when exposed to water or air forming Si-O and Si-O-H terminated surfaces. Chemical modification of silica surfaces using silanes and silane modified surfaces already has been discussed in section 4.1. However, rather than modifying the silicon particles using silanes, hydrosilylation, a direct functionalization route was pursued. In hydrosilylation reactions, hydrogen-terminated silicon surfaces can bind to alkyne or alkane groups to form Si-C bonds in the presence of radicals.<sup>151, 152</sup> The hydrosilylation route was chosen since it did not require additional chemical modification of the silicon surface and the reaction could be catalyzed by applying an external stimulus such as UV-light to the colloidal dispersion. Moreover, the absence of a silica intermediate layer between the silicon particles and the carbon nanotubes and SEI hopefully will simplify the later analysis. The reaction scheme between the alkyne functionality on the modified CNTs and the hydrogen-terminated silicon surface is shown in Figure 64.

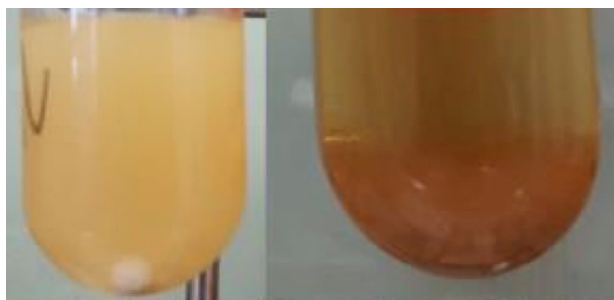


Figure 67: Photographs of the silicon nanoparticle, hexadecane/THF and aniline mixture reacted with out (left) and with (right) UV irradiation.

Since silicon nanoparticles are easily oxidized, most silicon particles used for anodes have a native oxide layer that is challenging to remove. However, it is possible to synthesize silicon nanoparticles solvothermally without a native oxide layer.<sup>153, 154</sup> A commercial vendor was identified (Meliorium Technologies) that could provide nominally 30 nm hydrogen-terminated silicon particles. The particles were provided in dry hexadecane and an argon atmosphere to prevent oxidation in transit and were stored in an argon filled glovebox prior to use.

The dispersibility of the hydrogen-terminated silicon nanoparticles in different solvents was tested by sonicating small volumes of the silicon/hexadecane stock solution in larger volumes of dry solvents with different polarities: toluene, hexadecane, tetrahydrofuran (THF), dichloromethane (DCM) and DMF. The nanoparticle-solvent samples were then examined after a period of time to see in which solvent the nanoparticles remained dispersed without any visible solid/liquid phase separation or aggregation. THF was found to be the best solvent for dispersing the nanoparticles. Dilute samples of the silicon/solvent samples were also measured using DLS. In all solvents, the nanoparticles showed at least some aggregates of approximately a few hundred nanometers in addition to the primary particles. Electron microscopy showed that the aggregates consist of primary particles that are tens of nanometers in diameter.

The hydrosilylation reaction between the hydrogen-terminated silicon nanoparticles and the alkyne groups on the aniline compound was probed first without the carbon nanotube substrate. The silicon nanoparticles were dispersed in THF and sonicated to form a stable dispersion. The aniline and the silicon, dispersed hexadecane/THF mixture, were reacted in a quartz conical flask under UV illumination to catalyze the reaction. A control sample without UV light was also prepared and after the reaction both solutions were allowed to stand for a period of time. Figure 67 shows the decrease in dispersibility of the silicon

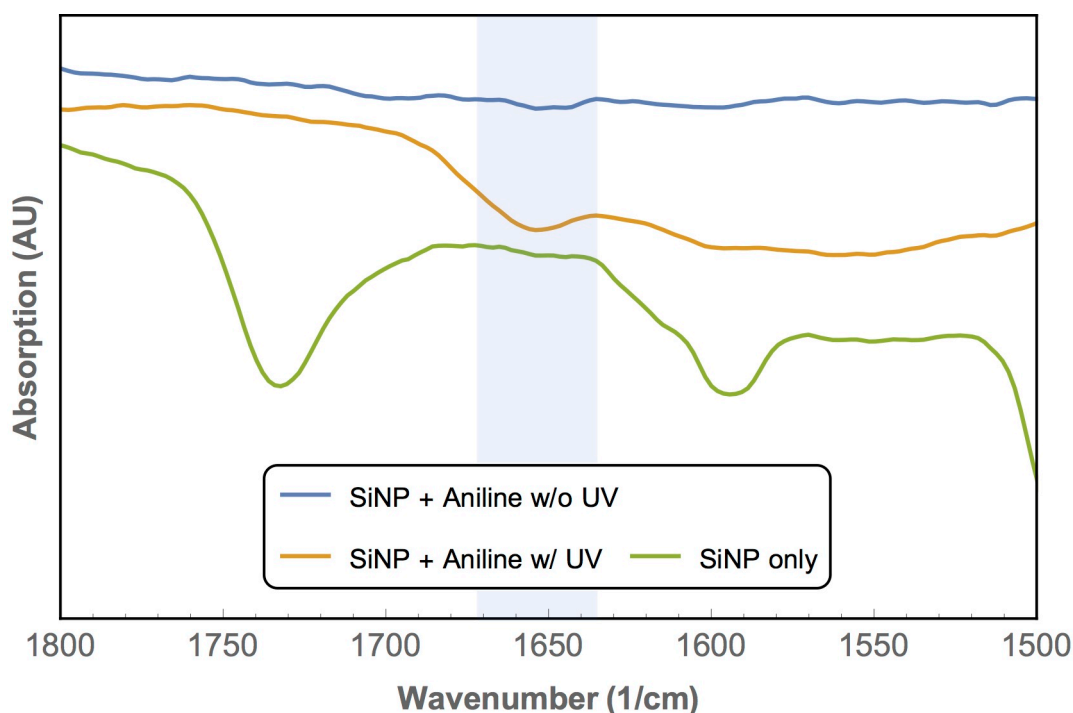


Figure 68: FTIR absorption spectrum of silicon reacted with the alkyne-aniline with and without UV irradiation and the silicon nanoparticle. The C=C ( $1650\text{ cm}^{-1}$ ) absorption band is highlighted for clarity.

nanoparticles after reacting under UV radiation, while the nanoparticles in the sample without UV radiation stayed dispersed. The reduced dispersibility is likely due to the introduction of more polar groups to the nanoparticle surface.

The samples then were washed in a glass centrifuge tube under nitrogen to remove the hexadecane and excess aniline. The IR spectra of the silicon nanoparticles were measured using an ATR-FTIR instrument in an argon filled glovebox. The absorption spectra of silicon nanoparticles reacted with UV light, without UV light and those simply washed in hexane to remove the hexadecane were compared (Figure 68). An increased absorption was observed at  $1650\text{ cm}^{-1}$  in the sample reacted under UV irradiation. Absorption in this band shows the presence of C=C bonds, supporting that there was a conversion of the alkyne groups to alkane groups upon hydrosilylation.<sup>151</sup> Si-C bonds were difficult to observe directly in FTIR, since they are in the figure print region and overlap with Si-O vibrations. The silicon nanoparticles themselves show two additional absorption peaks at  $1730\text{ cm}^{-1}$  and  $1590\text{ cm}^{-1}$  that are likely from contamination that leached from the polystyrene centrifuge tubes used to wash the unreacted sample.

### 5.2.3 Silicon-carbon nanotube composite formation

Since there was some direct and indirect evidence of successful attachment of the aniline to both silicon nanoparticles and carbon nanotubes, the alkyne functionalized carbon nanotubes were reacted with the silicon nanoparticle to form the composite material. THF was added to unmodified silicon nanoparticles and sonicated. The THF/hexadecane/silicon nanoparticle mixture was mixed with the modified carbon nanotubes in DCM in a conical quartz flask and irradiated with UV light (1:1 by solvent volume, 5:1 by mass of silicon to CNTs). After irradiation for 30 minutes, the solid material was washed in hexane in a nitrogen atmosphere to remove any residual hexadecane. The composite material did not disperse in hexane and had the appearance of low density, fluffy material with a uniform color (Figure 69). The composite material was then dried under a flow of nitrogen and stored for later use. Since the composite material consisted of carbon nanotubes cross-linked with silicon nanoparticles using covalently bonds, it can be expected to be mechanically robust and to be dried without collapsing the structure due to capillary forces.

Transmission electron microscopy was performed to study the morphology of the composite material (Figure 70). The composite was stable under the electron beam and could be studied in detail. As expected from the DLS measurement, the silicon nanoparticles are in agglomerates as well as isolated particles. Nonetheless, the silicon nanoparticles are dispersed throughout the carbon matrix. The layers of the carbon nanotubes are also clearly visible and a clear diffraction pattern from the silicon nanoparticles was observed showing that they are crystalline. The silicon nanoparticles are in close contact with the carbon nanotubes and some of the carbon nanotubes are wrapped around the surface of the silicon



Figure 69: Photograph of silicon nanoparticle, carbon nanotube composite material in hexane.

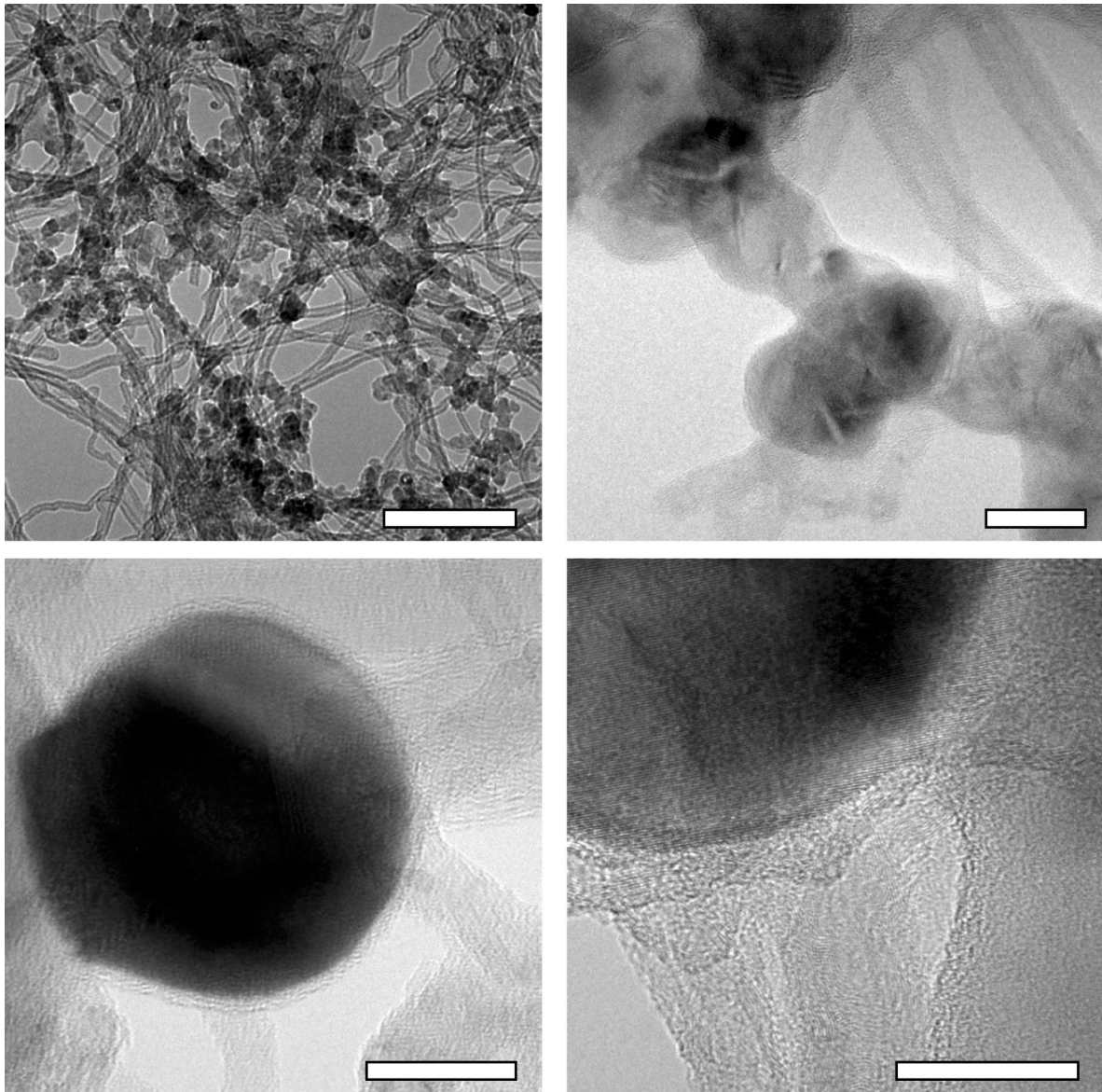


Figure 70: TEM micrographs of silicon nanoparticle composites. Scale bar on top left is 100 nm and all others are 20 nm.

nanoparticles. There appears to be a direct transition of morphologies between the crystallinity of the silicon nanoparticles and the layer spacing of the carbon nanotubes without a disordered region in between. The absence of a disordered region suggests that the silicon nanoparticles did not undergo significant oxidation. Oxidation before the reaction between the silicon nanoparticles with the carbon nanotubes would prevent the hydrosilylation.

## 5.2.4 Electrochemical measurements of silicon-carbon nanotube composite

The TEM evidence of the close physical contact between the silicon nanoparticles and the carbon nanotubes led to the electrochemical testing of the composite material. To establish a baseline, half-cells consisting of a physical mixture of silicon nanoparticles and non-modified carbon nanotubes were cycled against a disc of metallic lithium. The physical mixture was prepared by mixing dry solutions of CNT in DCM and silicon nanoparticles in THF/hexadecane in a 5:1 by ratio (by of the solid mass) in a conical flask. The composite was then washed using a 1:1 mixture of THF:DCM to remove the residual hexadecane and to obtain a solution of the resultant material. The solution of the material was then “drop-casted” by pipetting the solution onto a stainless-steel disc and letting the solvent mixture evaporate. The composite thin film was well-adhered to the stainless-steel disc and was assembled into coin cells with a glass separator, LP30 electrolyte and the lithium disc cathode as described in section 2.3.4.

The half-cell was lithiated at a constant current at a rate such that it would take 75 hours to fully lithiated the anode based of the gravimetric capacity of silicon (C/75) and can be seen in Figure 71. The electrochemical behavior of the material upon lithiation is consistent with what has been observed in silicon anodes.<sup>137, 138, 141</sup> At approximately 0.8 V, there is a plateau showing the onset of SEI formation. Only once the SEI sufficiently passivates

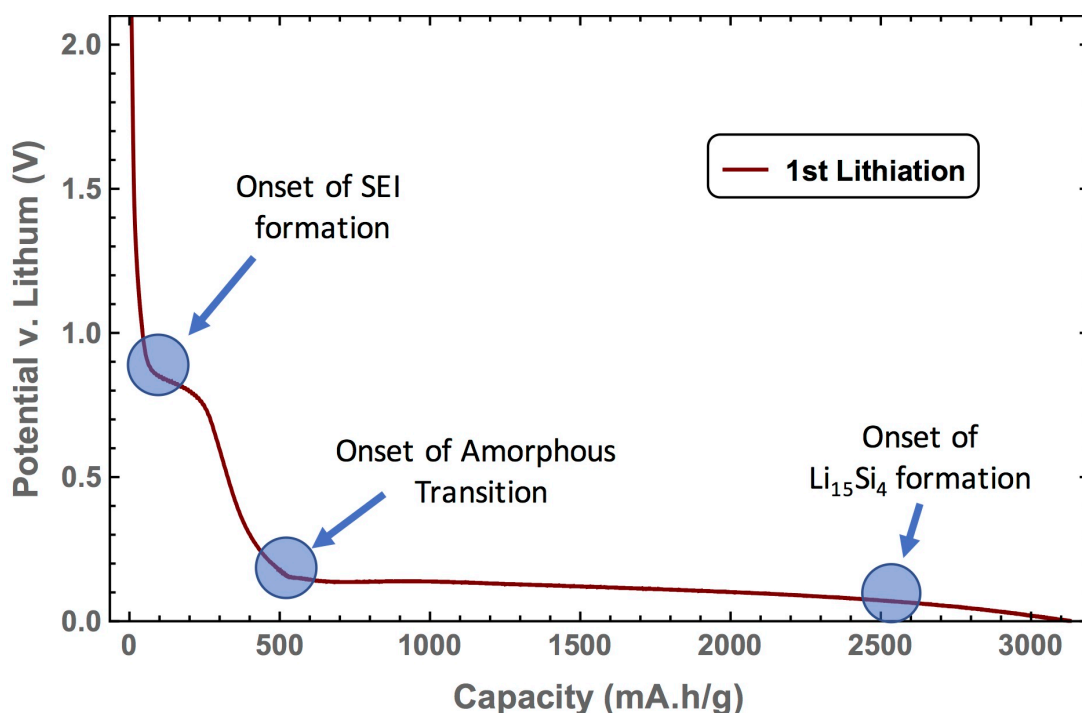


Figure 71: Electrochemistry of the initial lithiation of the physical mixture of silicon nanoparticle and carbon nanotube in a half-cell. The onset of the SEI formation, the amorphous transition and formation of Li<sub>15</sub>Si<sub>4</sub> are highlighted for clarity.

the electrode does the potential again decrease. The next feature appears at approximately 0.2 V, which is the beginning of the crystal to amorphous transition in the silicon. At approximately 50 mV, the amorphous silicide transitions to  $\text{Li}_{15}\text{Si}_4$ , the fully lithiated phase. The capacity of the anode is approximately  $3200 \text{ mA h g}^{-1}$  and approaches the theoretical capacity of silicon within the measurement error. However, a portion of the current can be expected to contribute to the electrolyte degradation forming the SEI and therefore will be irreversible. The carbon nanotubes are not expected to contribute significantly to the capacity of the electrode due to the low mass (5:1) and carbon's low theoretical specific capacity with respect to silicon (~9:1).

Figure 72 shows the electrochemical behavior of the half-cell under cycling. As expected, during the first delithiation (charge), only approximately  $1900 \text{ mA h g}^{-1}$  of the capacity can be recovered. The capacity loss can be attributed to both the formation of SEI under lithiation and the loss of electrical contact with the silicon nanoparticles. Upon subsequent cycling the capacity of the anode quickly fades and less than 10% of the original capacity remains after 5 cycles.

The self-assembled silicon nanocomposite was also tested to see if it had improved the electrochemical performance over a simple physical mixture. Unfortunately, almost no

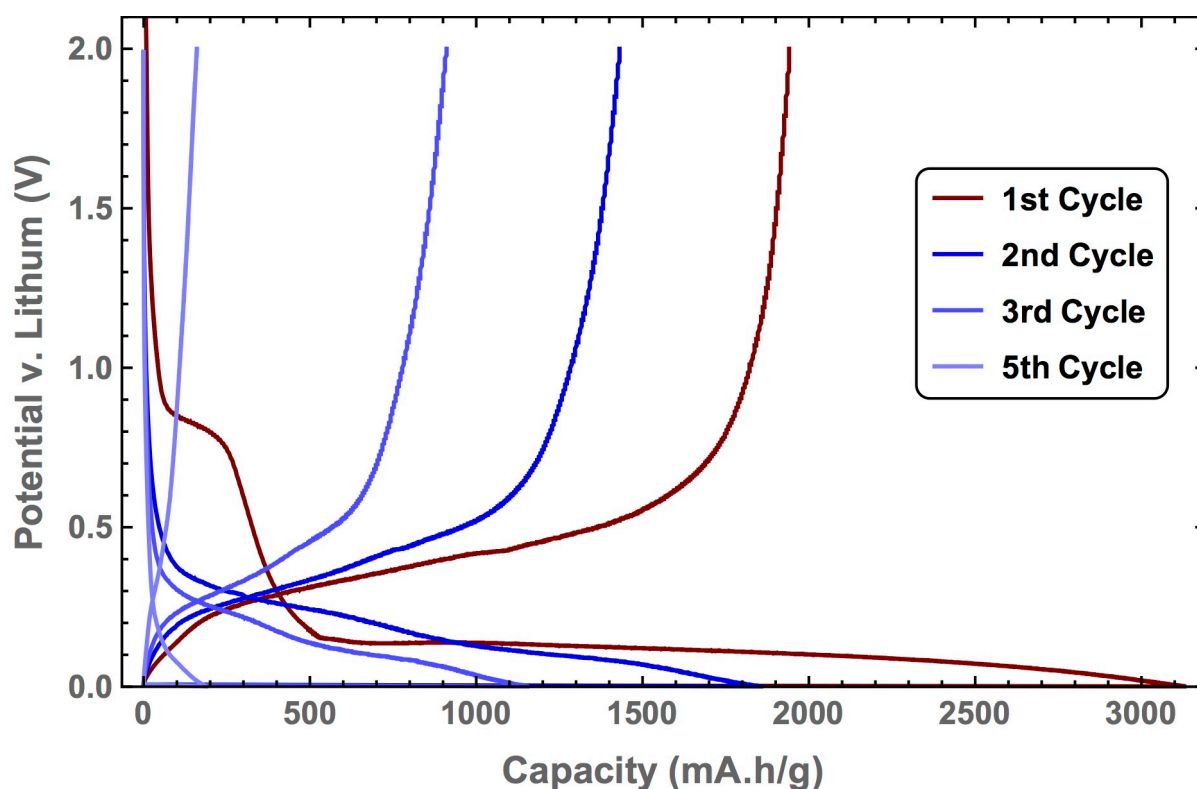


Figure 72: Electrochemistry of the physical mixture of silicon nanoparticle and carbon nanotube in a cycled in a half-cell.

capacity was measured in half-cells containing the self-assembled composite material as the electrode prepared by drop-casting. The material was examined under TEM and it was found that the composite was contaminated with polystyrene that had leached from the centrifuge tubes used to wash the composite after the reaction. Electrochemical testing is now being repeated using only glassware to prepare the composite material and should show if the improved dispersion of the silicon nanoparticles throughout the CNT matrix will lead to superior electrochemical performance and anodes approaching the theoretical capacity of the silicon nanoparticles upon lithiation.

Wiring up the nanoparticles alone likely will not be sufficient to prevent the capacity fade in silicon anode. The SEI layer can still be expected to grow continuously under cycling as the SEI cracks to expose fresh surfaces. To prevent continuous SEI formation, a strategy will be need to form a SEI that can withstand the mechanical stress of cycling. One potential strategy is to coat the silicon nanoparticles with a flexible polymeric species that mimics the dielectric and ionic conductivity properties of the SEI layer. Appendix 7.2 discusses hydrosilylation reactions to coat the silicon nanoparticles with such materials. Understanding and improving the properties of the SEI on silicon anodes is an ongoing area of research for our group as well as others. The composite electrode demonstrated here could be a good substrate for testing artificial SEI coatings.

## 6 Outlook

Colloidal self-assembly offers the opportunity to form macroscopic objects with short-range order having properties optimized for specific applications. This thesis explored using systems of gold, silica, silicon and carbon colloids for photonic, plasmonic and electrochemical applications. The example systems were chosen to take advantage of the specific properties of a given nanoparticle material. By carefully designing colloidal assemblies, in the future it may be possible to harness novel properties of nanoparticles that have not yet been exploited in devices.

One-component nanoparticle gels can be engineered to have porosity on the order of tens of nanometers to tens of microns. As was shown in this work, nanoparticle gels themselves can be used to demonstrate novel properties, such as structural color or used to make devices such as SERS substrates. However, the nanoparticle assemblies also can be used as templates; much how block copolymer and colloidal crystal templates have been used in research. However, for applications that require only short-range order, colloidal self-assembly offers a three-dimensional template with a greater range of feature sizes. Often, only short-range order is necessary for most optoelectronic, electrochemical and catalytic applications. Techniques such as solution or electrochemical deposition may be used to coat active materials onto the self-assembled colloidal templates, which can subsequently be removed.

Since the assembly of colloids is largely driven by the surface interactions, particles made from different materials can be substituted for those presented in this work. Substituting materials with higher refractive indexes for silica is potentially a straight-forward approach for increasing the optical scattering of the gels presented in chapter 4. A greater index contrast between the colloids-rich and colloid-free phases would move the system out of the Rayleigh-Gans scattering regime and may enable the reflection of a full color spectrum.

The use of covalent bonds rather than DNA-mediate interactions to self-assemble the silicon-carbon nanotube composite shows how the concept of colloidal self-assembly can be simplified. In this example, the minimal requirements of an externally triggered, short range attraction between two different materials could potentially be reduced further. Adding an anti-dispersant to a dispersion of silicon nanoparticles and carbon nanotubes could eliminate the need for functional handles on the colloids. Instead, once the precursor dispersion of

silicon and carbon was disrupted by adding the anti-dispersant, the colloids would assemble into a porous structure held together through Van der Waals interactions.

The example of rod-sphere interactions demonstrates how the geometry of the colloidal building blocks can be used to control the structure of nanoparticle gels. Certainly, colloids consisting of other shapes could also be used to form gels with alternative porosities. More complex structures may be formed through that application of external fields including flow, electronic and magnetic fields to break the symmetry inherent to the isotropic colloidal assemblies.

The concepts explored in this thesis represent a few basic examples of exploiting colloidal self-assembly to produce functional materials. Introducing specific functionalities to the surface of colloids allowed for the engineering of systems governed by specific binding rules and the assemble colloids consisting of dissimilar materials. By selecting the minimum requirements of an application from this approach, it may be possible to harness the unique classical and quantum mechanical properties of nanoparticles in novel ways.

## 7 Appendix

### 7.1 Effect of Inert Tails on DNA Hybridization

UV absorption, melt curve measurements are a powerful tool for understanding DNA hybridization. The wide use of short strands of synthetic ssDNA has led to simple computer programs to calculate the free energy of DNA hybridization ( $\Delta G$ ) based on the model developed by SantaLucia.<sup>35, 36</sup> The SantaLucia model takes into account both the free energy contributions of nearest-neighbor pairs of bases and the unpaired bases immediately adjacent to the duplex regions. However, the model does not explicitly consider the contributions from non-binding bases in ssDNA oligomers that occur in many experimental systems such as in DNACCs. Experiments and simulations were performed to investigate the effects of the inert bases on the free energy of DNA hybridization.<sup>12</sup>

Melt curves was used to quantify the free energy of hybridization of complementary DNA sequences (IDT) with different lengths and orientations, same-side (3', 5') and opposite sides (5', 5'), of inert tails. The free energy can be calculated from the melt temperature and the concentration of DNA in solution ( $\rho$ ):

$$\Delta G = RT_m \ln \frac{\rho}{2} \quad (29)$$

To generate the melt curves, short ssDNA oligomers were purchased commercially (Integrated DNA technologies) with varied lengths of binding motifs (7-13 bases) and inert tails (0-11 bases). The amount of DNA supplied by the vendor was carefully measured using a nano-drop UV spectrometer in conjunction with the sequence dependent extinction coefficients provided by the IDT. Phosphate buffer saline (PBS) solutions of equal molar complementary DNA strands were then carefully prepared and their melt curves were measured at different salt concentrations. Heating and cooling rates were chosen to maintain thermodynamic equilibrium (0.3 °C/min). The change in the free energy of hybridization due to the inert tails with respect to ssDNA sequences without inert tails can be defined as:

$$\delta\Delta G(n_{tail}) = \Delta G(n_{tail}) - \Delta G^0(n_{tail} = 0) \quad (30)$$

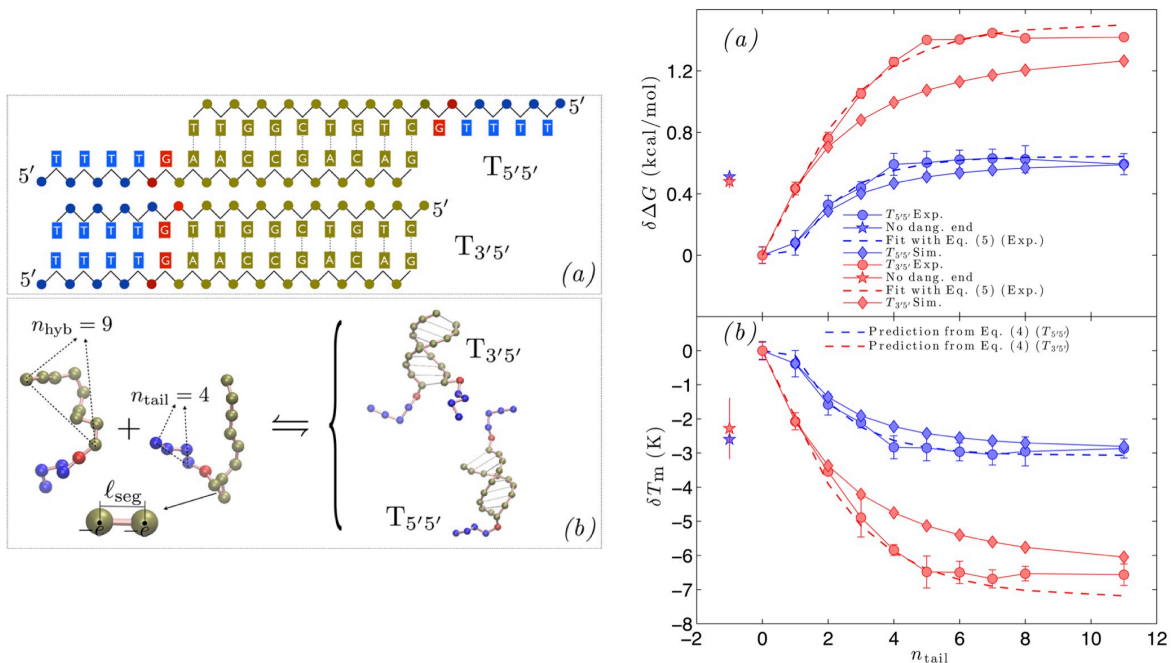


Figure 73: Schematics of hybridized DNA with inert single-stranded spacers (left, b) and simulation snapshots of the hybridizing oligomers (left, b). Plots showing the change in free-energy (right, a) and the change in melt temperature ( $T_m$ , right, a) as a function of the length of the inert tails. Figure adapted with permission from reference,<sup>12</sup> Copyright 2014, American Chemical Society.

The effect of inert tail length and orientation is shown in Figure 73. Initially, the inert tails have a strong effect on the free energy of hybridization. At  $n_{\text{tail}} = 5$ , the effect saturates at  $\sim 0.6$  kcal/mol for the opposite side configuration and  $\sim 1.3$  kcal/mol for the same side configuration. There is a corresponding change in the melt temperature of the DNA strands. Electrostatic repulsion between the inert tails was hypothesized to be the mechanism for the observed shift in free energy and this result was supported with simulations. Additional measurements to separate the enthalpic and entropic contributions are needed to confirm this mechanism.

## 7.2 Hydrosilylation of Silicon Nanoparticles with Polymers

As discussed in section 5.2, coating silicon nanoparticles with an artificial SEI layer is a possible approach to preventing electrolyte degradation in silicon anodes. Polyethylene glycol (PEO, PEG) has been shown to be a main component of the SEI in silicon anodes.<sup>138, 141</sup> As a first step towards understanding and synthesizing an artificial SEI, experiments were performed to coat silicon nanoparticles with polyethylene methacrylate (PM) using a hydrosilylation reaction, where the acrylate group reacts with the hydrogenated-silicon surface to form Si-C bonds (Figure 74). To form silicon nanoparticles with a PEG coating, the silicon nanoparticles first were mixed with THF and sonicated. The PEG-PM (2 kDa) was then added to the SiNP/THF mixture and the mixture was irradiated with UV light. The nanoparticles were then washed with THF and pentane to remove the residual PM and hexadecane.

The PEG coated silicon nanoparticles (SiNP-PEG) were characterized based on their dispersion properties, IR absorption spectra and electrochemical properties. After functionalization, the SiNP-PEG could be well-dispersed in a range of solvents including polar solvents, compared to the unmodified SiNP which were best dispersed in THF. FTIR absorption measurements on the SiNP-PEG showed the vibrational signatures of PEG. However, direct evidence of the hydrosilylation reaction could not be extracted from the FTIR measurements due to the Si-C absorption bands overlapping with the Si-O bands. Electrochemical measurements on SiNP-PEG drop-cast to form anodes showed a small improvement in capacity fade compared to anodes made from uncoated SiNP. However, the lower capacity fade may simply be attributed improved dispersion of the functionalized nanoparticles in precursor anode solution. More careful studies of the potential usage of hydrosilylation reactions to coat silicon anodes with an artificial SEI layer on planar silicon

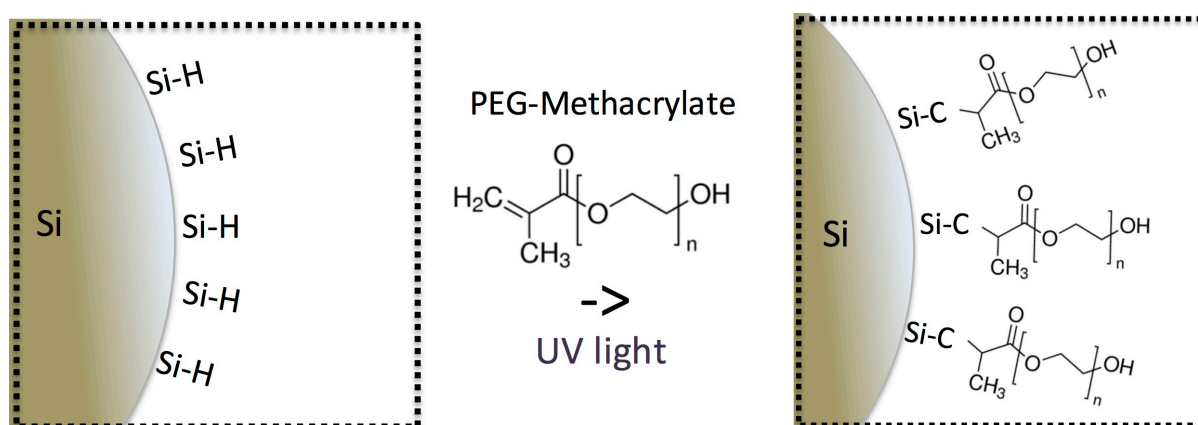


Figure 74: Hydrosilylation reaction between hydrogen-terminated silicon and PEG-methacrylate in THF.

substrates that are 150 nm thick are ongoing. Various monomers and polymers are currently under investigation include artificial SEI layers made from acrylic acid, phosphines and PEO species rich with amines.

## 8 References

1. Barhoumi, A.; Zhang, D.; Tam, F.; Halas, N. J., Surface-Enhanced Raman Spectroscopy of DNA. *Journal of the American Chemical Society* 2008, 130, (16), 5523-5529.
2. Xu, L.-J.; Lei, Z.-C.; Li, J.; Zong, C.; Yang, C. J.; Ren, B., Label-Free Surface-Enhanced Raman Spectroscopy Detection of DNA with Single-Base Sensitivity. *Journal of the American Chemical Society* 2015, 137, (15), 5149-5154.
3. Movileanu, L.; Benevides, J. M.; Thomas, G. J., Temperature dependence of the raman spectrum of DNA. Part I—Raman signatures of premelting and melting transitions of poly (dA–dT)· poly (dA–dT). *Journal of Raman Spectroscopy* 1999, 30, (8), 637-649.
4. Green, M.; Liu, F.-M.; Cohen, L.; Kollensperger, P.; Cass, T., SERS platforms for high density DNA arrays. *Faraday Discussions* 2006, 132, (0), 269-280.
5. Takeoka, Y., Angle-independent structural coloured amorphous arrays. *Journal of Materials Chemistry* 2012, 22, (44), 23299.
6. Emanuela, Z., Colloidal gels: equilibrium and non-equilibrium routes. *Journal of Physics: Condensed Matter* 2007, 19, (32), 323101.
7. Prum, R. O.; Torres, R. H., A Fourier Tool for the Analysis of Coherent Light Scattering by Bio-Optical Nanostructures<sup>1</sup>. *Integrative and Comparative Biology* 2003, 43, (4), 591-602.
8. Ruff, Z.; Nathan, S. H.; Unwin, R. R.; Zupkauskas, M.; Joshi, D.; Salmond, G. P. C.; Grey, C. P.; Eiser, E., Designing disordered materials using DNA-coated colloids of bacteriophage fd and gold. *Faraday Discussions* 2015.
9. Stiles, P. L.; Dieringer, J. A.; Shah, N. C.; Duyn, R. P. V., Surface-Enhanced Raman Spectroscopy. *Annual Review of Analytical Chemistry* 2008, 1, (1), 601-626.
10. Unwin, R. R.; Cabanas, R. A.; Yanagishima, T.; Blower, T. R.; Takahashi, H.; Salmond, G. P. C.; Edwardson, J. M.; Fraden, S.; Eiser, E., DNA driven self-assembly of micron-sized rods using DNA-grafted bacteriophage fd virions. *Physical Chemistry Chemical Physics* 2015, 17, (12), 8194-8202.
11. Guerrini, L.; Graham, D., Molecularly-mediated assemblies of plasmonic nanoparticles for Surface-Enhanced Raman Spectroscopy applications. *Chemical Society Reviews* 2012, 41, (21), 7085-7107.
12. Di Michele, L.; Moggetti, B. M.; Yanagishima, T.; Varilly, P.; Ruff, Z.; Frenkel, D.; Eiser, E., Effect of Inert Tails on the Thermodynamics of DNA Hybridization. *Journal of the American Chemical Society* 2014, 136, (18), 6538-6541.
13. Di Michele, L.; Varrato, F.; Kotar, J.; Nathan, S. H.; Foffi, G.; Eiser, E., Multistep kinetic self-assembly of DNA-coated colloids. *Nat Commun* 2013, 4, 2007.
14. Zhang, H.; Yu, X.; Braun, P. V., Three-dimensional bicontinuous ultrafast-charge and -discharge bulk battery electrodes. *Nat Nanotechnol* 2011, 6, (5), 277-81.
15. Nykypanchuk, D.; Maye, M. M.; van der Lelie, D.; Gang, O., DNA-guided crystallization of colloidal nanoparticles. *Nature* 2008, 451, (7178), 549-52.
16. Cho, Y. K.; Wartena, R.; Tobias, S. M.; Chiang, Y. M., Self-Assembling Colloidal-Scale Devices: Selecting and Using Short-Range Surface Forces Between Conductive Solids. *Advanced Functional Materials* 2007, 17, (3), 379-389.
17. Chung, S.-Y.; Bloking, J. T.; Chiang, Y.-M., Electronically conductive phospho-olivines as lithium storage electrodes. *Nature materials* 2002, 1, (2), 123-128.
18. Ermolov, V.; Heino, M.; Karkkainen, A.; Lehtiniemi, R.; Nefedov, N.; Pasanen, P.; Radivojevic, Z.; Rouvala, M.; Ryhanen, T.; Seppala, E. In *Significance of nanotechnology for future wireless devices and communications*, Personal, Indoor and Mobile Radio

- Communications, 2007. PIMRC 2007. IEEE 18th International Symposium on, 2007; IEEE: 2007; pp 1-5.
19. Moore, G. E., Cramming more components onto integrated circuits. *Proceedings of the IEEE* 1998, 86, (1), 82-85.
  20. Shi, J.; Votruba, A. R.; Farokhzad, O. C.; Langer, R., Nanotechnology in Drug Delivery and Tissue Engineering: From Discovery to Applications. *Nano Letters* 2010, 10, (9), 3223-3230.
  21. Varrato, F.; Di Michele, L.; Belushkin, M.; Dorsaz, N.; Nathan, S. H.; Eiser, E.; Foffi, G., Arrested demixing opens route to bigels. *Proceedings of the National Academy of Sciences* 2012, 109, 19155–19160.
  22. Whitesides, G. M.; Boncheva, M., Beyond molecules: Self-assembly of mesoscopic and macroscopic components. *Proceedings of the National Academy of Sciences* 2002, 99, (8), 4769-4774.
  23. Berger, V.; Gauthier-Lafaye, O.; Costard, E., Photonic band gaps and holography. *Journal of Applied Physics* 1997, 82, (1), 60-64.
  24. Cheng, J. Y.; Mayes, A. M.; Ross, C. A., Nanostructure engineering by templated self-assembly of block copolymers. *Nat Mater* 2004, 3, (11), 823-8.
  25. Lu, P. J.; Zaccarelli, E.; Ciulla, F.; Schofield, A. B.; Sciortino, F.; Weitz, D. A., Gelation of particles with short-range attraction. *Nature* 2008, 453, (7194), 499-503.
  26. Mirkin, C. A.; Letsinger, R. L.; Mucic, R. C.; Storhoff, J. J., A DNA-based method for rationally assembling nanoparticles into macroscopic materials. *Nature* 1996, 382, (6592), 607-609.
  27. Alivisatos, A. P.; Johnsson, K. P.; Peng, X.; Wilson, T. E.; Loweth, C. J.; Bruchez, M. P.; Schultz, P. G., Organization of 'nanocrystal molecules' using DNA. *Nature* 1996, 382, (6592), 609-611.
  28. Geerts, N.; Eiser, E., DNA-functionalized colloids: Physical properties and applications. *Soft Matter* 2010, 6, (19), 4647.
  29. Israelachvili, J. N., *Intermolecular and Surface Forces, Third Edition*. Third ed.; Academic Press: 2011.
  30. Derjaguin, B. L., L., Theory of the stability of strongly charged lyophobic sols and of the adhesion of strongly charged particles in solutions of electrolytes. *Acta Physico Chemica URSS*, (14), 633.
  31. Overbeek, E. J. V. a. J. T. G., *Theory of the Stability of Lyophobic Colloids*. Elsevier.
  32. Watson, J. D.; Crick, F. H. C., Molecular Structure of Nucleic Acids: A Structure for Deoxyribose Nucleic Acid. *Nature* 1953, 171, (4356), 737-738.
  33. Tinland, B.; Pluen, A.; Sturm, J.; Weill, G., Persistence Length of Single-Stranded DNA. *Macromolecules* 1997, 30, (19), 5763-5765.
  34. Brinkers, S.; Dietrich, H. R. C.; de Groot, F. H.; Young, I. T.; Rieger, B., The persistence length of double stranded DNA determined using dark field tethered particle motion. *The Journal of Chemical Physics* 2009, 130, (21), -.
  35. SantaLucia, J., A unified view of polymer, dumbbell, and oligonucleotide DNA nearest-neighbor thermodynamics. *Proceedings of the National Academy of Sciences* 1998, 95, (4), 1460-1465.
  36. SantaLucia, J.; Hicks, D., THE THERMODYNAMICS OF DNA STRUCTURAL MOTIFS. *Annual Review of Biophysics and Biomolecular Structure* 2004, 33, (1), 415-440.
  37. Tinoco, I., Hypochromism in Polynucleotides1. *Journal of the American Chemical Society* 1960, 82, (18), 4785-4790.

38. BAIN, C. D.; WHITESIDES, G. M., Molecular-Level Control over Surface Order in Self-Assembled Monolayer Films of Thiols on Gold. *Science* 1988, 240, (4848), 62-63.
39. Brust, M.; Schiffrin, D. J.; Bethell, D.; Kiely, C. J., Novel gold-dithiol nano-networks with non-metallic electronic properties. *Advanced Materials* 1995, 7, (9), 795-797.
40. Jin, R.; Wu, G.; Li, Z.; Mirkin, C. A.; Schatz, G. C., What Controls the Melting Properties of DNA-Linked Gold Nanoparticle Assemblies? *Journal of the American Chemical Society* 2003, 125, (6), 1643-1654.
41. Hurst, S. J.; Lytton-Jean, A. K. R.; Mirkin, C. A., Maximizing DNA Loading on a Range of Gold Nanoparticle Sizes. *Analytical Chemistry* 2006, 78, (24), 8313-8318.
42. Park, S. Y.; Lytton-Jean, A. K. R.; Lee, B.; Weigand, S.; Schatz, G. C.; Mirkin, C. A., DNA-programmable nanoparticle crystallization. *Nature* 2008, 451, (7178), 553-556.
43. Maye, M. M.; Nykypanchuk, D.; van der Lelie, D.; Gang, O., A Simple Method for Kinetic Control of DNA-Induced Nanoparticle Assembly. *Journal of the American Chemical Society* 2006, 128, (43), 14020-14021.
44. Maye, M. M.; Nykypanchuk, D.; van der Lelie, D.; Gang, O., DNA-regulated micro- and nanoparticle assembly. *Small* 2007, 3, (10), 1678-82.
45. Sharma, J.; Chhabra, R.; Liu, Y.; Ke, Y.; Yan, H., DNA-templated self-assembly of two-dimensional and periodical gold nanoparticle arrays. *Angew Chem Int Ed Engl* 2006, 45, (5), 730-5.
46. Macfarlane, R. J.; Lee, B.; Jones, M. R.; Harris, N.; Schatz, G. C.; Mirkin, C. A., Nanoparticle superlattice engineering with DNA. *Science* 2011, 334, (6053), 204-8.
47. Zhang, C.; Macfarlane, R. J.; Young, K. L.; Choi, C. H. J.; Hao, L.; Auyeung, E.; Liu, G.; Zhou, X.; Mirkin, C. A., A general approach to DNA-programmable atom equivalents. *Nat Mater* 2013, 12, (8), 741-746.
48. Geerts, N.; Schmatko, T.; Eiser, E., Clustering versus Percolation in the Assembly of Colloids Coated with Long DNA. *Langmuir* 2008, 24, (9), 5118-5123.
49. Schmatko, T.; Bozorgui, B.; Geerts, N.; Frenkel, D.; Eiser, E.; Poon, W. C. K., A finite-cluster phase in  $\beta$ -DNA-coated colloids. *Soft Matter* 2007, 3, (6), 703.
50. Valignat, M. P.; Theodoly, O.; Crocker, J. C.; Russel, W. B.; Chaikin, P. M., Reversible self-assembly and directed assembly of DNA-linked micrometer-sized colloids. *Proc Natl Acad Sci U S A* 2005, 102, (12), 4225-9.
51. Kim, A. J.; Biancaniello, P. L.; Crocker, J. C., Engineering DNA-Mediated Colloidal Crystallization. *Langmuir* 2006, 22, (5), 1991-2001.
52. Di Michele, L.; Fiocco, D.; Varrato, F.; Sastry, S.; Eiser, E.; Foffi, G., Aggregation dynamics, structure, and mechanical properties of bigels. *Soft Matter* 2014, 10, (20), 3633-3648.
53. Wang, Y.; Wang, Y.; Zheng, X.; Ducrot, E.; Yodh, J. S.; Weck, M.; Pine, D. J., Crystallization of DNA-coated colloids. *Nat Commun* 2015, 6.
54. Park, J.-G.; Kim, S.-H.; Magkiriadou, S.; Choi, T. M.; Kim, Y.-S.; Manoharan, V. N., Full-Spectrum Photonic Pigments with Non-iridescent Structural Colors through Colloidal Assembly. *Angewandte Chemie International Edition* 2014, 53, (11), 2899-2903.
55. Teshima, M.; Seki, T.; Kawano, R.; Takeuchi, S.; Yoshioka, S.; Takeoka, Y., Preparation of structurally colored, monodisperse spherical assemblies composed of black and white colloidal particles using a micro-flow-focusing device. *Journal of Materials Chemistry C* 2015, 3, (4), 769-777.
56. Prum, R. O.; Torres, R. H.; Williamson, S.; Dyck, J., Coherent light scattering by blue feather barbs. *Nature* 1998, 396, (6706), 28-29.

57. Dufresne, E. R.; Noh, H.; Saranathan, V.; Mochrie, S. G. J.; Cao, H.; Prum, R. O., Self-assembly of amorphous biophotonic nanostructures by phase separation. *Soft Matter* 2009, 5, (9), 1792-1795.
58. Parnell, A. J.; Washington, A. L.; Mykhaylyk, O. O.; Hill, C. J.; Bianco, A.; Burg, S. L.; Dennison, A. J. C.; Snape, M.; Cadby, A. J.; Smith, A.; Prevost, S.; Whittaker, D. M.; Jones, R. A. L.; Fairclough, J. P. A.; Parker, A. R., Spatially modulated structural colour in bird feathers. *Scientific Reports* 2015, 5, 18317.
59. Takeoka, Y.; Honda, M.; Seki, T.; Ishii, M.; Nakamura, H., Structural Colored Liquid Membrane without Angle Dependence. *ACS Applied Materials & Interfaces* 2009, 1, (5), 982-986.
60. Harun-Ur-Rashid, M.; Imran, A. B.; Seki, T.; Takeoka, Y.; Ishii, M.; Nakamura, H., Template Synthesis for Stimuli-Responsive Angle Independent Structural Colored Smart Materials. *Transactions of the Materials Research Society of Japan* 2009, 34, (2), 333-337.
61. Magkiriadou, S.; Park, J.-G.; Kim, Y.-S.; Manoharan, V. N., Disordered packings of core-shell particles with angle-independent structural colors. *Optical Materials Express* 2012, 2, (10), 1343-1352.
62. Long, J. W.; Dunn, B.; Rolison, D. R.; White, H. S., Three-Dimensional Battery Architectures. *Chemical Reviews* 2004, 104, (10), 4463-4492.
63. Rolison, D. R.; Long, J. W.; Lytle, J. C.; Fischer, A. E.; Rhodes, C. P.; McEvoy, T. M.; Bourg, M. E.; Lubers, A. M., Multifunctional 3D nanoarchitectures for energy storage and conversion. *Chem Soc Rev* 2009, 38, (1), 226-52.
64. Braun, P. V.; Cho, J.; Pikul, J. H.; King, W. P.; Zhang, H., High power rechargeable batteries. *Current Opinion in Solid State and Materials Science* 2012, 16, (4), 186-198.
65. Sakamoto, J. S.; Dunn, B., Hierarchical battery electrodes based on inverted opal structures. *Journal of Materials Chemistry* 2002, 12, (10), 2859-2861.
66. Tonti, D.; Torralvo, M. J.; Enciso, E.; Sobrados, I.; Sanz, J., Three-Dimensionally Ordered Macroporous Lithium Manganese Oxide for Rechargeable Lithium Batteries. *Chemistry of Materials* 2008, 20, (14), 4783-4790.
67. Haetge, J.; Hartmann, P.; Brezesinski, K.; Janek, J.; Brezesinski, T., Ordered Large-Pore Mesoporous Li<sub>4</sub>Ti<sub>5</sub>O<sub>12</sub> Spinel Thin Film Electrodes with Nanocrystalline Framework for High Rate Rechargeable Lithium Batteries: Relationships among Charge Storage, Electrical Conductivity, and Nanoscale Structure. *Chemistry of Materials* 2011, 23, (19), 4384-4393.
68. Brezesinski, T.; Wang, J.; Polleux, J.; Dunn, B.; Tolbert, S. H., Templated Nanocrystal-Based Porous TiO<sub>2</sub> Films for Next-Generation Electrochemical Capacitors. *Journal of the American Chemical Society* 2009, 131, (5), 1802-1809.
69. Grätzel, M., Dye-sensitized solar cells. *Journal of Photochemistry and Photobiology C: Photochemistry Reviews* 2003, 4, (2), 145-153.
70. Stöber, W.; Fink, A.; Bohn, E., Controlled growth of monodisperse silica spheres in the micron size range. *Journal of Colloid and Interface Science* 1968, 26, (1), 62-69.
71. Smoluchowski, M. v., Contribution to the theory of electro-osmosis and related phenomena. *Bull Int Acad Sci Cracovie* 1903, 3, 184-199.
72. Oh, J. S.; Wang, Y.; Pine, D. J.; Yi, G.-R., High-Density PEO-b-DNA Brushes on Polymer Particles for Colloidal Superstructures. *Chemistry of Materials* 2015.
73. Lukatsky, D.; Frenkel, D., Phase Behavior and Selectivity of DNA-Linked Nanoparticle Assemblies. *Physical Review Letters* 2004, 92, (6).

74. Huang, B.; Wang, W.; Bates, M.; Zhuang, X., Three-Dimensional Super-Resolution Imaging by Stochastic Optical Reconstruction Microscopy. *Science* 2008, 319, (5864), 810-813.
75. Song, C.; Wang, P.; Makse, H. A., A phase diagram for jammed matter. *Nature* 2008, 453, (7195), 629-632.
76. Levitz, P.; Tchoubar, D., Disordered porous solids : from chord distributions to small angle scattering. *Journal de Physique I* 1992, 2, (6), 771-790.
77. Levitz, P., Off-lattice reconstruction of porous media: critical evaluation, geometrical confinement and molecular transport. *Advances in Colloid and Interface Science* 1998, 76-77, 71-106.
78. Levitz, P., Toolbox for 3D imaging and modeling of porous media: Relationship with transport properties. *Cement and Concrete Research* 2007, 37, (3), 351-359.
79. Otsu, N., A Threshold Selection Method from Gray-Level Histograms. *IEEE Transactions on Systems, Man, and Cybernetics* 1979, 9, (1), 62-66.
80. Zupkauskas, M.; Lan, Y.; Joshi, D.; Ruff, Z.; Eiser, E., Optically Transparent Dense Colloidal Gels. *Chemical Science* 2017.
81. Ru, E. C. L.; Etchegoin, P. G.; Meyer, M., Enhancement factor distribution around a single surface-enhanced Raman scattering hot spot and its relation to single molecule detection. *The Journal of Chemical Physics* 2006, 125, (20), 204701.
82. Kneipp, K.; Wang, Y.; Kneipp, H.; Perelman, L. T.; Itzkan, I.; Dasari, R. R.; Feld, M. S., Single molecule detection using surface-enhanced Raman scattering (SERS). *Physical review letters* 1997, 78, (9), 1667.
83. Sun, D.; Gang, O., Binary Heterogeneous Superlattices Assembled from Quantum Dots and Gold Nanoparticles with DNA. *Journal of the American Chemical Society* 2011, 133, (14), 5252-5254.
84. Stoeva, S. I.; Lee, J. S.; Thaxton, C. S.; Mirkin, C. A., Multiplexed DNA detection with biobarcoded nanoparticle probes. *Angew Chem Int Ed Engl* 2006, 45, (20), 3303-6.
85. Heck, C.; Prinz, J.; Dathe, A.; Merk, V.; Stranik, O.; Fritzsche, W.; Kneipp, J.; Bald, I., Gold Nanolenses Self-Assembled by DNA Origami. *ACS Photonics* 2017, 4, (5), 1123-1130.
86. Zhang, Z.; Wen, Y.; Ma, Y.; Luo, J.; Jiang, L.; Song, Y., Mixed DNA-functionalized nanoparticle probes for surface-enhanced Raman scattering-based multiplex DNA detection. *Chemical Communications* 2011, 47, (26), 7407-7409.
87. Thacker, V. V.; Herrmann, L. O.; Sigle, D. O.; Zhang, T.; Liedl, T.; Baumberg, J. J.; Keyser, U. F., DNA origami based assembly of gold nanoparticle dimers for surface-enhanced Raman scattering. *Nature communications* 2014, 5, 3448.
88. Zhang, Y.; Lu, F.; Yager, K. G.; van der Lelie, D.; Gang, O., A general strategy for the DNA-mediated self-assembly of functional nanoparticles into heterogeneous systems. *Nat Nanotechnol* 2013, 8, (11), 865-72.
89. Liu, W.; Halverson, J.; Tian, Y.; Tkachenko, A. V.; Gang, O., Self-organized architectures from assorted DNA-framed nanoparticles. *Nat Chem* 2016, 8, (9), 867-873.
90. Shirley, D. A., High-Resolution X-Ray Photoemission Spectrum of the Valence Bands of Gold. *Physical Review B* 1972, 5, (12), 4709-4714.
91. Jones, R. A., *Soft condensed matter*. Oxford University Press: 2002; Vol. 6.
92. McQuarrie, D., *Statistical Mechanics*. 2000. Sausalito, Calif.: University Science Books 2004, 12, 641.

93. Auyeung, E.; Macfarlane, R. J.; Choi, C. H.; Cutler, J. I.; Mirkin, C. A., Transitioning DNA-engineered nanoparticle superlattices from solution to the solid state. *Adv Mater* 2012, 24, (38), 5181-6.
94. de Gennes, P. G., Conformations of Polymers Attached to an Interface. *Macromolecules* 1980, 13, (5), 1069-1075.
95. Perry, J. L.; Reuter, K. G.; Kai, M. P.; Herlihy, K. P.; Jones, S. W.; Luft, J. C.; Napier, M.; Bear, J. E.; DeSimone, J. M., PEGylated PRINT nanoparticles: the impact of PEG density on protein binding, macrophage association, biodistribution, and pharmacokinetics. *Nano letters* 2012, 12, (10), 5304-5310.
96. Wu, Y.; Koch, W.; Pratt, K., Proposed new electrolytic conductivity primary standards for KCl solutions. *Journal of research of the National Institute of Standards and Technology* 1991, 96, (2), 191.
97. Candy, J.-P.; Fouilloux, P.; Keddam, M.; Takenouti, H., The characterization of porous electrodes by impedance measurements. *Electrochimica Acta* 1981, 26, (8), 1029-1034.
98. De Levie, R., On porous electrodes in electrolyte solutions: I. Capacitance effects. *Electrochimica Acta* 1963, 8, (10), 751-780.
99. De Levie, R., On porous electrodes in electrolyte solutions—IV. *Electrochimica acta* 1964, 9, (9), 1231-1245.
100. Wang, G. R.; Wang, L.; Rendeng, Q.; Wang, J.; Luo, J.; Zhong, C.-J., Correlation between nanostructural parameters and conductivity properties for molecularly-mediated thin film assemblies of gold nanoparticles. *Journal of Materials Chemistry* 2007, 17, (5), 457-462.
101. Yu, X.; Malvankar, N.; Landis, R.; Eymur, S.; Miranda, O. R.; Rotello, V. M., Impedance Spectroscopy of Ionic Ligand-Modulated Charge Transport of Gold Nanoparticle Films. *Small* 2015, 11, (31), 3814-3821.
102. Sheng, P.; Abeles, B., Voltage-Induced Tunneling Conduction in Granular Metals at Low Temperatures. *Physical Review Letters* 1972, 28, (1), 34-37.
103. Park, S.-J.; Lazarides, A. A.; Mirkin, C. A.; Brazis, P. W.; Kannewurf, C. R.; Letsinger, R. L., The Electrical Properties of Gold Nanoparticle Assemblies Linked by DNA. *Angewandte Chemie International Edition* 2000, 39, (21), 3845-3848.
104. Houlton, A.; Watson, S. M. D., DNA-based nanowires. Towards bottom-up nanoscale electronics. *Annual Reports Section "A" (Inorganic Chemistry)* 2011, 107, 21.
105. Ford, W. E.; Harnack, O.; Yasuda, A.; Wessels, J. M., Platinated DNA as Precursors to Templated Chains of Metal Nanoparticles. *Advanced Materials* 2001, 13, (23), 1793-1797.
106. Braun, E.; Eichen, Y.; Sivan, U.; Ben-Yoseph, G., DNA-templated assembly and electrode attachment of a conducting silver wire. *Nature* 1998, 391, (6669), 775-778.
107. Houlton, A.; Watson, S. M. D., DNA-based nanowires. Towards bottom-up nanoscale electronics. *Annual Reports Section "A" (Inorganic Chemistry)* 2011, 107, (0), 21-42.
108. Kleinman, S. L.; Sharma, B.; Blaber, M. G.; Henry, A.-I.; Valley, N.; Freeman, R. G.; Natan, M. J.; Schatz, G. C.; Van Duyne, R. P., Structure Enhancement Factor Relationships in Single Gold Nanoantennas by Surface-Enhanced Raman Excitation Spectroscopy. *Journal of the American Chemical Society* 2013, 135, (1), 301-308.
109. Pilo-Pais, M.; Watson, A.; Demers, S.; LaBean, T.; Finkelstein, G., Surface-enhanced Raman scattering plasmonic enhancement using DNA origami-based complex metallic nanostructures. *Nano letters* 2014, 14, (4), 2099-2104.
110. Movileanu, L.; Benevides, J. M.; Thomas, G. J., Temperature dependence of the raman spectrum of DNA. II. Raman signatures of premelting and melting transitions of poly

- (dA)· poly (dT) and comparison with poly (dA-dT)· poly (dA-dT). *Biopolymers* 2002, 63, (3), 181-194.
111. Wang, Y.; Wang, Y.; Zheng, X.; Ducrot, É.; Lee, M.-G.; Yi, G.-R.; Weck, M.; Pine, D. J., Synthetic Strategies Toward DNA-Coated Colloids that Crystallize. *Journal of the American Chemical Society* 2015, 137, (33), 10760-10766.
112. Parak, W. J.; Gerion, D.; Zanchet, D.; Woerz, A. S.; Pellegrino, T.; Micheel, C.; Williams, S. C.; Seitz, M.; Bruehl, R. E.; Bryant, Z.; Bustamante, C.; Bertozzi, C. R.; Alivisatos, A. P., Conjugation of DNA to Silanized Colloidal Semiconductor Nanocrystalline Quantum Dots. *Chemistry of Materials* 2002, 14, (5), 2113-2119.
113. Walsh, M. K.; Wang, X.; Weimer, B. C., Optimizing the immobilization of single-stranded DNA onto glass beads. *Journal of Biochemical and Biophysical Methods* 2001, 47, (3), 221-231.
114. Lockett, M. R.; Phillips, M. F.; Jarecki, J. L.; Peelen, D.; Smith, L. M., A tetrafluorophenyl activated ester self-assembled monolayer for the immobilization of amine-modified oligonucleotides. *Langmuir* 2008, 24, (1), 69-75.
115. Thyagarajan, S.; Murthy, N. N.; Narducci Sarjeant, A. A.; Karlin, K. D.; Rokita, S. E., Selective DNA Strand Scission with Binuclear Copper Complexes: Implications for an Active Cu<sub>2</sub>-O<sub>2</sub> Species. *Journal of the American Chemical Society* 2006, 128, (21), 7003-7008.
116. Cervantes-Cervantes, M. P.; Calderón-Salinas, J. V.; Albores, A.; Muñoz-Sánchez, J. L., Copper increases the damage to DNA and proteins caused by reactive oxygen species. *Biological trace element research* 2005, 103, (3), 229-248.
117. Orski, S. V.; Sheppard, G. R.; Arumugam, S.; Arnold, R. M.; Popik, V. V.; Locklin, J., Rate Determination of Azide Click Reactions onto Alkyne Polymer Brush Scaffolds: A Comparison of Conventional and Catalyst-Free Cycloadditions for Tunable Surface Modification. *Langmuir* 2012, 28, (41), 14693-14702.
118. Lee, H.; Venable, R. M.; Mackerell Jr, A. D.; Pastor, R. W., Molecular Dynamics Studies of Polyethylene Oxide and Polyethylene Glycol: Hydrodynamic Radius and Shape Anisotropy. *Biophysical Journal* 2008, 95, (4), 1590-1599.
119. M'Pandou, A.; Siffert, B., Polyethyleneglycol adsorption at the TiO<sub>2</sub> H<sub>2</sub>O interface: Distortion of ionic structure and shear plane position. *Colloids and Surfaces* 1987, 24, (2), 159-172.
120. Liu, H.; Xiao, H., Adsorption of poly(ethylene oxide) with different molecular weights on the surface of silica nanoparticles and the suspension stability. *Materials Letters* 2008, 62, (6-7), 870-873.
121. Wang, Q.; Chan, T. R.; Hilgraf, R.; Fokin, V. V.; Sharpless, K. B.; Finn, M. G., Bioconjugation by Copper(I)-Catalyzed Azide-Alkyne [3 + 2] Cycloaddition. *Journal of the American Chemical Society* 2003, 125, (11), 3192-3193.
122. Shay, J. S.; Raghavan, S. R.; Khan, S. A., Thermoreversible gelation in aqueous dispersions of colloidal particles bearing grafted poly(ethylene oxide) chains. *Journal of Rheology* 2001, 45, (4), 913.
123. Gillich, T.; Acikgöz, C.; Isa, L.; Schlüter, A. D.; Spencer, N. D.; Textor, M., PEG-Stabilized Core-Shell Nanoparticles: Impact of Linear versus Dendritic Polymer Shell Architecture on Colloidal Properties and the Reversibility of Temperature-Induced Aggregation. *ACS Nano* 2013, 7, (1), 316-329.
124. Yanagishima, T.; Di Michele, L.; Kotar, J.; Eiser, E., Diffusive behaviour of PLL-PEG coated colloids on λ-DNA brushes – tuning hydrophobicity. *Soft Matter* 2012, 8, (25), 6792.

125. Feng, L.; Laderman, B.; Sacanna, S.; Chaikin, P., Re-entrant solidification in polymer–colloid mixtures as a consequence of competing entropic and enthalpic attractions. *Nat Mater* 2015, 14, (1), 61–65.
126. Cohen-Tannoudji, L.; Bertrand, E.; Bressy, L.; Goubault, C.; Baudry, J.; Klein, J.; Joanny, J.-F.; Bibette, J., Polymer bridging probed by magnetic colloids. *Physical review letters* 2005, 94, (3), 038301.
127. Swan, J. W.; Zia, R. N.; Brady, J. F., Large amplitude oscillatory microrheology. *Journal of Rheology* 2014, 58, (1), 1–41.
128. Xie, F.; Woodward, C. E.; Forsman, J., Theoretical Predictions of Temperature-Induced Gelation in Aqueous Dispersions Containing PEO-Grafted Particles. *The Journal of Physical Chemistry B* 2016, 120, (16), 3969–3977.
129. Fan, F. Y.; Woodford, W. H.; Li, Z.; Baram, N.; Smith, K. C.; Helal, A.; McKinley, G. H.; Carter, W. C.; Chiang, Y. M., Polysulfide flow batteries enabled by percolating nanoscale conductor networks. *Nano Lett* 2014, 14, (4), 2210–8.
130. Garnett, J. C. M., Colours in Metal Glasses and in Metallic Films. *Philosophical Transactions of the Royal Society of London. Series A, Containing Papers of a Mathematical or Physical Character* 1904, 203, (359–371), 385–420.
131. van de Hulst, H., Light scattering by small particles. 1981.
132. Magkiriadou, S.; Park, J.-G.; Kim, Y.-S.; Manoharan, V. N., Absence of red structural color in photonic glasses, bird feathers, and certain beetles. *Physical Review E* 2014, 90, (6), 062302.
133. Adams, M.; Dogic, Z.; Keller, S. L.; Fraden, S., Entropically driven microphase transitions in mixtures of colloidal rods and spheres. *Nature* 1998, 393, (6683), 349–352.
134. Marvin, D. A., X-ray diffraction and electron microscope studies on the structure of the small filamentous bacteriophage fd. *Journal of Molecular Biology* 1966, 15, (1), 8–IN4.
135. Bergenholtz, J.; Poon, W. C. K.; Fuchs, M., Gelation in Model Colloid–Polymer Mixtures. *Langmuir* 2003, 19, (10), 4493–4503.
136. Di Michele, L.; Eiser, E., Developments in understanding and controlling self assembly of DNA-functionalized colloids. *Phys Chem Chem Phys* 2013, 15, (9), 3115–29.
137. Obrovac, M.; Christensen, L., Structural changes in silicon anodes during lithium insertion/extraction. *Electrochemical and Solid-State Letters* 2004, 7, (5), A93–A96.
138. Michan, A. L.; Leskes, M.; Grey, C. P., Voltage Dependent Solid Electrolyte Interphase Formation in Silicon Electrodes: Monitoring the Formation of Organic Decomposition Products. *Chemistry of Materials* 2016, 28, (1), 385–398.
139. Kasavajjula, U.; Wang, C.; Appleby, A. J., Nano- and bulk-silicon-based insertion anodes for lithium-ion secondary cells. *Journal of Power Sources* 2007, 163, (2), 1003–1039.
140. Chan, C. K.; Peng, H.; Liu, G.; McIlwrath, K.; Zhang, X. F.; Huggins, R. A.; Cui, Y., High-performance lithium battery anodes using silicon nanowires. *Nat Nano* 2008, 3, (1), 31–35.
141. Michan, A. L.; Divitini, G.; Pell, A. J.; Leskes, M.; Ducati, C.; Grey, C. P., Solid electrolyte interphase growth and capacity loss in silicon electrodes. *Journal of the American Chemical Society* 2016, 138, (25), 7918–7931.
142. Liu, N.; Lu, Z.; Zhao, J.; McDowell, M. T.; Lee, H.-W.; Zhao, W.; Cui, Y., A pomegranate-inspired nanoscale design for large-volume-change lithium battery anodes. *Nature nanotechnology* 2014, 9, (3), 187–192.
143. Park, S.-J.; Zhao, H.; Ai, G.; Wang, C.; Song, X.; Yuca, N.; Battaglia, V. S.; Yang, W.; Liu, G., Side-chain conducting and phase-separated polymeric binders for high-performance

- silicon anodes in lithium-ion batteries. *Journal of the American Chemical Society* 2015, 137, (7), 2565-2571.
144. Kharissova, O. V.; Kharisov, B. I.; de Casas Ortiz, E. G., Dispersion of carbon nanotubes in water and non-aqueous solvents. *RSC Advances* 2013, 3, (47), 24812-24852.
145. Li, H.; Cheng, F.; Duft, A. M.; Adronov, A., Functionalization of Single-Walled Carbon Nanotubes with Well-Defined Polystyrene by "Click" Coupling. *Journal of the American Chemical Society* 2005, 127, (41), 14518-14524.
146. Dyke, C. A.; Tour, J. M., Solvent-free functionalization of carbon nanotubes. *Journal of the American Chemical Society* 2003, 125, (5), 1156-1157.
147. Dresselhaus, M. S.; Dresselhaus, G.; Saito, R.; Jorio, A., Raman spectroscopy of carbon nanotubes. *Physics reports* 2005, 409, (2), 47-99.
148. Huang, W.; Lin, Y.; Taylor, S.; Gaillard, J.; Rao, A. M.; Sun, Y.-P., Sonication-Assisted Functionalization and Solubilization of Carbon Nanotubes. *Nano Letters* 2002, 2, (3), 231-234.
149. Lipińska, M. E.; Rebelo, S. L.; Pereira, M. F. R.; Gomes, J.; Freire, C.; Figueiredo, J., New insights into the functionalization of multi-walled carbon nanotubes with aniline derivatives. *Carbon* 2012, 50, (9), 3280-3294.
150. Bahr, J. L.; Tour, J. M., Covalent chemistry of single-wall carbon nanotubes. *Journal of Materials Chemistry* 2002, 12, (7), 1952-1958.
151. Stewart, M. P.; Buriak, J. M., Exciton-Mediated Hydrosilylation on Photoluminescent Nanocrystalline Silicon. *Journal of the American Chemical Society* 2001, 123, (32), 7821-7830.
152. Buriak, J. M., Illuminating Silicon Surface Hydrosilylation: An Unexpected Plurality of Mechanisms. *Chemistry of Materials* 2014, 26, (1), 763-772.
153. Neiner, D.; Chiu, H. W.; Kauzlarich, S. M., Low-temperature solution route to macroscopic amounts of hydrogen terminated silicon nanoparticles. *Journal of the American Chemical Society* 2006, 128, (34), 11016-11017.
154. Kim, H.; Seo, M.; Park, M. H.; Cho, J., A critical size of silicon nano-anodes for lithium rechargeable batteries. *Angewandte Chemie International Edition* 2010, 49, (12), 2146-2149.